Researches
on
Decadal Polar Motion
and
GPS Retrieved Water Vapor

Tetsuya Iwabuchi

Acknowledgements

First of all, the author would like to express his hearty gratitude to his supervisor Professor Isao Naito, National Astronomical Observatory (NAO), Mizusawa, not only for many meaningful advice and encouragement to these researches in frontiers of geodesy, but also for thoughtfulness of the author's health during the course of this study. Owing to his suggestions, an initial interest of the author in monitoring sea level rise due to the global warming could be expand into various interests in basic roles of water in the Earth rotation dynamics and Global Positioning System (GPS).

Fortunately, the author could take an active part in "GPS/MET Japan", GPS meteorology project of Japan, launched in April, 1997. He would like to thank all the members of this project for their kind comments and advice.

The author expresses his appreciation to his colleagues in weekly seminar on Earth and planet researches at NAO, Mizusawa, convened by Prof. I. Naito, especially to Dr. Takashi Takanezawa and Dr. Yuichi Aoyama for many ingoing discussions to his researches, to Drs. Yoshiaki Tamura, Kosuke Heki, Tadahiro Sato, and Masatsugu Ooe for their useful comments and advice. In the lectures of the seminar, he was always stimulated and excited with discussions with his colleagues.

Mr. Katsushi Chida kindly helped a part of GPS data processing. Discussions with him are also useful to develop this study.

The author also thanks Dr. Kimio Hanawa for his comments on the decadal variability in climate system, Drs. Koichi Masuda, Taikan Oki, and Hiroshi Matsuyama for discussions on precipitation changes and water balance model, and Dr. Shin'ichi Miyazaki for discussions on GPS tropospheric delay gradient due to water vapor distributions.

The author wish to thank Dr. Richard Gross for providing SPACE94 data, JMA for providing the atmospheric sea level pressure data in the Northern Hemisphere of JMA, NOAA for providing precipitation data set. Thanks are also extended to members of Geographical Survey Institute (GSI) and University NAVSTAR Consortium (UNAVCO), for providing

data of GSI's GPS array, especially to Dr. Mikio Tobita of GSI for providing the coordinate transformation program, tky2wgs, and to many software scientist who provided Generic Mapping Tool (GMT) for assistance in his researches.

Finally, the author would like to thank all of my family who have always been supported him. His mother, passed away in April 1995, understood his will and encouraged him to continue his studies. The author could not accomplish this work without their continuous supports and encouragement.

Extended Abstract

In this thesis, we present basic discussions in the geodetic verification and monitoring of the effects of the global warming on the geosystem.

It is well known that the global warming is induced by rapid discharge of green house gases due to increase in human activities. In spite of the requirements to understand the global warming, present verifications and predictions on effects of the global warming have uncertainties. There are two major reasons; (1) rates of various decadal variations in climate system are equal to- or more than- those of climate changes due to the global warming, and (2) precision and space-time resolution in meteorological observation of water vapor, one of the most effective green house gases in constituents of atmosphere, are not enough at present. Then, concerning (1), we try to study mechanism of the decadal variations through understandings the decadal polar motion, and concerning (2), we try to detect behavior of water vapor from analysis of Global Positioning System (GPS) in this thesis.

At first (*chapter 2*), we find that decadal polar motion based on IPMS data and SPACE94 data shows similar variation with a decadal variation in index of the North Atlantic Oscillation (NAO), atmospheric teleconnection pattern having structure of north-south dipole in atmospheric pressure centered in the North Atlantic. The excitation pole based on atmospheric pressure data in the Northern Hemisphere from Japan Meteorological Agency (JMA), however, can only explain about one fifth of amplitude in the observed decadal excitation pole.

On the other hand, sea level changes based on Permanent Service for Mean Sea Level (PSMSL) data show decadal variations in global-scale. We find that the variation is dominant in coastal regions of the North Atlantic, where decadal east-west oscillation of the sea level corresponding to the decadal polar motion can be seen. The decadal sea level oscillation, in general, can not be considered to excite the polar motion under the plausible assumption that water in ocean follows isostatic equilibrium on time-scale longer than several years.

Contributions of land water storage to the decadal polar motion are also studied based on monthly gridded precipitation anomalies data for $5^o \times 5^o$ compiled by National Oceanic

and Atmospheric Administration (NOAA), where the model used for the computation and the discussion assumes that land water storage is expressed by precipitation and its exponential decay time. When the decay time is 3.7 months, namely when 1/e of precipitation in arbitrary month flows out into the ocean after 3.7 months, square of the difference between the observed and the calculated excitation poles is minimum, and ten-yearly periodic components of observed and calculated excitation poles show similar ellipsoids though the calculated excitation pole can explain only 37 % of the observed one. However, the calculated excitation pole can explain more than 80% of the observed one at the decay time is 6 to 7 months, if the small phase difference of about 1 year between them is neglected.

We also find decadal seesaw-like variations in precipitation between North America and Eurasia, in which these precipitation patterns behave to excite the decadal polar motion efficiently. Thus, we advocate a conceptual model on decadal hydrologic cycle centered in the North Atlantic to link the observational facts, where decadal variations of land water storage can explain the excitation of the decadal polar motion.

At second (*chapter 3*), we show potential ability of dense nationwide GPS array in Geographical Survey Institute (GSI) in Japan, which consists of 612 GPS sites and has space resolution of about 50km, as water vapor sensor over the Japanese Islands.

In GPS analysis, zenith tropospheric delay (ZTD) is estimated simultaneously with site coordinate, where ZTD is sum of the zenith hydrostatic delay (ZHD) which depend upon atmospheric pressure and zenith wet delay (ZWD) due to water vapor in zenith direction. ZWD can be converted to precipitable water vapor (PWV), integrated water vapor in atmospheric column above the ground by multiplying ZWD by a proportional coefficient equal to about 0.15.

During a front passage in summer, we illustrate behavior of GPS retrieved water vapor around the front accompanying with heavy rains, where errors due to GPS analysis is estimated as about 1 mm. These show potential ability of the GSI's GPS array as water vapor sensor over the Japanese Islands in all weather conditions. However, comparison between GPS retrieved PWV and those based on numerical weather prediction (NWP) in JMA shows underestimation of GPS PWV of about 3 mm.

When ZTD shows azimuthally inhomogeneous distribution during weather conditions of passages of front and tropical cyclone, apparent variations of horizontal coordinate of several cm are generally seen. We illustrate a close relationship between the horizontal coordinate variation and ZTD gradient based on the operational analysis of the nationwide GPS array of GSI. With the relationship, unusually large horizontal coordinate variations can be diagnosed if they reflect net crustal movement connected with occurrence of earthquakes or noise due

to azimuthally inhomogeneous distribution of water vapor.

On the other hand, we show that the GSI's GPS array acquires diurnal variation of water vapor due to thermally induced local circulation over the Japanese Islands in summer. Composite analysis and principal component analysis of ZTD in July and August, 1996, show spatio-temporal pattern of the diurnal variation, rapid increase in the daytime and gentle decrease in nighttime, over the Japanese Islands especially in mountainous area. The similar diurnal variation is also confirmed in precipitation. All the above results suggest that GPS retrieved ZTD can contribute to mesoscale meteorology.

The potential ability of the GSI's GPS array as excellent water vapor sensor in all weather conditions suggests that the globally distributed ground-based GPS network can monitor a trend in water vapor due to the global warming. An accumulation of the GPS water vapor information would hopefully make it possible to provide us transportation patterns of water vapor connected with the decadal hydrological cycle stated above in future.

The results presented in this thesis indicate that the geodetic verification and monitoring of the effects of the global warming are available with precise space geodetic technique.

Contents

List of Tables

List of Figures

Chapter 1

Introduction

1.1 Global Warming and Decadal Variability

1.1.1 Global Warming and Climate Changes

Discharges of the green house gases (ex. carbon dioxide (CO_2), methane (CH_4), chlorofluorocarbons ($CFCs$)) due to rapid increase of human activities by consuming fossil fuel and deforesting in the tropic are considered to induce the global warming. Global mean surface temperature actually has increased by 0.3 to $0.6°C$ over the last 100 years according to historical temperature observations, while increase of 1.5 to 4.5 $°C$ is predicted based on climate model simulation, general circulation model (GCM) of atmosphere and ocean, with CO_2 doubling [*IPCC: Intergovernmental Panel for Climate Change*, 1990]. Considering global increase of population, climate changes induced by the global warming can cause serious problems in shortage of foods due to extreme regional decrease of agricultural production. In the predictable effects by the global warming, sea level rise mainly contributed by steric expansion of sea water and melting of land ice arises serious disasters in regions distributed around 0 meter above sea level such as many metropolitan area which faces the ocean and in insular country. Thus, we need to understand the mechanism of global warming and to make the accurate prediction of the effects of the global warming for the development of human activity and realization of the coexistence with nature.

However, predictions of global mean surface temperature under CO_2 doubling based on climate model have uncertainties of about 3 $°C$ as mentioned above. The main reason is lack of information on climate system, especially in complicated interactions among atmosphere, ocean, and land on various timescales. Above all, origins of the decadal variations observed in most of metorological phenomena are open question as will be mentioned below while mechanisms on inter-annual variations has rapidly been clarified with recent studies. The problem is that rates of changes in decadal variations are same order as those in climate chsnges due to the global warming. Thus, the decadal variations are considered as obstacles to verify the global warming and its effects from several to decadal years data.

1.1.2 Decadal Polar Motion

Introducing space technique in geodesy have made it possible to measure coordinates and sea level with accuracy of better than several centimeter. For example, global sea level rise of about 4 mm/yr was detected with TOPEX/ POSEIDON (T/P) satellite altimetry of two-yeras [*Nerem*, 1995]. However, to extract net sea level rise due only to the global warming from the sea level data is difficult because of existence of the decadal variability. *Nerem et al.* [1997], for example, have mentioned that effects of inter-annual to decadal variations may be contained in the rate of sea level rise. Further, *Haines and Bar-Sever* [1998] have found that the rate of sea level rise can be changed by about 1.2 mm due to drift in water vapor radiometer (WVR) of T/P, in which the calibration was made by GPS measurement; this is the most important motivation for this thesis (GPS retrieved water vapor is discussed in section 3.1.). Consequently, understandings of the decadal variations are extremely important to detect the effects of the global warming when short data are used.

On the other hand, decadal variation can be also seen in polar motion, the variation of the Earth's rotational axis in the geographical coordinate system. Polar motion up to decadal time-scale is known to be mainly excited by redistribution of mass and relative angular momentum change in atmosphere and hydrosphere. The origins of the decadal variations in climate system are expected to be clarified by understandings on the excitation dynamics of the decadal polar motion. Thus, in this thesis, with the polar motion data, we first try to understand the decadal variations in climate system from the geodetic viewpoint.

1.2 Global Warming and Water Vapor

1.2.1 The Role of Water Vapor for Global Warming

Water vapor is known as one of the most effective greenhouse effect gas in constituents of atmosphere. Moreover, it induces positive feedback for the global warming, that is, the global warming increases amount of water vapor in atmosphere due to increases of its saturation temperature, and the increased water vapor accelerates the global warming. With the variations, precipitation patterns are also considered to drastically vary especially in mid and high latitudes where large increase of surface temperature are predicted in the climate model with CO_2 doubling. For example, the northern Japan regions can be expected to be damaged by torrential rains in every rainy season.

Although water vapor play an important role in the global warming, its behaviors have not well understood mainly due to shortage of the space-time resolution of water vapor observation. For example, routine observations with radiosonde that can retrieve vertical distribution precisely have limitation of space resolution of several hundred km and of time resolution of every twelve hours. On the other hand, observation with water vapor radiometer mounted in artificial satellites have a weak point over land. Due to these limitations, the prediction of the local torrential rains in Japan is considered to be very difficult. Thus, we need developments of new water vapor sensor which has high space-time resolution to monitor local behaviors of water vapor as will be mentioned below.

1.2.2 GPS Retrieved Water Vapor

Water vapor in troposphere is also one of major error sources in coordinate estimation of Global Positioning System (GPS), a satellite-based positioning system widely used for navigation, relative positioning, and time transfers (see Appendix B.1). The accuracy of relative positioning used for monitoring crustal movements reaches mm to cm. In general, daily coordinate solutions in GPS analysis show apparent variations of about several cm especially in summer wet season due to tropospheric delay by water vapor (wet delay). Precision of GPS estimated coordinate can be improved if behaviors of water vapor are modeled appropriately. This enable us to detect not only minute signal related to occurrence of earthquakes, but also sea level rise due to the global warming by subtracting effects of vertical crustal movement from tide gage data. The sea level data enables powerful calibration for T/P altimeter.

The wet delay estimated simultaneously with coordinates contain information water vapor contents. In general, GPS-derived precipitable water vapor (PWV), integrated water vapor in atmospheric column above the ground, which is proportional to zenith wet delay, has accuracy as same as or better than PWV observed by usual meteorological instruments such as radiosonde and water vapor radiometer, so that GPS also have important role to calibrate the drift as mentioned above [*Haines and Bar-Sever*, 1998]. Therefore, if a dense GPS array is deployed, GPS retrieved PWV is expected not only to detect new facts on behaviors of water vapor but also to monitor increase of water vapor due to the global warming.

Fortunately, there is a nationwide dense GPS array installed by Geographical Survey Institute (GSI) for the purpose of monitoring crustal deformation and for constructing highly precise geodetic network in Japan. The number of GPS sites in the array has rapidly increased under requirements of earthquake prediction and investigation into the mechanism of earthquakes especially since the occurrence of the Great Hanshin-Awaji Earthquake in January 1995. The array which consists of 612 sites in 1996 (about 1000 sites in 1998) is the most dense network routinely operated in the world; its space interval is about 50 km (20 km in 1998). With the GPS array, we can greatly expect high space resolution data of water vapor over the Japanese Islands. Thus, in this thesis, we second try to clarify behaviors of water vapor over the Japanese Islands with the GPS array.

1.3 Purposes of the Thesis

The two theme stated above aim at geodetic understanding and monitoring of the effects of the global warming from the geodetic viewpoint by means of space technique in geodesy. Both fruits have complementary relationship to understand the climate system, especially on effects of the global warming.

Thus, we have studied (1) excitation sources of the ten-yearly polar motion and (2) GPS retrieved water vapor. The purpose of (1) is to understand mechanism of the decadal variations in climate system based on polar motion with atmospheric and hydrospheric data, and (2) aims at understandings on behaviors of water vapor based on the GSI's nationwide GPS array to improve precision of GPS coordinate estimation.

1.4 Structure of the Thesis

This thesis is divided into two parts; (1) understandings meteorological excitation sources of the decadal polar motion, and (2) understandings on behaviors of GPS retrieved water vapor.

In Chapter 2, excitation sources of ten-yearly polar motion are stated. Contributions of decadal variations in atmosphere and ocean to the polar motion are presented at the first section. The second section deals with excitation of the decadal polar motion based on variations of the land water storage in North America and Eurasia, where we advocate the ten-yearly hydrologic cycle centered in the North Atlantic Ocean.

Subsequently, chapter 3 deals with GPS retrieved water vapor. The first section presents behaviors of GPS retrieved water vapors over the Japanese Islands based on GSI's nation-wide GPS array, where we show potential of the array as water vapor sensor at all weather condition. At the second section, effects of azimuthally inhomogeneous distribution of water vapor to horizontal coordinate solution is investigated in weather conditions of passage of front and tropical cyclone. The last section deals with summer diurnal variations of GPS retrieved water vapor over the Japanese Islands, where we show the behaviors due to thermally induced local circulation over the Japan Islands.

Bibliography

[*Haines and Bar-Sever*, 1998] Haines, B. J. and Y. E. Bar-Sever, Monitoring the TOPEX Microwave Radiowave with GPS: Stability of Columnar Water Vapor Measurements, Geophys. Res. Lett., 25, 3536-3566.

[*IPCC*, 1990] IPCC, Climate Change, The IPCC Scientific Assessment, eds. J. H. Houghton, G. J. Jenkins and J. J. Ephraums, Cambridge Univ. Press, 365p., 1990.

[*IPCC*, 1996] IPCC, Climate Change, 1995, The Science of Climate Change, eds. J. H. Houghton, L. G. M. Filho, B. A. Callander, N. Harris, A. Kattenberg and K. Maskell, Cambridge Univ. Press, 572p., 1996.

[*Nerem*, 1995] Nerem, R. S., Global Mean Sea Level Variations from TOPEX/ POSEIDON Altimeter Data, Science, 268, 708-710, 1995.

[*Nerem et al.*, 1997] Nerem, R. S., B. J. Haines, J. Hendricks, J. F. Minster, G. T. Mitchum, and W. B. White, Improved Determination of Global Mean Sea Level Variations using TOPEX/ POSEIDON Altimeter Data, Geophys. Res. Lett., 24, 1331-1334.

Chapter 2

Excitation Sources of Ten-yearly Polar Motion

2.1 Decadal Polar Motion Connected with Atmospheric Pressure and Sea Level Patterns over the North Atlantic Ocean

2.1.1 Abstract

This section intends to discuss sources of the decadal polar motion, focusing on a decadal fluctuation of the NAO (North Atlantic Oscillation) known as atmospheric pressure oscillation between middle and high latitudes over the North Atlantic Ocean.

Some correlation and similar patterns are found between decadal variations of the polar motion and the NAO index. A model computation shows that the decadal polar motion could be explained by a zonally asymmetric atmospheric pressure distribution of about 1 hPa over the northern hemisphere which may be connected with the NAO. Results of calculation with sea level atmospheric pressure data, however, reveal that the atmosphere cannot be the source of the decadal polar motion.

Sea level changes corresponding to the decadal polar motion are also found in the North Atlantic Ocean, in particular along the east coasts of the North America. A model computation suggests that the decadal polar motion is also explained by sea level changes of a few centimeters in the northern hemisphere. However, if these sea level changes are due to atmospheric pressure variations, they cannot be the source of the decadal polar motion under assumption of inverted barometer rule.

These results suggest that the sources of the decadal polar motion are to be found among land water and glaciers. A water mass redistribution over the northern hemisphere connected with land water variation is the most plausible source for the decadal polar motion.

2.1.2 Introduction

The variation of the Earth's rotational axis in the geographical coordinate system is known as the polar motion. It is mainly excited by redistribution of mass and relative angular momentum change of the atmosphere and hydrosphere [e.g. *Munk and MacDonald*, 1960; *Lambeck*, 1980; *Barnes et al.*, 1983].

Introduction of space geodesy in the 1970s has markedly improved the accuracy and resolution in the Earth's rotation data. At the same time, new information on intra-and inter-annual polar motions has been accumulated and analyzed in addition to those on the Chandler wobble and the annual wobble [e.g. *Chao and Au*, 1991; *Eubanks*, 1993].

Zhou and Chao [1995], for example, reported the strong correlation between the NAO index and polar motion at the inter-annual timescale. *Kikuchi and Naito* [1995] also found the decadal polar motion in the IPMS (International Polar Motion Service) data and the SPACE94 data (Figure 2.1). However, its excitation dynamic remains to be an open question.

Variations on decadal timescale are hot topics in the study of the atmosphere-ocean system. One of such variations is the NAO (North Atlantic Oscillation) atmospheric teleconnection pattern having north-south dipole in the North Atlantic [*Walker and Bliss*, 1932; *Deser and Blackmon*, 1993]. *Hurell* [1995] revealed that decadal variability in the NAO has been remarkable since 1950 using its winter (December through March) index derived from the difference of normalized pressures between Lisbon in Portugal and Stykkisholmur in Iceland.

Decadal scale variations are also seen in the ocean. *Groger and Plag* [1993] showed east-west motion of the oceanic heights on decadal to interdecadal timescales with Permanent Service for Mean Sea Level (PSMSL) data set. Lately, *Unal and Ghil* [1995] also reported that decadal sea level variation can be seen globally.

In this paper, we first point out similarity between the decadal polar motion and the NAO index variations, secondly we consider whether or not the NAO teleconnection and the atmospheric pressure variations are physically responsible for the decadal polar motion, thirdly we show the relationship between the decadal polar motion and the global sea level changes, and lastly we discuss their inter-relationship.

2.1.3 Polar Motion and Excitation Function

According to the conventional notation, coordinates of rotation pole along the Greenwich Meridian and along $90^\circ E$ longitude axes can be defined as m_1 and m_2, respectively, and complex form $\tilde{\chi} = \chi_1 + \chi_2$ is generally used. If the excitation function of $\tilde{m}$ is defined as $\tilde{\chi}$, the equation of the polar motion is given by

$$\frac{i}{\sigma_0}\frac{d\tilde{m}}{dt} + \tilde{m} = \tilde{\chi} \tag{1}$$

where $\sigma_0 = 2\pi\{F_c(1 + 1/2Q)\}$ is complex-valued frequency of Chandler wobble, that is one of the Earth's free oscillation, F_c is frequency (0.843cpy) of Chandler wobble, and $1/Q_c$ is the factor which indicates the dissipation of energy near F_c [e.g. *Munk and MacDonald*, 1960; *Wilson*, 1985]. In Eq (1), $\tilde{\chi}$ calculated from $\tilde{m}$ based on geodetic observation is called as geodetically observed excitation pole.

The first term in the left hand of Eq (1) is negligible because the frequencies around 0.1 cpy to be considered here are much lower than F_c, so that $\tilde{m}$ can be regard as $\tilde{\chi}$ approximately in discussion in this study. Hereafter, is called as excitation pole, which is approximately equal to rotation pole in case of decadal time-scale.

In general, $\tilde{\chi}$ based on geophysical observation is called as geophysically observed excitation pole. The excitation pole contributed by the mass redistribution in atmosphere and hydrosphere is given by

$$\tilde{\chi} = 1.00\frac{-1}{C-A}\int \rho D r^2 \cos\phi \sin\phi \exp(i\lambda) dS \tag{2}$$

where the factor 1.00 in the right hand results from the cancellation of the effects between the rotational deformation of the Earth and the solid Earth elasticity by surface loading, D is depth or height of fluids' mass distributions with density ρ, C and A are the Earth's polar and equatorial moments of inertia, r is the mean radius of the Earth, ϕ and λ are latitude and longitude, respectively and $dS = r^2 \cos\phi d\phi d\lambda$ [e.g. *Barnes et al.* 1993; *Eubanks*, 1992]. For further details, see Appendix A.

2.1.4 Data and Computation

We use the two polar motion data sets; one is the IPMS data for 1962-1975 and the other the SPACE94 data for 1976 - 1995. The sampling interval of both data set are 5 days. Older polar motion data based on ILS (International Latitude Service) are not used here because of their low precision [e.g. *Eubanks*, 1993].

To study the relation between the polar motion and the NAO index, we use time series data of the NAO index for 1962-1995 [*Hurell*, 1995] during which a typical NAO pressure pattern is found (Figure 2.2). In addition, the monthly mean atmospheric sea level pressure data in the northern hemisphere for the period 1951-1990 provided from the Japan Meteorological Agency (JMA) are used to calculate excitation of the decadal polar motion; for excitation dynamics of polar motion, see chapter 3 of *Eubanks* [1993].

Monthly mean sea level data of PSMSL [*Woodworth*, 1991] for 1951-1990 are used to search decadal sea level variations, but the data including steps or gaps are not used here.

2.1.5 Results of Analysis

Excitation function given by a deconvolution of the polar motion is expressed conventionally with χ_1 (along the Greenwich meridian) and χ_2 ($90^\circ E$) components [*Barnes et al.* 1983; *Eubanks*, 1993]. Figure 2.3 shows the decadal variation of the excitation pole in Figure 2.1 smoothed with 5-year low-pass filter and detrended by a least-square fitting. Here we call this the decadal polar motion. Note that it rotates counterclockwise.

Figure 2.4 shows the polar motion and variation of the NAO index. Noteworthy is that χ_1 and the NAO index have similar behavior; the NAO index also has correlation with χ_2 of 2.5 years lag.

A model computation shows that the decadal polar motion is induced by a global atmospheric pressure distribution of 1 hPa of spherical harmonic function of degree 2 and order 1. Therefore, we try to calculate the excitation function for the decadal polar motion by the observed atmospheric sea level pressure data over the northern hemisphere. The calculations are done assuming IB(Inverted Barometer) response of the ocean is assumed [e.g. *Munk and MacDonald*, 1960; *Ponte et al.*, 1991]. Figure 2.5 shows the calculated decadal polar motion. Its magnitude of variation is about one fourth of the observed decadal polar motion in Figure 2.3, and its rotational direction is opposite to observed one. These suggest that the atmospheric pressure variations are not the source of the decadal polar motion. On the other hand, the sea level changes are investigated with a spectrum analysis to detect decadal variation. The results show similar behaviors to those obtained by *Unal and Ghil* [1995]; decadal sea level changes are seen globally. It is found, in particular, that amplitudes of the decadal sea level changes are larger in the North Pacific Ocean and the North Atlantic Ocean than in other oceans. The sea level changes in the North Atlantic Ocean corresponding the decadal polar motion in Figure 2.3 are shown in Figure 2.6. The seesaw-like patterns of the sea level variation are mainly seen along the east coast of the North America. The similar patterns have been pointed out by *Georger and Plag* [1992].

We calculate the decadal polar motion by the seesaw-like sea level changes assuming that there exists mass distribution corresponding to these sea level changes in the North Atlantic Ocean. The results show that the decadal polar motion can be explained by the hypothesized sea level change of about 5 cm.

2.1.6 Discussion and Concluding Remarks

Similar patterns and correlation are found between the decadal polar motion and the NAO index. However, the observed data shows that the atmospheric pressure contribution to the decadal polar motion is negligible.

On the other hand, decadal sea level changes are found to exist globally. In particular, seesaw-like sea level changes corresponding to the decadal polar motion are found in the North Atlantic Ocean. The decadal polar motion can be excited by these sea level changes if they reflect real mass distribution. The possibility depends upon whether or not these sea level changes are net changes in oceanic mass. This is a problem to be explained in physical oceanography.

Now, the polar motion is generally ascribed to mass redistribution of the atmosphere, land water and ocean, and to relative angular momentum changes of atmosphere, ocean, and Earth's fluid core. For example, a number of authors have investigated on the annual wobble and concluded that it is mainly excited by atmospheric pressure redistribution and partly by redistribution of land water [e.g. *Chao and Au*, 1991; *Wahr*, 1983]. In addition, secular polar motion can be explained by post-glacial rebound, sea level changes, melting of glacial ice and land water storage on order of 10 to 20% [e.g. *Eubanks*, 1993; *Trupin*, 1993].

We have not considered effect of land water to the decadal polar motion yet though it would partly contribute the polar motions on various time-scale. Comprehensive data of land water changes to discuss the decadal polar motion, however, does not exist now, so such analysis remains to be solved future.

According to *Bradley et al.* [1987], decadal variations of the precipitation exist over the continents in the northern hemisphere. In particular, these variations have been strong since about 1950 in the United States, North Africa and Middle East. These facts suggest that the decadal polar motion may be excited mainly or partly by redistribution of land water.

If the land water distribution is the major source of the decadal polar motion, its magnitude is 1 g/cm^2 on the surface of the Earth like the atmospheric pressure distribution and the sea level change. The correlation among the decadal polar motion, NAO index, and sea level changes found in this study may suggest an existence of the decadal hydrological cycle.

2.2 Ten-yearly Polar Motion Connected with Precipitation Changes over North American and Eurasian Continents

2.2.1 Abstract

A hydrologic excitation model of ten-yearly polar motion appearing in the combined polar motion data of five-daily IPMS and SPACE94 during 1962-1995 is proposed. The model is based on the exponential decay of the land water storage supplied by precipitation. The NOAA monthly gridded precipitation anomaly data for $5^o \times 5^o$ are used for the model estimation. By assuming that the land water decreases exponentially with time, about 37 % of the ten-yearly polar motion can be explained when decay parameter τ_d of 3.7 month. The seesaw-like changes of precipitation that efficiently excite the ten-yearly polar motion are also confirmed between the North American continent and western region of the Eurasian continent. From these results, a new look at the ten-yearly hydrological cycle system is advocated, which consists of atmospheric variations connected with the North Atlantic Oscillation, see-saw like sea level changes along both coastal regions in the North Atlantic Ocean, and precipitation changes in the North American continent and the Eurasian continent. The essential factor to determine ten-year scale in the system is considered to be hydrological cycle in the two continent.

2.2.2 Introduction

The understanding and identification of decadal variability in the climate system are important for the detection and prediction of the global warming due to increase of human activities. The reason is that the rate of the decadal change is as same as or more than that of global warming. The global warming based on short data for several years to several ten years should thus be discussed taking the natural decadal change into account.

The mechanism of the decadal variability, however, has not been well known yet in contrast with the rapid development of understandings on dominant inter-annual variability like as El Niño / Southern Oscillation [ENSO, e.g. *Philander*, 1990] phenomena. One reason is that the decadal variability are produced by complicated interaction among the elements that compose the climate system [e.g. *Latif*, 1998], and another reason is a shortage of data to construct models on the decadal variability.

A decadal variation has also found in polar motion [*Kikuchi and Naito*, 1995], that is the variation of the Earth's instantaneous rotational axis in the geographyical coordinate system. In general, polar motion up to decadal time-scale is known to be excited by redistribution of mass and relative angular momentum change in atmosphere and hydrosphere [e.g. *Munk and MacDonald*, 1960; *Lambeck*, 1980]. Thus, dynamics of the decadal variability in atmosphere and hydrosphere can be understood by an approach to investigate the excitation of the polar motion as a global indicator on motion of the fluids distributed in the Earth's surface.

Since the polar motion is excited by integration of the phenomena all over the Earth, it sensitively reflects global variations in atmosphere and hydrosphere. In such phenomena, teleconnection patterns in the atmosphere, that is systematic distribution pattern of the atmospheric pressure in hemisphere-scale [e.g. *Walker and Bliss*, 1932; *Wallace and Gutzler*, 1981; *Wallace*, 1996 as references], are recognized as one of the major phenomena. For example, *Chao and Zhou* [1997] have shown that inter-annual polar motion changes in connection with North Atlantic Oscillation (NAO) atmospheric teleconnection pattern, where NAO is a dominant teleconnection pattern in the mid and high latitude in the Northern Hemisphere, which is represented by seesaw-like variations of atmospheric pressure between Icelandic Low and Azores High [e.g. *Walker and Bliss*, 1932; *Hurrell*, 1995].

On the other hand, Southern Oscillation (SO), which has been defined by *Walker and Bliss* [1932], is the most well known teleconnection pattern in the tropical Pacific. *Chao and Zhou* [1997] and *Naito et al.* [1998], however, have shown that relationships between the SO and the polar motion are weaker than those of the NAO's.

In a dynamics of the polar motion excitation, contributions of meteorological variations to the polar motion become maximum in both 45° latitudes. Moreover, redistribution of atmospheric pressure and water mass act as net mass loading only in land area, while these effects are averaged globally on the sea floor due to static or isostatic ocean response on decadal time-scale by plausible assumptions. They imply one reason why the NAO shows more correlation with the polar motion than the SO.

In the NAO, a decadal variation has also been found by *Hurrell* [1995]. He has shown that the decadal variation can be seen in the winter (December to March) NAO index defined as the difference of normalized pressure between Lisbon in Portugal and Stykkisholmur in Iceland. He has also mentioned that the variation has been remarkable since 1950. The time evolution of the NAO index has also confirmed by *Hurrell and van Loon* [1997] in spectrum analyses with time windows. They have shown that the spectrum power on the period of 6-10 years becomes stronger toward the end of the period during 1865 and 1994.

Lately, *Iwabuchi et al.* [1997] have found that the ten-yearly polar motion and the decadal variation of the NAO index [*Hurrell*, 1995] show similar behaviors. However, a calculated polar motion based on the atmospheric pressure data in the Northern Hemisphere is less than one fifth of the observed polar motion. Thus, they have mentioned that variations of the land water storage related to the NAO teleconnection pattern may be a excitation source of the ten-yearly polar motion.

Many decadal climate changes that are prominent around the North Atlantic Ocean, North American continent continents, and Eurasian continent also have shown in the previous studies based on observational evidences; sea level change [*Groger and Plag*, 1993; *Unal and Ghil*, 1995; *Iwabuchi et al.* 1997], sea surface temperature (SST) variation [*Deser and Blackmon*, 1993], surface temperature changes of about 10 to 11 years [*Mann and Park*, 1994, 1995], precipitation changes [*Bradley et al.* 1987; *Diaz et al.* 1989], and snow cover variation [*Walland and Simmonds*, 1997]. In these variations, the most probable excitation source for the ten-yearly polar motion is land water storage under the plausible assumption that water in the ocean follows isostatic equilibrium on decadal time-scale as mentioned above. According to *Bradley et al* [1987] and *Diaz et al.* [1989], changes of precipitation on inter-annual to inter-decadal time-scale can be seen in most of continents. Hence, hydrological excitation of the polar motion by distribution of water mass is expected to explain the ten-yearly polar motion.

Main two purposes of this study are first to investigate hydrological excitation of the ten-yearly polar motion based on precipitation data and a decay model of the land water storage supplied by precipitation, and second to clarify the mechanism of decadal variation whose center of action is the North Atlantic from the viewpoint of the earth rotation. Thus, in the paper, formulation, land water storage model and used data are described in section 2.2.3 and calculated excitation poles based on the model are described in section 2.2.4. In section 2.2.5, firstly, ten-yearly sinusoids of the excitation poles and correlation between precipitation change and the polar motion are discussed and secondly, a decadal hydrologic cycle model connected with the NAO is advocated to link the several decadal variations in atmosphere and ocean based on the results in this study. In section 2.2.6, the results of analysis are concluded.

2.2.3 Model and Data

Land Water Storage Model on Precipitation

In general, the terrestrial water balance equation is written as

$$\frac{dW}{dt} = P - E - R_r - R_g \tag{3}$$

where P, E, R_r ,R_g are precipitation, evaporation, river run-off, groundwater run-off, respectively. In the parameters in the right hand, E, R_r, and R_g can be hardly estimated accurately because reliable data of these parameters, particularly E and R_g, are not available.

Thus, this study assumes that E, R_r, and R_g are expressed by only one parameter so that the temporal integral in Eq (3) is given by

$$W(t) = \sum_{\tau=0}^{m}\{P(t-\tau)\cdot\kappa(\tau)\} \tag{4}$$

where the unit t and τ is month, amount of land water storage $W(t)$ is gone back from $\tau = 0$ to $\tau = m$, and κ is rate of run-off including the effects of E, R_r , and R_g. To simply express the decay pattern of the land water storage supplied by precipitation, two types of κ are evaluated; linear decay and exponential decay of precipitation in each grid. Since the both results do not show much differences, this study applies

$$\kappa(\tau) = \exp(-\tau/\tau_d) \tag{5}$$

where τ_d shows the decay constant which suggests decay time of the land water storage supplied by precipitation. Note that water gone out of each grid runs off into the ocean directly, namely, the water supplied by precipitation at arbitrary month decrease its $1/e$ just after τ_d months to release most part of the precipitation into the ocean based on Eq (4) and Eq (5).

When raw precipitation data which has rapid decrease of data number is used in Eq (4) and Eq (5), enormous biases arise in the model computation because water that should be as 'climate value' does not consider after the data missing. On the other hand, when anomaly data from mean value of the raw precipitation data is used, the biases are far smaller than those based on the raw data because the most biases are already removed as the mean value. However, the anomaly data can not be used if nonlinear effects such as a switching based on surface air temperature to control run-off of precipitation are considered to modify Eq (4) and Eq (5). In the case, the raw data has to be used.

This model assumes that density of water is constant globally as $1.0gcm^{-3}$ because surface air temperature which mainly depends on height in the observation sites can not be evaluated accurately. In addition, the model ignores the excitation of the polar motion by redistribution of water vapor in the atmosphere because the effect is negligible to compare with the excitation by land water storage [e.g. *Hinnov and Wilson*, 1987; *Chao et al.*, 1987]. Water mass conservation between land and ocean is considered in the model under the assumption that the mass of the water vapor in the atmosphere and the land water storage in unused grids due to no observation or data missing are constant on time, namely, the total anomaly of water mass in land area is subtracted from the ocean area uniformly. The magnitude of excitation pole by water mass changes in the ocean is negligible due to large cancellation of the excitation by global distribution of the ocean.

At $m = 0$, Eq (4) and Eq (5) are simplified to ; a model that precipitation of each month in each grid runs off into the oceans at the end of the month. This means that excitation pole is calculated based on raw precipitation data without considering the decay process expressed in Eq (4) and Eq (5). Thus, hereafter, the model is called as a non-reservoir model though the existence of slight accumulating effect of precipitation within one month.

If $m > 0$, precipitation anomaly is accumulated in each grid to obey Eq (4) and Eq (5). Thus, hereafter, the model is called as a reservoir model. In the model computation, 120 months are adopted as the integration period m in Eq (4). Errors originated in the round off effect of $m = 120$ are confirmed to be negligible till $= 10.0$. The most suitable τ_d to account for the ten-yearly polar motion is fixed to evaluate a minimum value of square of the observed excitation pole minus the calculated excitation pole to vary τ_d every 0.1.

In the reservoir model, no additional parameters, dependencies of τ_d on geographical conditions such as latitude and topography for example, are not considered due to shortage of data to evaluate those parameters. However, dependencies of τ_ds on the length from the ocean in the observation sites are considered. They are evaluated by removing land area whose length from the ocean is less than about 500 km and 1000 km in the model computation.

Used Data

a) Polar Motion Data

This study uses the excitation function calculated by *Kikuchi and Naito* [1995] using a differential equation by *Wilson* [1985] shown in Eq (1) (see Appendix A). The excitation function is based on two kinds of polar motion data; one is the IPMS data for 1962-1975 and the other the SPACE94 data for 1976-1995 [*Gross*, 1996]. Sampling interval of the both data is five days. Note that two data are based on the different technique; the former is based on optical observations and the latter, space geodetic techniques. Although the former is less precise than the latter [e.g. *McCarthy and Luzum*, 1996], the two data are regarded as identical and continuous in this study because they agree with just slight discrepancies as mentioned by *Kikuchi and Naito* [1995]. Other older polar motion data are not used here because of their low precision to discuss the ten-yearly polar motion of cm order [e.g.

McCarthy and Luzum, 1996; *Eubanks*, 1993].

The observed excitation pole (hereafter, referred to as OP) after removing its trend is shown in Figure 2.7. The OP oscillates toward 59^oE and 126^oW, and its magnitude is comparable to the excitation pole calculated by imaginary patterns of mass redistribution assumed by a spatial pattern of $Y_{2,1}$ mode of spherical harmonics whose center of action is the North American continent and the Eurasian continent and whose amplitude is 10 mm. A excitation pole based on atmospheric pressure data also presented as a small curve in the upper-right of Figure 2.7. The magnitude of the oscillation is approximately one fifth of the and the direction of the rotation is opposite of that of the OP [*Iwabuchi et al.*, 1997].

b) Precipitation Data

The monthly gridded ($5^o \times 5^o$) precipitation anomalies data compiled by NOAA for 1950-1993 is used for P in Eq (3). The data is computed from the median for a period of 1951-1980 in each grid under the assumption of a spatial homogeneity of precipitation. Figure 2.8 shows the distribution of the data with a land map of $5^o \times 5^o$ used in this study, where land area is divided into five regions; North America, South America, Eurasia, Africa, and Australia (hereafter, the five regions of the land area are referred as those). A 90^oE line is defined in this study as a boundary between the western region and eastern region of Eurasia (hereafter, western Eurasia and eastern Eurasia).

The grids shown as blank grid indicate unused regions in the model computation where continuous data from 1960 to 1985 are not available. The effective grid number of the precipitation data is approximately 450 with small variations during 1950-1988. In 1989 and 1991, however, the number decrease largely to 220 at last. As stated in section 2.2.3, the error induced by the decrease of the data number is negligible when the anomaly data is used.

Comparisons of the calculated excitation pole with the observed excitation pole are started from 1962, so that 11 years of the calculated excitation pole can be considered as the period for spin-up to avoid systematic biases.

2.2.4 Calculated Excitation Functions from Precipitation Data

Non-Reservoir Model

As stated in section 2.2.3, the non-reservoir model to substitute 0 for m in Eq (4) and Eq (5) does not consider accumulations of precipitation anomaly. The calculated excitation pole at CP_0 (hereafter, CP_0) is shown as 'GLOBAL' in the top panel of Figure 2.9(b) with OP shown in Figure 2.7, where CP_0 is global contribution which consists of the excitation pole calculated in each continents shown in the lower panel of Figure 2.9(b) and the oceanic contribution to conserve water mass. Note that all the excitation poles in this study are 60-month low-pass filtered and detrended values. CP_0 and OP show similar variations each other. The correlation coefficients are 0.50 and 0.46 in χ_1 and χ_2, respectively, and 0.54 in the direction of the oscillation shown in Figure 2.7. Considering phase lags, the correlation coefficients increase to 0.52 in χ_1 when the CP_0 leads the OP by 10 months, and 0.75 in χ_2 by 14 months. However, the magnitude of the CP_0 is fairly small comparing to that of OP The fact suggests that the accumulations of the precipitation anomalies are essential to explain the OP based on the land water storage model.

To see each continental excitation in the lower panel of Figure 2.9(b), the variations both in North American and in western Eurasia are similar to the OP's variations, especially in χ_2 . On the other hand, the variations in other continents also sometimes show considerable large variations. For example, the magnitude of the excitation pole in Australia is remarkably large around 1974, which corresponds to the greater rainfall in Australia around the period shown in *Diaz et al.* [1989]. Note that the amplitude of the CP_0 is smaller than the OP7s one around the period in though same trend can be seen in χ_2 between them. This suggests that the contribution of Australia to the CP_0 arises disagreement between the CP_0 and the OP, so that the land water storage model is considered not to reflect the hydrological cycle in the small continents.

Reservoir Model

The reservoir model reflects effects of the accumulation of precipitation anomaly that depends on decay constant τ_d in Eq (5), so that the magnitude of the calculated excitation pole is larger than that of the CP_0. Figure 2.10(a) and (b) show comparisons between the OP and a calculated excitation pole at $\tau_d = 3.7$ (hereafter, $CP_{3.7}$) when square of the OP minus the calculated excitation pole is minimum in the component of the oscillating direction in the OP shown in Figure 2.7, where the method to find τ_ds is defined as minimum $(O - C)^2$ in this study. The correlation coefficients in the component is 0.50. Note that the variation of the $CP_{3.7}$ is similar to that of CP_0 except that the amplitude of $CP_{3.7}$ is approximately three to four times larger than that of CP_0. The results suggest that the globally averaged relaxation time of precipitation, that is time to be needed for precipitation anomalies at one month to decrease their 1/e, is approximately 3.7 months under the land water storage model.

Behaviors in each continental contribution to the $CP_{3.7}$ agrees with those of the CP_0

shown in the lower part of Figure 2.9 very well though the figure is not shown here. The lower part of Figure 2.10(b) shows a calculated excitation pole at $\tau_d = 4.6$ in minimum $(O - C)^2$ when only two continental contributions of North America and Eurasia are considered (hereafter, $CP_{4.6}(NA + EU)$ following the abbreviations in Figure 2.8). Note that the behaviors are similar to $CP_{3.7}$ especially in χ_2, and that the trend become closer to the OP in χ_1 around 1974 due to removal of the contribution by Australia as mentioned in the non-reservoir model.

The τ_ds increase of 1.1 months in the $CP_{4.6}(NA + EU)$ as against that in the $CP_{3.7}$ principally corresponds to a decrease of land area used in the model computation. However, if the OP mainly reflects the variations of land water storage in the two continents due to their large capacity to reserve the land water, τ_d of 4.6 is interpreted as more natural decay time of precipitation than that of 3.7.

Figure 2.10(c) shows calculated excitation poles at minimum $(O - C)^2$ by removing land whose length from the ocean is less than about 500 km in the reservoir model. Both τ_ds in Figure 2.10(c) increase about two month from those of Figure 2.9(b). As similar to Figure 2.9(b), significant differences can not be seen between the global contribution and the two continental contribution. On the other hand, some differences of behaviors in each contribution between Figure 2.10(b) and Figure 2.10(c) can be seen, for example, interannual variations shown in the former around 1978 disappear in the letter. It reflects that τ_d plays a role of low-pass filter. In the end, these suggest that inland regions in North America and Eurasia are closely related with the ten-yearly variation in OP. A evaluation of minimum $(O - C)^2$ by removing land whose length from the ocean is less than about 1,000 km in the reservoir model shows no extremum due to significant decrease of land area.

2.2.5 Discussion

Ten-yearly Sinusoids

The OP and the calculated excitation poles in Figure 2.10(a) and Figure 2.10(b) show the maximal spectrum power just around ten years; the OP is 10.5 years, the $CP_{3.7}$ and the $CP_{4.6}(NA + EU)$ is 10.6 years. Rotational components of the three excitation poles based on sinusoidal fit at the period of ten years for 1967 to 1988 are shown in Figure 2.11 as three ellipsoids. The open circles indicate the one-yearly phases, the solid circles correspond to its origins of 1976, and arrows show the direction of the motion. The direction of major axis in ellipsoid of the OP, which points to North America and Eurasia, nearly agrees with those of the two calculated excitation poles, especially in the $CP_{4.6}(NA + EU)$. In addition, the ellipsoid of the and that of are similar. This facts suggest that variations of the land water storage in North America and Eurasia are essential in excitation of the OP.

On the other hand, phases of the two calculated excitation poles lead that of OP at about 1 year as suggested in Figure 2.9 and Figure 2.10. The fact shows that variations of the land water storage can be excitation source of the OP because the calculated excitation pole always leads the OP and the phase lags are small; approximately one tenth of ten years. Note that differences of the magnitude between the OP and the $CP_{4.6}(NA + EU)$ significantly decreases at 6 to 7 of τ_d in the reservoir model when the phase lag of about 1 year is not considered. It suggests that most of the will be explained by redistribution of the land water storage in North America and Eurasia if accurate and comprehensive data of precipitation is obtained.

The phase lags do not decrease significantly even if τ_d increase. For example, phase lags between the OP and the calculated excitation poles become only 1-2 month smaller even if τ_d become 20.0. It shows the limits to express the natural land water storage in the reservoir model. Thus, the new parameters should be considered such as movement of water among the lateral grids to account for the phase differences. In addition, consideration of water mass restricted in same place for several months to several years such as snow, ice, permafrost and hydrological reservoirs are needed.

In the effects mentioned above, freezing effects of the precipitation in winter season are considered to be one of the most efficient effects to preserve precipitation anomalies in each grid for several months, especially in North America and Eurasian. *Walland and Simmonds* [1997] have shown decadal variations of the area covered with snow in North America and Eurasia with the data of snow distribution observed by NOAA/ NESDIS satellite. In their Fig. 3, a see-saw like variation of the snow cover can be seen between the two continents corresponding to the results in this study. This suggests that redistribution of the snow mass may excite the ten-yearly polar motion.

However, it is difficult to accurately estimate the snow mass based on satellite image of the snow cover. Then, snow mass excitation of the polar motion is evaluated based on a simple freezing model of precipitation as the same way of *Hinnov and Wison* [1987]; precipitation in each grid is accumulated in the grid during the period that surface air temperature there is less than 0 degree Celsius. Data of precipitation and surface air temperature in each $5^o \times 5^o$ grid are computed from those station data compiled by NOAA to average them in each grid. The number of station in the precipitation data decrease rapidly after 1989, so that possible period to discuss is limited as mentioned in section 2.2.3.

The results show that magnitude of the calculated excitation pole is approximately one fifth of the *OP* on decadal time-scale and behaviors of them are not so similar as those on the reservoir model. These suggest that snow mass variations are not so important for the excitation of ten-yearly polar motion as precipitation changes.

The line in the center of Figure 2.10 shows the periodic excitation pole after ten-yearly sinusoidal fit based on atmospheric pressure in the Northern Hemisphere, which is approximately one tenth of the *OP* . Its small contribution to the on decadal time-scale in comparison with that of the land water storage is contrast to the case of annual wobble whose excitation sources are mainly seasonal variation of atmospheric pressure in the continents, and relatively small contributions by wind and the land water storage. For example, *Kuehne and Wilson* [1991] have shown that the storage of the land water storage is minor contributor to the annual wobble. They also have compared the power spectrums between the polar motion excited by changes of water storage and that by changes of atmospheric pressure, and have suggested that the variations of water storage become a dominant cause of excitation pole in the period longer than several years. The results in this study supports their results. Thus, it is shown that the major meteorological excitation sources of the polar motion differ with the time-scale.

Figure 2.12 shows a correlation map between precipitation change in each grid and the variation of the *OP* along the principal axis shown in Figure 2.11, that is the direction of the oscillation in Figure 2.7, i.e., $95^{\circ}E$ and $126^{\circ}W$ direction. In around $45^{\circ}N$, positive correlation can be seen in North America, and negative correlation, in western Eurasia. The seesaw-like patterns of the both are nearly $Y_{2,1}$ mode, which excite the polar motion most effectively. The trends are also confirmed in the continental contributions to the CP_0 shown in the lower part of Figure 2.9(b). These results suggest that precipitation changes in North America and western Eurasia are the major excitation sources of the ten-yearly polar motion.

Chao and O'Connor [1988] have shown that the seasonal changes of snow and rainfall in the North America and Eurasian are comparable in total mass, so that a large cancellation between their contributions to the polar motion is achieved on seasonal time-scale. Figure 2.12 also shows that the characteristics is different on decadal time-scale. The inverse-correlation pattern between North America and western Eurasia promote the amplitude of the ten-yearly polar motion each other. Assuming that the water mass between North America and western Eurasia is conserved in the two regions in a rough approximation, the anomalies of water mass are considered to move between the two regions through the North Atlantic Ocean since the most rivers in the both regions run off into the North Atlantic Ocean or the Arctic Ocean.

On the other hand, in Eurasian, seesaw-like variation of precipitation can be seen between the western region and the eastern region though the signal of eastern Eurasia is weaker than other regions. The fact suggests that the anomalies of the water mass propagate eastward on decadal time-scale in the mid latitude where the westerly are prominent. The hypothesis is supported by the nature of counterclockwise rotation of the OP, the $CP_{3.7}$, and the $CP_{4.6}(NA + EU)$ as shown in Figure 2.11. The rainfall trapped in land subsurface around the river basin, vegetation, and reservoirs are considered to be sources for new precipitation which propagate slowly in the lateral grids. *Chao* [1988] has confirmed that the levels for the North American Great Lakes fluctuate on time-scale of 10-20 years. It is one of the visible phenomenon in the trapped water listed above. The decadal water mass transportation also may affect the condition of the atmosphere indirectly in connection with the NAO teleconnection patter through interactions between atmosphere and land surface.

Moreover, Figure 2.12 also shows that the variations of precipitation in tropical region of Africa have strong negative correlation with the OP. This may reflect decadal drought in Sahel [e.g. *Rowell*, 1995]. However, the contribution to the polar motion is considered to be small because the phenomena arise in the tropical regions as suggested by Eq. (1). Noteworthy is that the lower panel of Figure 2.9(b) indicate that the excitation in Africa correlates inversely with Australia. These suggest some global connections of the decadal drought in Sahel with the NAO and the SO as *Folland et al.* [1986] have shown that it connects strongly with global SST anomaly.

Hydrologic Cycle Connected with NAO

On the decadal time-scale, it has shown that the variations of precipitation in North America and Eurasia can explain about 37% of the OP with the reservoir model, and that the calculated excitation pole become close to OP if τ_d is 6 to 7 in the model computation. In addition, it has been confirmed that the OP, the NAO index, and sea level changes along the both coastal regions in the North Atlantic Ocean change similarly [*Iwabuchi et al.* 1997]. To link these decadal phenomena at the viewpoint of the polar motion, a new look on a hydrological cycle centered in the North Atlantic Ocean is advocated as shown in Figure 2.13. The mechanism in this feedback system is illustrated as the following.

Most of precipitation in North America and Eurasian runs out either into the North Atlantic Ocean or into the Arctic Ocean due to topographical condition of the lands. Thus, the freshwater anomaly in the sub-surface of the North Atlantic Ocean is induced by precipitation changes in the both continents. Some part of the coastal sea level changes in the North Atlantic Ocean (section 2.1.5, e.g. *Iwabuchi et al.* 1997] are considered to reflect the freshwater anomaly.

The buoyant force fluctuation related to the salinity changes in the sub-surface ocean arise SST anomaly due to winter vertical mixing in the upper ocean. The decadal SST variations are confirmed to be particular in the North Atlantic Ocean [e.g. *Deser and Blackmon*, 1993]. Moreover, *Houghton* [1996] has also shown that the decadal fluctuation in the North Atlantic Ocean is likely to be related to surface forcing and upper-ocean mixing. He consider that the local precipitation, river runoff, and arctic ice or freshwater outflow are potential freshwater sources.

The anomaly of thermal energy in upper ocean, which is induced by decadal variation of SST, propagates to the atmosphere quickly through strong thermal interaction between ocean and atmosphere. The signals of change in atmospheric condition on decadal time-scale are reflected in changes of the NAO index. The winter sea ice anomalies, for example in the Davis Strait/ Labrador Sea region pointed by *Deser and Blackmon* [1993], may reflect the changes of the atmospheric conditions. The sea ice anomalies are also important sources for the fresh water anomaly though their feedback are not considered in this hydrological cycle model.

The decadal climate changes related to the NAO teleconnection pattern arise the variation of transportation patterns of the water vapor. As the result, precipitation changes are induced in the scale of the Northern Hemisphere. Here, movements of the water mass among the lateral grids, which can not be explained by the land water storage model, generate the phase lag between and the calculated excitation pole. In the end, the hydrological cycle plays an important role in the feedback system, which fixes the time-scale of the system. The ten-yearly polar motion is excited by mass redistribution of the land water storage which concerns precipitation changes in North America and Eurasia.

2.2.6 Conclusions

A model on decadal hydrological cycle is advocated to link the facts of observations; the NAO index, coastal sea level changes in the North Atlantic Ocean, and precipitation changes in North American continents and Eurasian continents. Here, the ten-yearly polar motion is excited by variations of the land water storage supplied by the precipitation in the both two continents. Further verification on this model needs comprehensive and precise data sets on the pathway of the rivers, evaporation, run-off, reservoirs, prosperity and decay of the glaciers, and the permanent freezing soil. Since it takes much time, however, to acquire the sufficient reliable data, the evaluations using the climate model coupled with the hydrologic system and the land surface process are considered as the alternative approach.

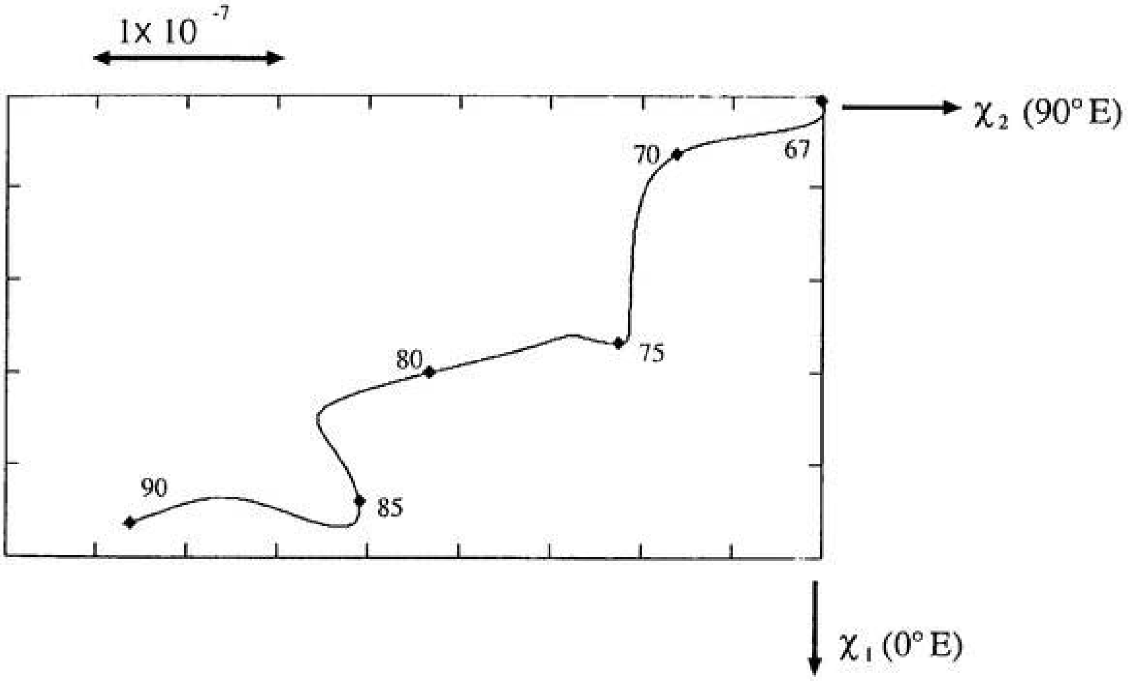

Figure 2.1: Variation of the excitation pole computed from the observed polar motion for the period 1962-1994 based on IPMS and SPACE94 data sets. Five-year low-pass-filter is used. Unit 1×10^{-7} of the non-dimensional excitation function in the figure corresponds to 64 cm on the Earth's surface. After *Kikuchi and Naito* [1995].

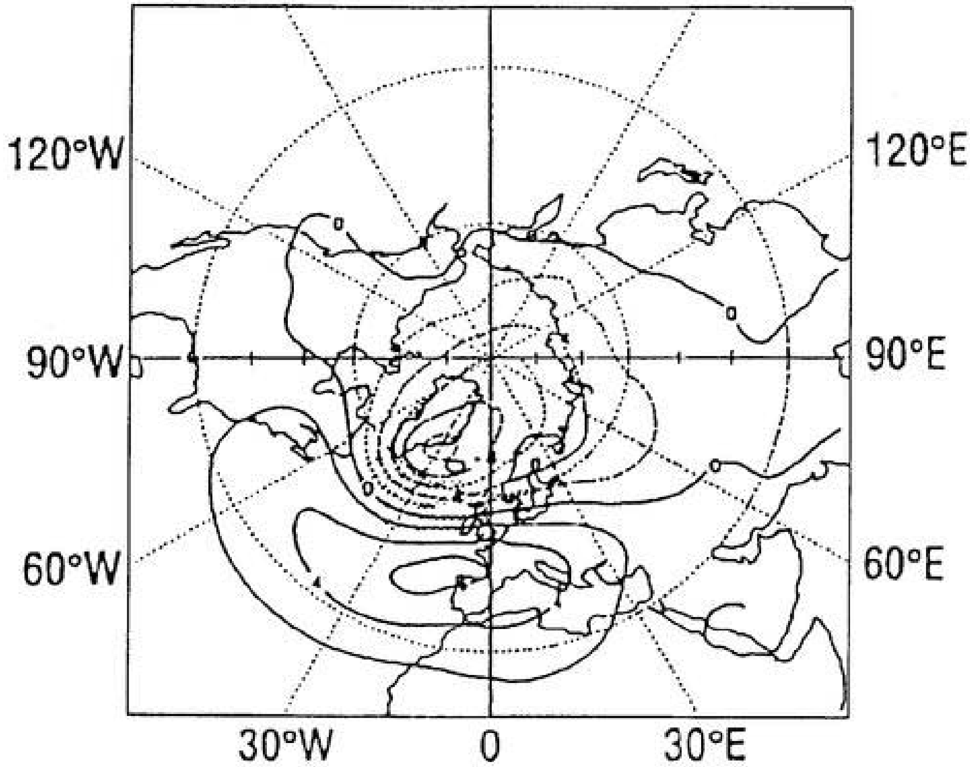

Figure 2.2: Difference in sea level atmospheric pressure (hPa) between high index minus low index of the North Atlantic Oscillation (NAO) [after *Hurell*, 1995], which shows the typical NAO teleconnection pattern. Dashed contour lines show negative values.

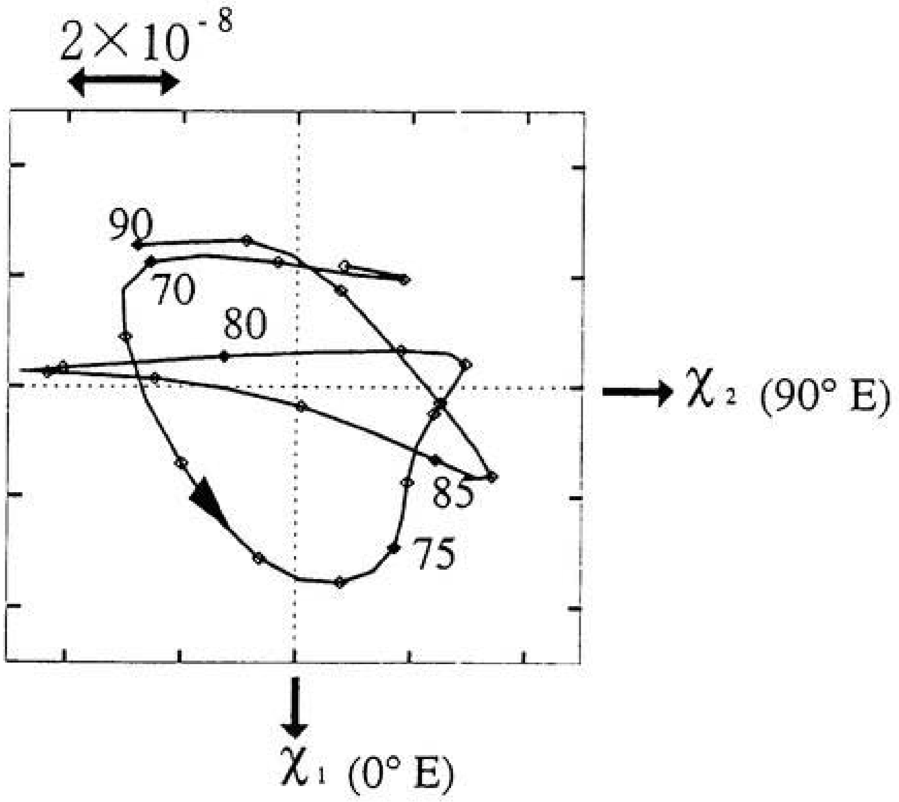

Figure 2.3: The ten-yearly motion of the observed excitation pole after removing the secular variation and bias (see Fig. 2.1). Note that the excitation pole rotates counterclockwise. Unit 2×10^{-8} in the figure corresponds to 13 cm on the Earth's surface.

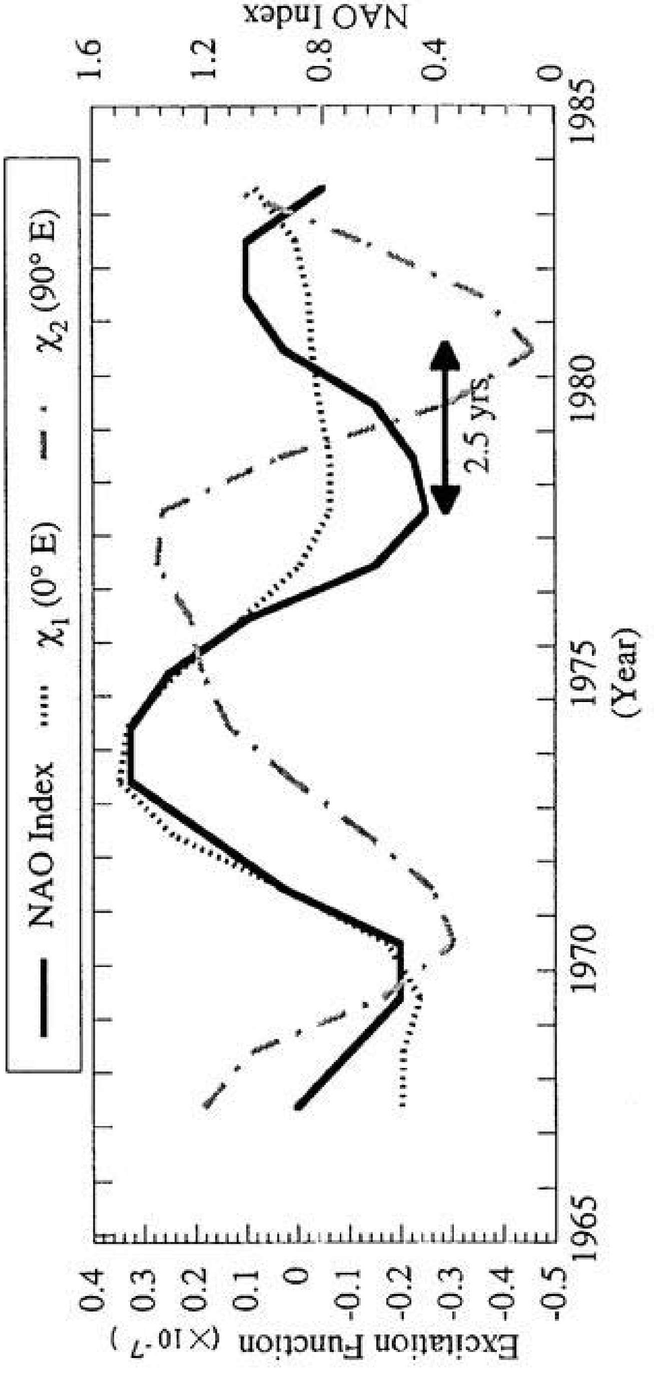

Figure 2.4: Variations of the excitation pole and the NAO index on decadal time-scale. Some correlation can be seen between χ_1 and the NAO index with 0 year lag and between χ_2 and the NAO index with 2.5 years lags.

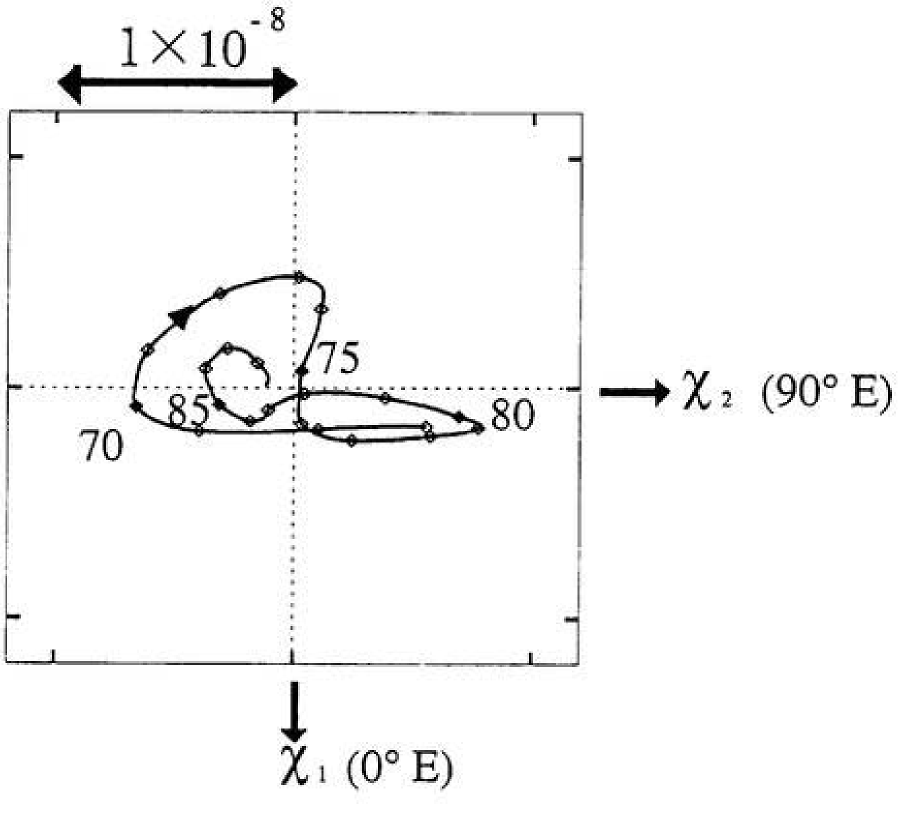

Figure 2.5: Calculated motion of the excitation pole from the atmospheric pressure data in the Northern Hemisphere. Magnitude of variation is about one fifth of that of the observed excitation pole in Fig. 2.3. Note that the pole rotates clockwise. Unit 1×10^{-8} in the figure corresponds to 6.5 cm on the Earth's surface.

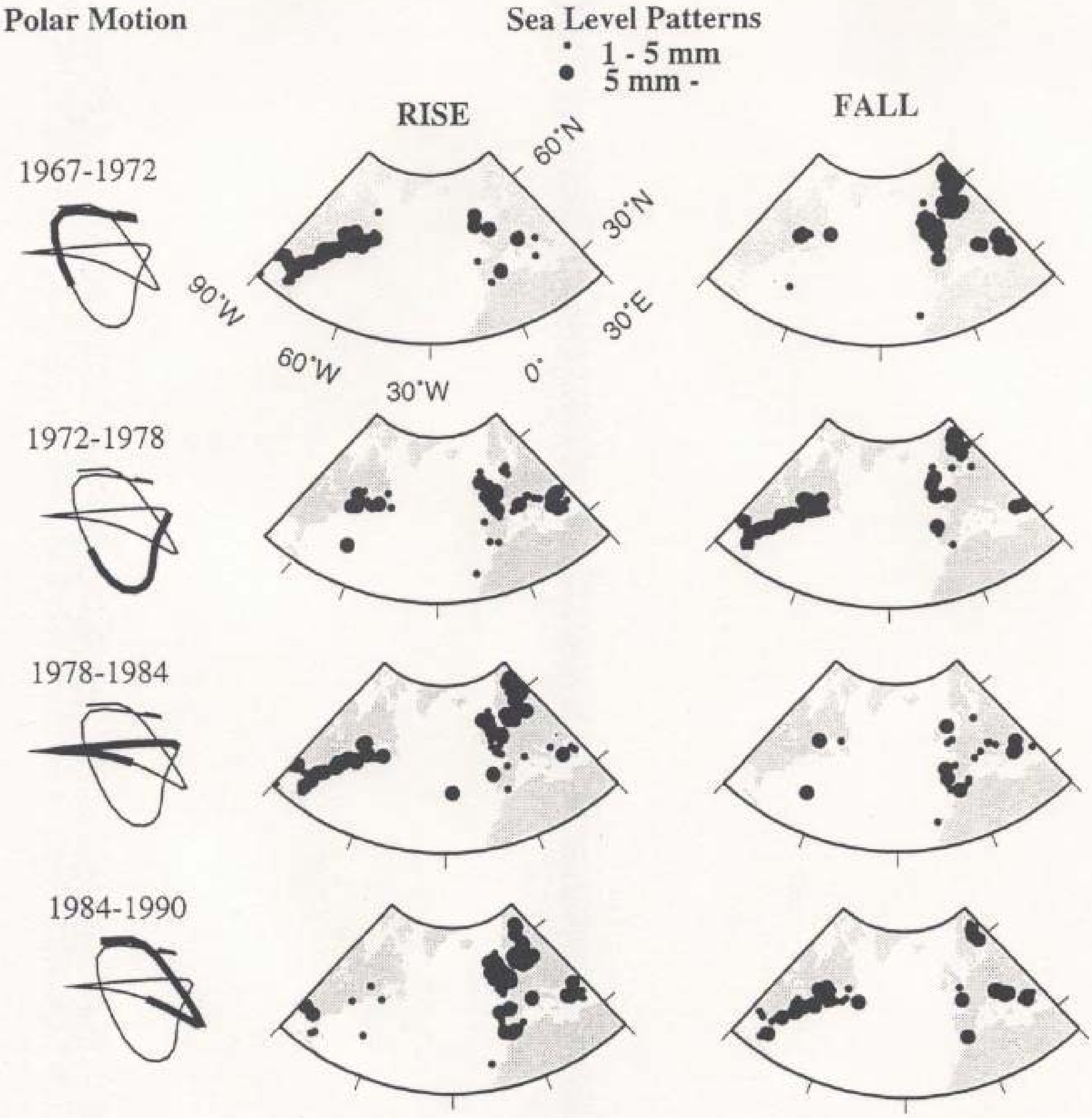

Figure 2.6: Sea level changes corresponding to the ten-yearly polar motion of the excitation pole in Fig. 2.3. The left column shows the period divided into typical two types of phase in the ten-yearly excitation pole, and the middle and right columns show rise and fall patterns in the sea level, respectively.

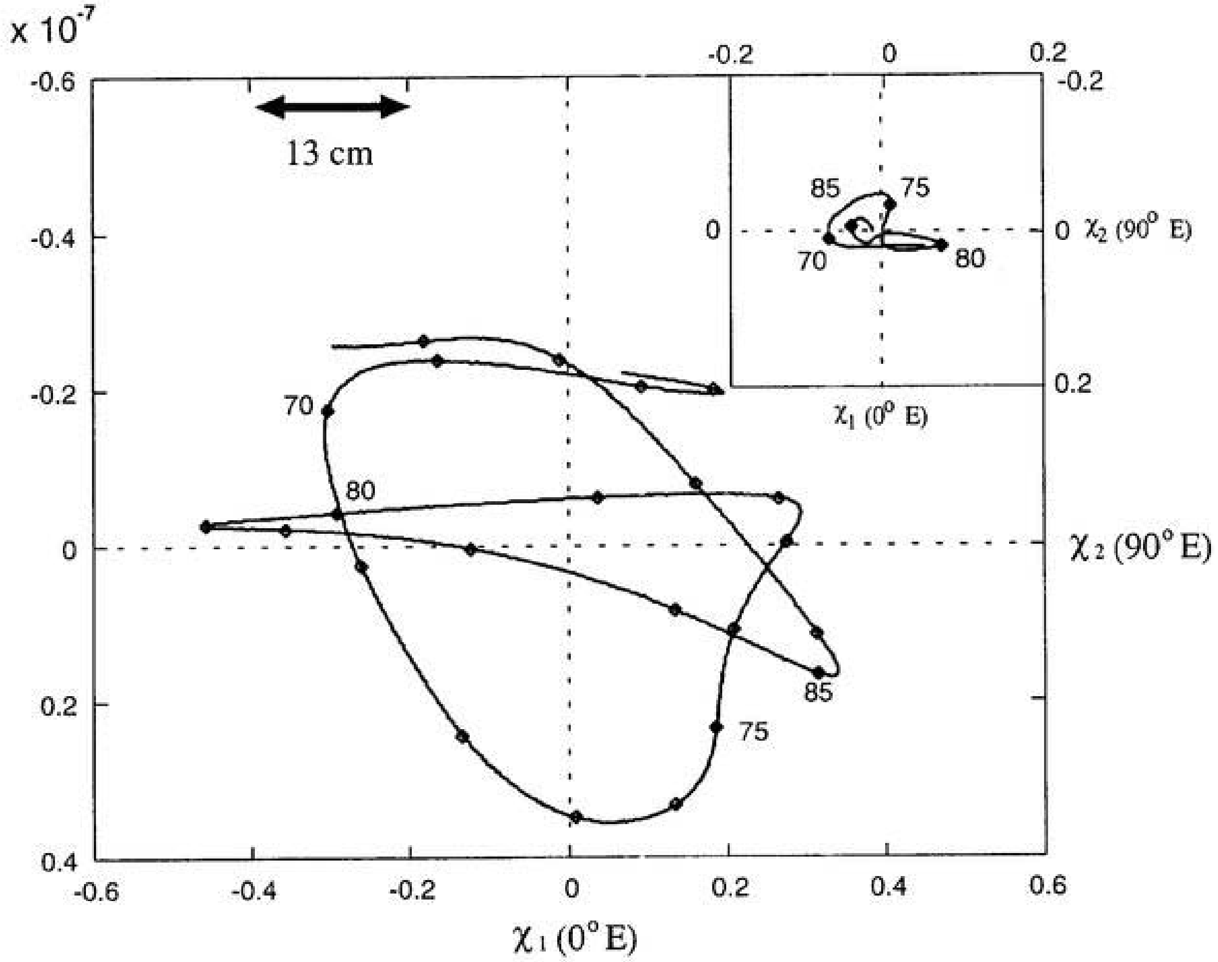

Figure 2.7: The ten-yearly motion of the observed excitation pole (central curve, hereafter, *OP*) computed from the IPMS and SPACE94 data and the decadal motion of calculated excitation pole (right upper curve) based on atmospheric pressure data set in the Northern Hemisphere, where both are five-year low pass filtered and then detrended excitation poles. Unit 0.2×10^{-7} of change in excitation pole corresponds to approximately 13 cm of Earth's surface. The dotted arrow shows the principal axis evaluated to fit 10 years period of sinusoid to the *OP*. The direction of the oscillation in the *OP* of approximately 40 cm is almost between $59°E$ and $126°W$. After *Iwabuchi et al.* [1997].

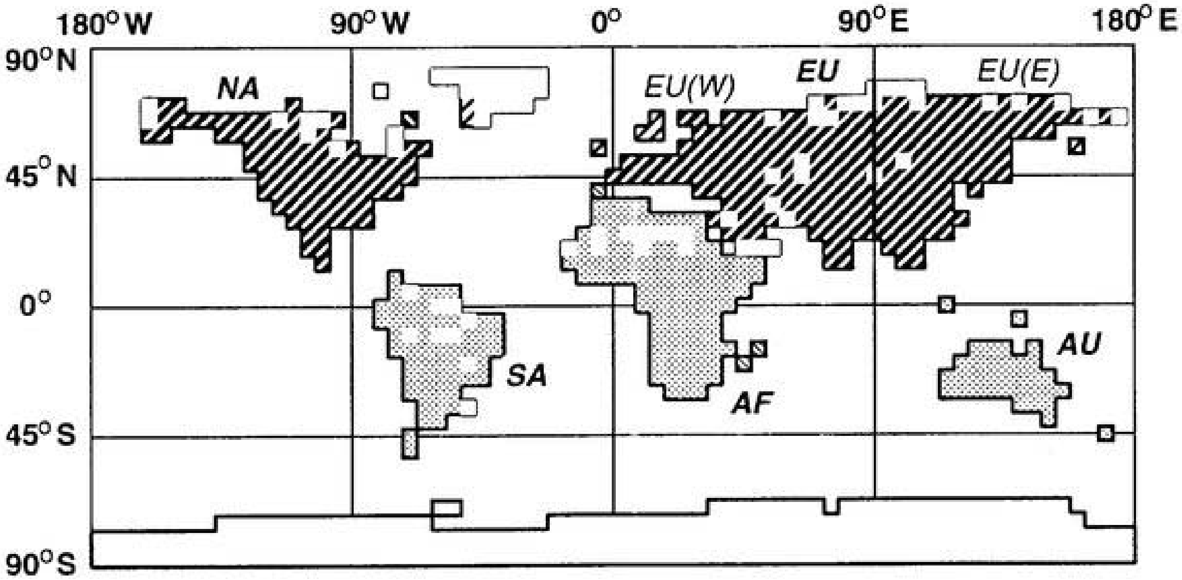

Figure 2.8: Map showing the distribution of the precipitation data for 5° × 5° grid in continents. Blank grids are not used here because continuous data for the period 1960-1985 is not available. Abbreviations NA, SA, EU, AF, and AU show North America, South America, Eurasia, Africa, and Australia. $90°E$ line is defined in this study as boundary between the western and eastern region of Eurasia, EU(W) and EU(E), respectively.

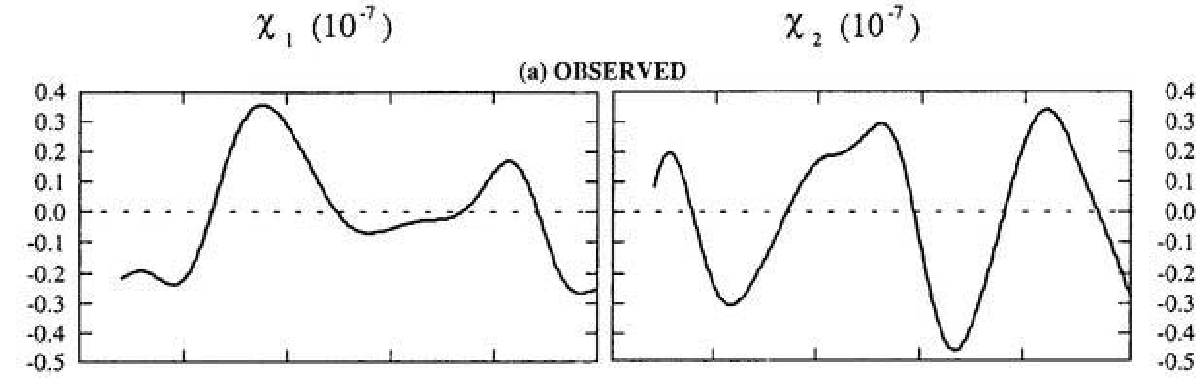

(b) CALCULATED (τ_d=0)

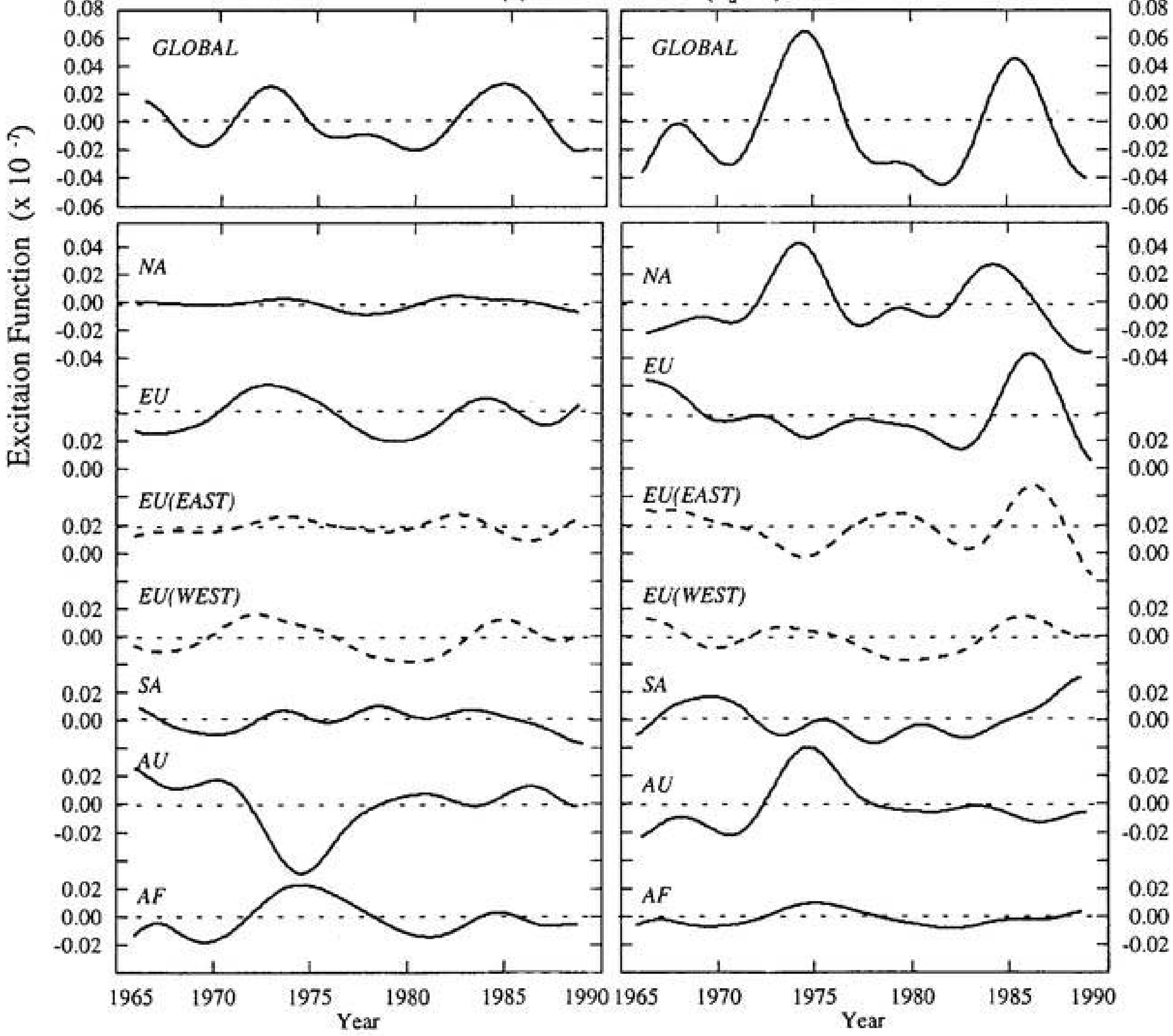

Figure 2.9: The ten-yearly variations in χ_1 ($0^o E$) and χ_2 ($90^o E$) components of (a) observed motion of excitation pole and (b) calculated motions of excitation pole at $m = 0$ in Eqs. (4) and (5) based on the non-reservoir model of the land water supplied by precipitation. Upper panels in (b) shown as GLOBAL indicate global contribution to the excitation pole (hereafter, CP_0) and the lower panels shown as abbreviations defined in Fig. 2.8 indicate each continental contribution. The correlation coefficient between the OP and the CP_0 in the direction of the oscillation shown is 0.50. The χ_2 of North America and western Eurasia in the CP_0 changes similarly with that of the OP .

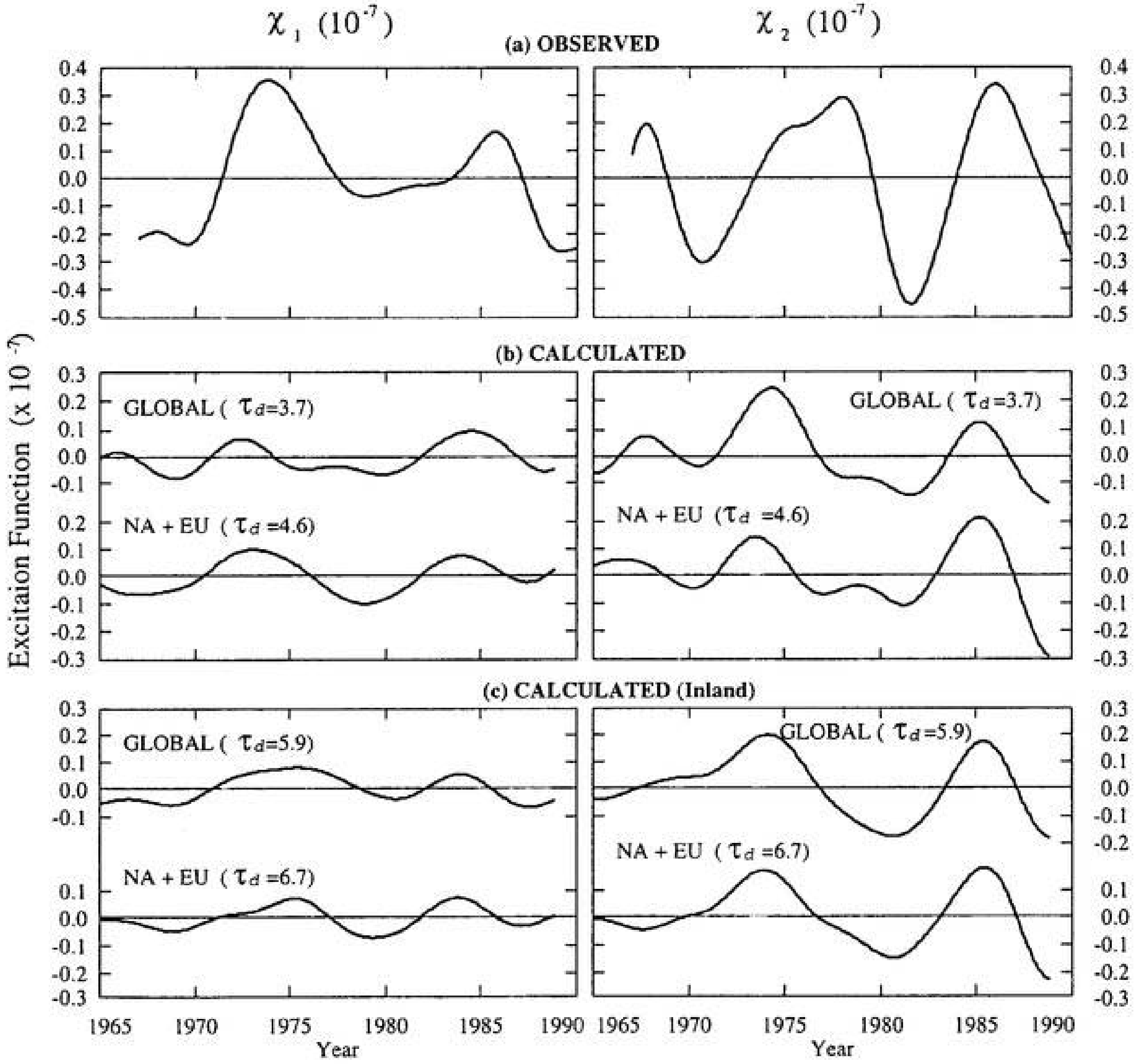

Figure 2.10: Ten-yearly variations in χ_1 and χ_2 components of (a) observed excitation pole, (b) calculated excitation pole at decay parameter of precipitation $\tau_d = 3.7$ (hereafter, $CP_{3.7}$) and one at $\tau_d = 4.6$ when only two continental contributions of NA and EU are considered (hereafter, $CP_{4.6}(NA + EU)$), and (c) same as (b) but at $\tau_d = 5.9$ and 6.7. These τ_ds are derived from evaluation that square of the difference between the observed and the calculated excitation poles are minimum.

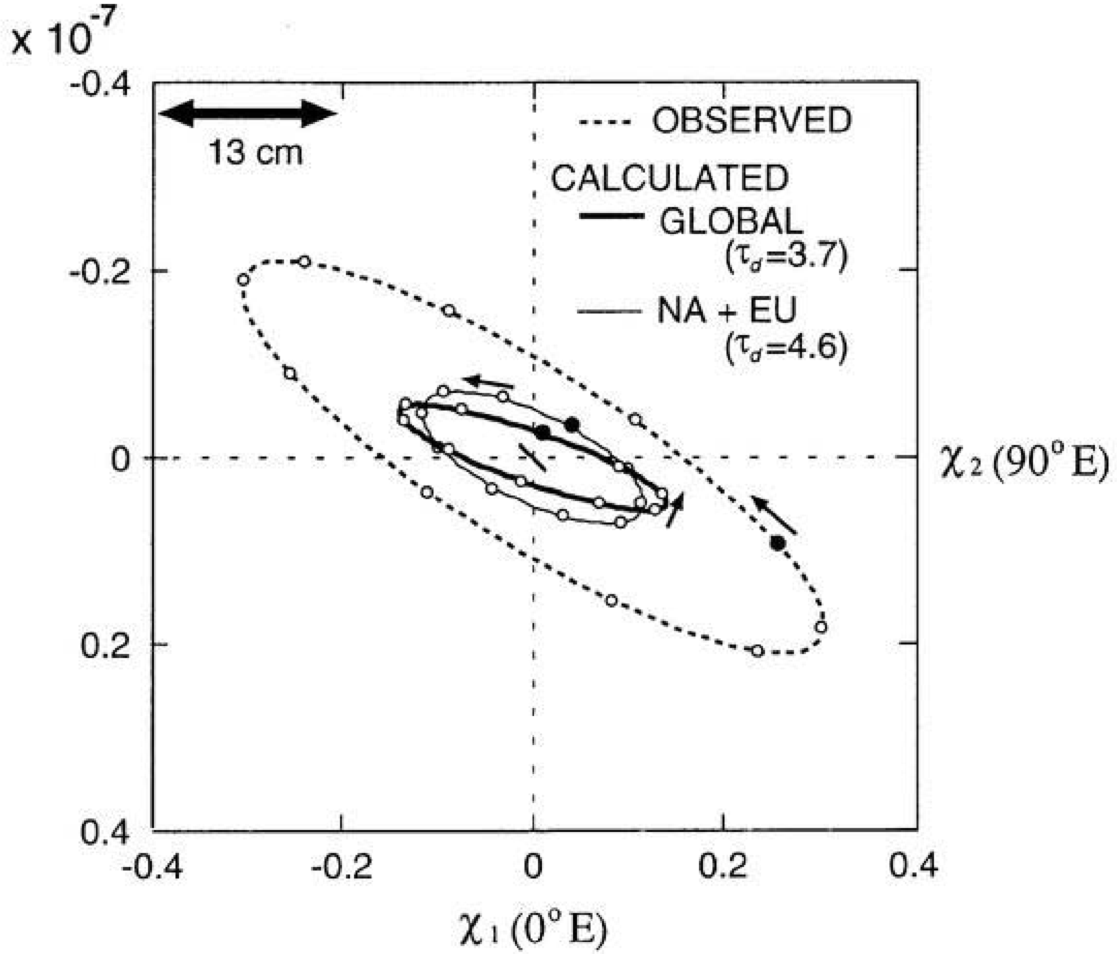

Figure 2.11: The periodic motion of excitation poles obtained by least square fit of 10 years period of sinusoid to the variations of the excitation pole for 1967 to 1988 seen in Fig. 2.10a and 2.10b. The observed excitation pole (dotted line), calculated excitation pole of the $CP_{3.7}$ (thick solid line), calculated excitation pole of the $CP_{4.6}(NA + EU)$ (thin solid line), and calculated excitation pole based on atmospheric pressure data (small line in the center of this figure) are shown. The phase and direction of the motions are shown with circles and arrows, respectively. Black circles indicate the origin of the motion corresponding to 1967.

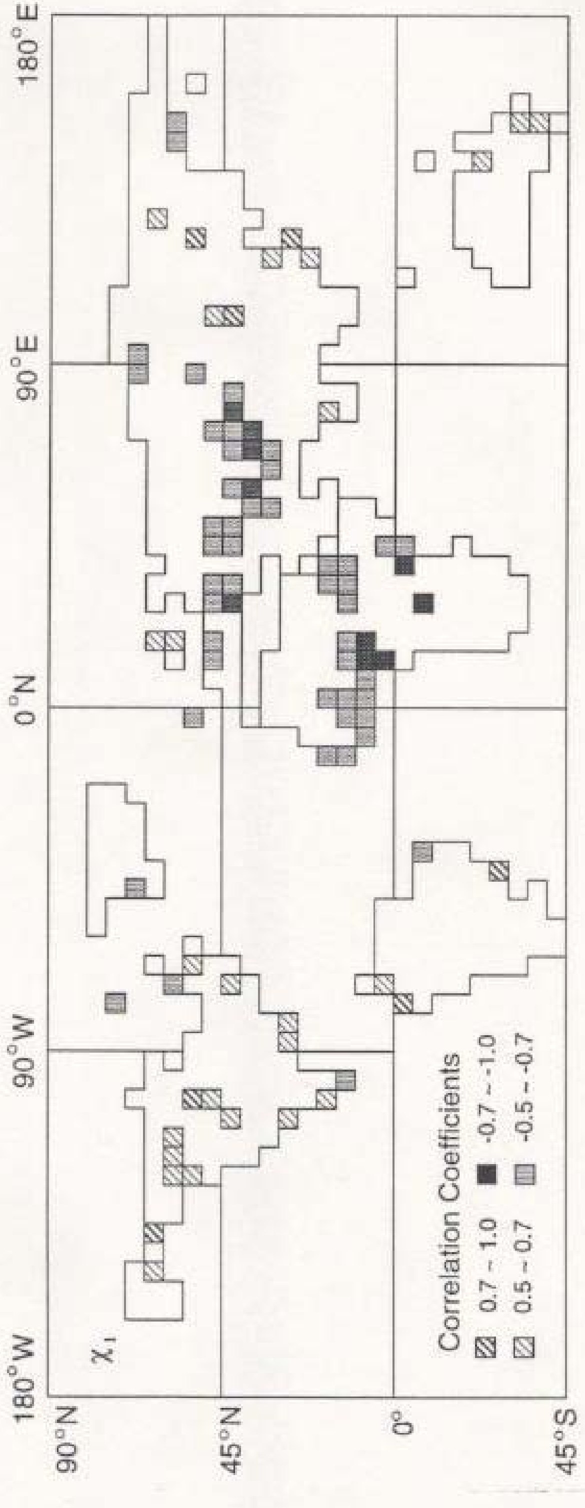

Figure 2.12: Map showing correlation coefficient between precipitation changes in each grid and the variation of the component along the principal axis in the *OP* of Fig. 2.11, that is the direction of the oscillation. Seesaw-like variations of the precipitation connected to the polar motion can be seen between the North America and western Eurasia.

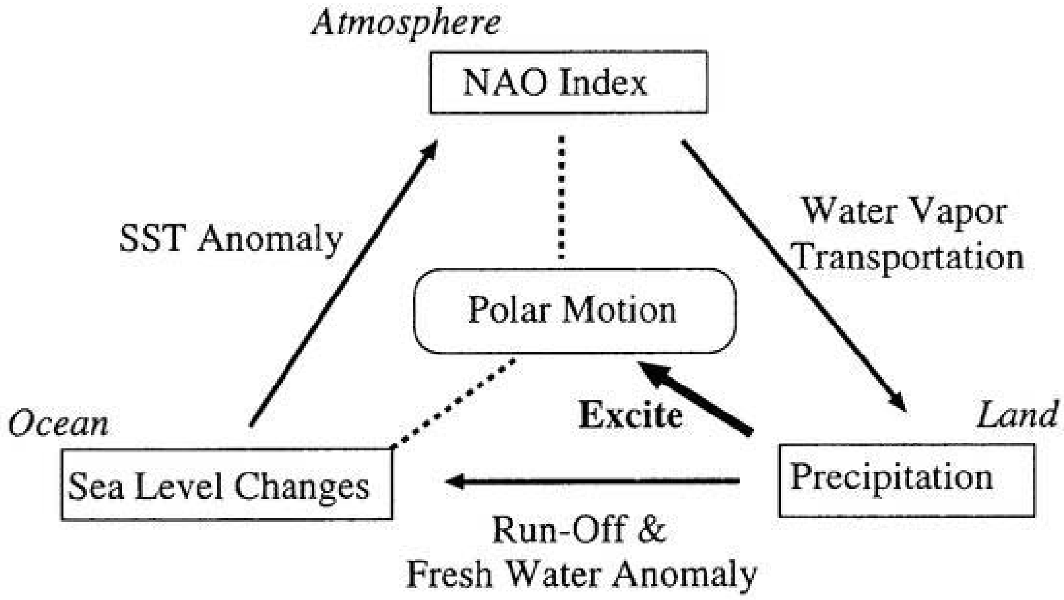

Figure 2.13: A Model showing the hydrological cycle connected with the NAO, in which water plays important role in the feedback system. Thick arrows and dotted lines denote the direction of action and existence of the correlation, respectively. The observed ten-yearly polar motion can be explained by the redistribution of the land water supplied by precipitation in the North American continent and Western region of the Eurasian continent.

Bibliography

[*Anderson and Willebrand*, 1996] Anderson, D. L. T., and J. Willebrand (Eds.), Decadal Climate Variability: Dynamics and Predictability. 44, Global Environmental Change, NATO ASI Series, Springer, 493 pp, 1996.

[*Barnes et al.*, 1983] Barnes, R. T. H., R. Hide, A. A. White, and C. A. Wilson, Atmospheric Angular Momentum Function, Length-of-Day Changes and Polar Motion, Proc. E. Soc. Lond., A387, 31-73, 1983.

[*Bradley et al.*, 1987] Bradley, R. S., H. F. Diaz, J. K. Eischeid, P. D. Jones, P. M. Kelly, C. M. Goodess, Precipitation Fluctuations over Northern Hemisphere Land Areas Since the Mid-19th Century, *Science,* **237,** 171-175, 1987.

[*Chao et al.*, 1987] Chao, B. F., W. P. O'Connor, A. T. C. Chang, D. K. Hall, and J. L. Foster, Snow Load Effect on the Earth's Rotation and Gravitational Field, 1979-1985, *J. Geophys. Res.* **92,** 9415-9422, 1987.

[*Chao and Au*, 1991] Chao, B . F., and A. Y. Au, Atmospheric Excitation of the Earth's Annual Wobble: 1980-1988, *J. Geophys. Res.,* **96,** 6577-6582., 1991

[*Chao and Zhou*, 1997] Chao, B. F., Y. Zhou, Meteorological Excitation of Interannual Polar Motion by the North Atlantic Oscillation, *J. Geodynamics,* in press, 1997.

[*Chao and O'Connor*, 1988] Chao, B. F., W. P. O'Connor, Global surface-water-induced seasonal variations in the Earth's rotation and gravity field. *Geophys. J.* **94,** 263-270, 1988.

[*Chao*, 1988] Chao, B. F., Excitation of the Earth's Polar Motion due to Mass Variations in Major Hydrological Reservoirs. *J. Geophys. Res.,* **93,** 13,811-13,819, 1988.

[*Deser and Blackmon*, 1993] Deser, C. and M. L. Blackmon, Surface Climate Variations over the North Atlantic Ocean during Winter: 1900-1989, *J. Climate,* **6,** 1743-1753, 1993.

[*Diaz et al.*, 1989] Diaz, H. F., R. S. Bradley, and J. K. Eischeid, Precipitation Fluctuations Over Global Land Areas Since the Late 1800's. *J. Geophys. Res.,* **94,** 1195-1210, 1989.

[*Eubanks*, 1993] Eubanks, T. M., Variations in the Orientation of the Earth, in Contributions of Space Geodesy to Geodynamics: Earth Dynamics, 24, pp. 1-54, eds. Smith, D. E. and Turcotte, D. L., American Geophysical Union, Washington, DC., 1993.

[*Groger and Plag*, 1993] Groger, M., H. -P. Plag, Estimations of a Global Sea Level Trend: Limitations from the Structure of the PSMSL Global Sea Level Data Set, *Global and Planetary Change,* **8,** 161-179, 1993.

[*Gross*, 1996] Gross, R. S., Combinations of Earth Orientation Measurements: SPACE94, COMB94, and POLE94, *J. Geophys. Res. 101,* **8729-8740,** 1996.

[*Hinnov*, 1987] Hinnov, L. A. and C. R. Wilson, An Estimate of the Water Storage Contribution to the Excitation of Polar Motion, *Geophys. J. R. astr. Soc.,* **88,** 437-459, 1987.

[*Houghton*, 1996] Houghton, R. W., Subsurface Quasi-Decadal Fluctuations in the North Atlantic, *J. Climate,* **9,** 1363-1373, 1996.

[*Hurrell*, 1995] Hurrell, J. W., Decadal Trends in the North Atlantic Oscillation: Regional Temperatures and Precipitation, *Science,* **269,** 676-679, 1995.

[*Hurrell and van Loon]* Hurrell, J. W. and H. van Loon, Decadal Variations in Climate Associated with the North Atlantic Oscillation, *Climate Change,* **36,** 301-326, 1997.

[*Iwabuchi et al.*, 1997] Iwabuchi, T , K. Heki, I. Naito, Decadal Polar Motion Connected with Atmospheric Pressure and Sea Level Patterns over the North Atlantic Ocean, International Association of Geodesy Symposia

117. Segawa et al. (Eds.) Gravity, Geoid and Marine Geodesy, Springer-Verlag, 1997, 666-673.

[*Iwabuchi and Naito*, 1998] Iwabuchi, T. and I. Naito, Ten-yearly Polar Motion Connected with Precipitation Changes over North American and Eurasian Continents, submitted to J. Meteor. Soc. Japan, 1998.

[*Kikuchi and Naito*, 1995] Kikuchi, N. and I. Naito, Notes on Behaviors of the Polar Motion Based on ILS, IPMS, and SPACE94, *J. Geodetic Society of Japan,* **41,** 239-249, 1995.

[*Lambeck*, 1980] Lambeck, K., The Earth's Variable Rotation, Cambridge University Press, Cambridge, 1980.

[*Latif*, 1998] Latif, M., Dynamics of Interdecadal Variability in Coupled Ocean-Atmosphere Models, *J. Climate,* **11,** 602-624, 1998.

[*McCarthy and Luzum*, 1996] McCarthy, D. D. and B. J. Luzum, Path of the Mean Rotational Pole from 1899 to 1994, *Geophys. J. Int.* **125,** 623-629, 1996.

[*Mann and Park*, 1994] Mann, M. E., and J. Park, Global-Scale Modes of Surface Temperature Variability on Interannual to Century Time-scale, *J. Geophys. Res.,* **99,** 25,819-25,833, 1994.

[*Mann and Park*, 1996] Mann, M. E., and J. Park, Joint Spatiotemporal Modes of Surface Temperature and Sea Level Pressure Variability in the Northern Hemisphere during the Last Century, *J. Climate,* **9,** 2137-2162, 1996.

[*Munk and MacDonald*, 1960] Munk, W. H., and G. J. F. MacDonald, The Rotation of the Earth. Cambridge University Press, Cambridge, 323pp, 1960.

[*Nerem*, 1995] Nerem, R. S., Global Mean Sea Level Variations from TOPEX/ POSEIDON Altimeter Data, *Science,* **268,** 708-710, 1995.

[*Philander*, 1990] Philander, S. G., El Niño, La Niña and the Southern Oscillation. Academic, New York, 293pp, 1990.

[*Ponte*, 1991] Ponte, R. M., D. A. Salstein, and R. D. Rosen, Sea Level Response to Pressure Forcing in a Barotropic Numerical Model, *J. Phys. Oceanogr.,* **21,** 1043-1057, 1991.

[*Rowell*, 1995] Rowell, D. P., C. K. Folland, K. Maskell, and M. N. Ward, Variability of Summer Rainfall over Tropical North Africa (1906-1992): Observations and Modeling, *Quart. J. Roy. Met. Soc.,* **121,** 669-704, 1995.

[*Unal and Ghil*, 1995] Unal, Y. S., and M. Ghil, Interannual and Interdecadal Oscillation Pattern in Sea Level, *Clim. Dyn.,* **11,** 303-319, 1995.

[*Wahr*, 1983] Wahr, J. M., The Effects of the Atmosphere and Oceans on the Earth's Wobble and on the Seasonal Variations in the Length of Day - 1. Results, *Geophys. J. R. astr. Soc.,* **74,** 451-487, 1983.

[*Walker and Bliss*, 1932] Walker, G. T., and E. W. Bliss, World Weather, V., *Mem. Roy. Meteor. Soc.,* **4,** 53-84, 1932.

[*Wallace and Gutzler*, 1981] Wallace, J. M., and D. S. Gutzler, Teleconnections in the Geopotential Height Field during the Northern Hemisphere Winter, *Mon. Wea. Rev.,* **109,** 784-812, 1981.

[*Wallace*, 1996] Wallace, J. M., Observed Climatic Variability: Spatial Structure, Decadal Climate Variability: Dynamics and Predictability, 44, Anderson, D. L. T., and J. Willebrand (Eds.), Global Environmental Change, NATO ASI Series, Springer, 31-81, 1996.

[*Walland and Simmonds*, 1997] Walland, D. J., and I. Simmonds, North American and Eurasian Snow Cover Co-Variability, *Tellus,* **49A,** 503-512, 1997.

[*Wilson*, 1985] Wilson, C. R., Discrete Polar Motion Equations, *Geophys. J. R. astr. Soc.,* **80,** 551-554, 1985.

Chapter 3

GPS Retrieved Water Vapor

3.1 Behavior of GPS Retrieved Precipitable Water Vapors over the Japanese Islands

3.1.1 Abstract

Behavior of precipitable water vapor (PWV) routinely retrieved from the nationwide array of Global Positioning System (GPS) in Geographical Survey Institute (GSI) of Japan for monitoring of crustal deformation are visualized and compared with the Japan area objective analysis data for numerical weather prediction (NWP) in Japan Meteorological Agency (JMA). The array used here has a space resolution of about 50 km, and their PWV data are those converted from the three-hourly zenith tropospheric delay (ZTD) data obtained in GSI's routine GPS analysis system, where the conversions from ZTD data to PWV data are made by using the twelve-hourly Japan area objective analysis data for NWP in JMA.

While a front accompanying with heavy rainfalls moved eastward across the Japanese Islands during 9(LST) Sep. 1- 9(LST) Sep. 3, 1996, the temporal anomalies in GPS PWV moving along with the front are clearly detected with almost the same space resolution as in the array all over the islands. In the analysis period, dependency of PWV value obtained at each GPS site upon the GSI's routine GPS clustering analysis is found to be in 1 - 3 mm. Hence, if the fact that these PWV agree with those calculated from the radiosonde observations in JMA with rms difference of about 3 mm, as shown by *Ohtani and Naito* [1998], is taken into consideration, the above results reveal that GSI's GPS array can work as an all weather giant array sensor of PWV over the islands.

On the other hand, comparisons of GPS retrieved PWV with those from the Japan area

objective analysis data for NWP in JMA show that GPS PWV have large positive biases with respect to NWP PWV reaching about 10 mm in mountain areas due to large negative biases in the topographic height at the GPS sites located on the real topography with respect to that of the model topography employed in NWP. This results from a fact that GPS sites in GSI are almost located in valleys in mountain areas for conveniences. However, negative biases in GPS PWV amounting to 2 - 4 mm not due to the difference in the topographic heights are also found all over the islands.

3.1.2 Introduction

Global Positioning System (GPS) is a space based positioning system now widely used for navigation, relative positioning, time transfer (see Appendix B.1). Recent progress in prediction system of GPS satellite orbits as well as in GPS analysis software has made it possible to accurately estimate not only the positional parameters such as latitude, longitude and height on the ground but also propagation delay at zenith angle of GPS microwaves in atmosphere above the ground. The propagation delay is caused in ionosphere and neutral atmosphere, where the ionospheric delay can be removed by determining phases of the GPS microwaves with strong dispersion relation in ionosphere.

The neutral atmospheric delay, which has been conventionally called tropospheric delay, can be in general expressed with sum of hydrostatic and wet delays. Since most GPS analysis software describes delays at arbitrary elevation angle as zenith delays multiplied by "mapping functions", dependence of delay on elevation angle, the tropospheric delay in GPS analysis are generally expressed by zenith tropospheric delay (ZTD) as sum of the zenith hydrostatic delay (ZHD) and the zenith wet delay (ZWD). ZHD has been known to depend only upon atmospheric pressure and then can be easily calculated from atmospheric pressure data observed at GPS site [*Davis et al.*, 1985]. Thus, ZWD can be obtained by subtracting ZHD from the determined ZTD in GPS data analysis.

Although a fact that ZWD is proportional to precipitable water vapor (PWV), integrated water vapor in atmospheric column above the ground, was found by *Hogg et al.* [1981], it was not applied to meteorology until the realization of GPS. As is now widely known, however, an application of GPS retrieved PWV to meteorology has been proposed as "Earth based GPS meteorology" [*Bevis et al.*, 1992; *Businger et al.*, 1996], although "satellite-based GPS meteorology" with low Earth orbiting satellites having GPS receiver by using the radio occultation technique has been proposed [*Ware et al.*, 1996; also see *Yuan et al.*, 1993]. Recent experimental studies have shown that GPS PWV have almost the same accuracy as those from radiosonde observations and from water vapor radiometries [*Rocken et al.*, 1993; *Rocken et al.*, 1995; *Duan et al.*, 1996; *Elgered et al.*, 1997; etc.].

On the other hand, information on the atmospheric water vapor is essential in predictions not only of a global change of climate but also of rainfall phenomena on meso- to- local scale. In particular, water vapor information with high space-time resolution is urgently needed for numerical prediction of localized torrential rains, that caused serious damages in every rainy season in the western part of Japan, for example. In these circumstances, Geographical Survey Institute (GSI) has deployed the nationwide dense GPS array to monitor crustal deformation for earthquake prediction researches. The array will have 950 GPS sites in 1998 [*Miyazaki et al.*, 1997], which corresponds to a space resolution of about 30 km enough for the above requirements.

In the GPS analysis of GSI's array, three-hourly ZTD have been routinely estimated together with the daily coordinates of the sites and filed with the Software INdependent EXchange (SINEX) format. *Ohtani and Naito* [1998] have shown that PWV obtained from GPS ZTD in GSI's SINEX data agree well with PWV calculated from radiosonde observations in Japan Meteorological Agency (JMA) located near the GPS sites over Japan with rms difference of about 3 mm, where ZHD and the conversions from GPS ZWD to PWV are based upon the radiosonde data. It should be noted here that the rms difference of about 3 mm is surprisingly small, if mean distance of about ten km between the GPS sites and the radiosonde stations is taken into consideration. Hence, PWV data thus obtained from the GPS array can be expected to contribute to the regional 4-dimensional data assimilation (4DDA) system for numerical weather prediction (NWP) in JMA.

There are various problems to be clarified, however, before applying these GPS PWV data to NWP. Especially, important is a point how the PWV at GPS sites close to each others behave in comparison with those at GPS sites distant each other. This is because PWV retrieved from GPS network with apertures smaller than about 500 km possibly have unknown biases due to incomplete separations of ZTD correlating with each other in GPS analysis, as described in Section 3.2 [see *Rocken et al.*, 1993, for details].

In addition, the above problem has closely connected with a point how much the clustering analysis of GPS data employed in GSI affects the PWV, since GSI's array is divided into several clusters with about 100 sites partly because different types of receivers are used in the array and partly because the volume of GPS data is too huge to analyze simultaneously. Therefore, the PWV retrieved from the different clusters may also involve systematic biases each others.

From view points of applications to NWP, it should also be confirmed how much the difference in height between real topography, on which GPS array are located, and modeled topography employed in NWP gives rise to the difference in PWV, in particular in mountain areas. A more basic interest is in how GPS PWV behaves during heavy rainfalls, by which an ability of GPS as PWV sensor can be evaluated.

Main purposes of this study are first to compute GPS PWV over the Japanese Islands based upon GSI's SINEX data retrieved when a front accompanied by heavy rainfalls moved eastward across the Japanese Islands, second to visualize them in order to see how they behave, and third to compare with meteorological data for NWP and discuss them from the above mentioned points of view. In the section, the details of GSI's array and outline of its routine analysis are described in Section 3.1,3, the GPS and meteorological data sets used in this analysis are described in Section 3.1.4. Behaviors of ZTD, ZHD, ZWD, PWV, and temporal anomalies of PWV visualized over the islands are respectively shown in Sections 3.1.5 and 3.1.6. Comparisons of GPS PWV with NWP PWV and effects of the GPS clustering analysis upon biases in GPS PWV are respectively discussed in Sections 3.1.7 and 3.1.8. In section 3.1.9 the results of analysis are summarized.

3.1.3 Nationwide GPS Array in GSI for Monitoring Crustal Deformation

Distribution of the Array

GSI has deployed the nationwide GPS array of 610 sites in 1996 [*Ohtani and Naito*, 1998]. The array is designed both to monitor crustal deformation and to serve as a high precision geodetic network. It is the densest GPS array operated routinely in the world, and will have about 950 sites in 1998 [*Miyazaki et al.*, 1997]. Mean separation of the sites is about 50 km for 610 sites, and 15-30 km for 950 sites. The GPS monuments of the array are set up in consideration of stable ground, wide over-view, electric power supply, availability of telephone lines, and accessibility to the sites [*e.g.*, *Miyazaki et al.*, 1997]. As a result, many GPS sites are located in valleys as shown in Fig. 3.1a.

In this analysis, GPS data of 556 sites in the 610 sites deployed in 1996 are used, where 27 sites of the remained 54 sites cannot provide continuous data during the analysis period mentioned in Section 3.1.4, and at the other 27 sites their heights above sea level cannot be known by using the following method.

As is mentioned in the previous section, heights at GPS sites above sea level are needed to calculate ZHD. Fig. 3.1a shows distribution of the height above sea level of the 556 GPS sites of GSI used in this study (then hereafter call this the real topographic height of

GPS sites), where the heights are calculated from the coordinates of GPS sites in SINEX data in GSI by using the conversion software "tky2wgsf Ver. 3.4" by *Tobita* [1994a, 1994b]. Since the conversion software uses the coordinates of World Geodetic System (WGS) 84 reference frame, and the coordinates in SINEX data are based on International Terrestrial Reference Frame (ITRF) for International Earth Rotation Service, the conversions are made by assuming ITRF coordinates to be identical to WGS84 coordinates. The results of the conversion show small biases between them less than a few meters that affect ZWD less than 1 mm and then PWV approximately less than 0.15 mm.

On the other hand, GSI's GPS array is divided into three types, as shown in Fig. 3.1a, according to sequence of installation time. They are (1) $Trimble^{TM}$ 4000 SSE of 107 sites (indicated by solid triangles), (2) $TOPCON^{TM}$ GP-R1DY which is equivalent with $Ashtech^{TM}$ Z-XII of 87 sites (indicated by solid circles), and (3) $Trimble^{TM}$ 4000 SSI of 362 sites (indicated by crosses). The receivers employed in (1) are distributed mainly in Kanto and Tokai districts of the main island of Japan, and the receivers employed in both (2) and (3) are distributed nationwide except Kanto and Tokai districts. In GSI's strategy for routine GPS analysis, (1) and (3) are regarded as identical, so that the GPS array is basically considered to be divided into Trimble cluster of 510 sites and Ashtech cluster of 100 sites. As will be mentioned in the next section, GSI employs clustering analysis strategy. Especially, in Trimble cluster having a large number of sites, back-bone (BB) sites indicated by solid stars in Fig. 3.1a are introduced to improve ZTD estimation as mentioned below.

Outline of the Routine Analysis

GSI's array used in this analysis observes dual-frequency phases at interval of 30 second transmitted from all GPS satellites above 15 degrees for 24 hours everyday. After the data are transmitted to GSI through public telephone lines, they are analyzed routinely with Bernese GPS Software (hereafter, BERNESE) [see *Rothacher and Mervart*, 1996, for details] by using the precise final satellite orbit information provided from International GPS Service for Geodynamics (IGS) (see *http://igscb.jpl.nasa.gov/* for details)

In the analysis, three-hourly ZTD are estimated deterministically at each site together with both coordinate parameters and initial phase ambiguities by least square method, where the temporal resolution of three hours in ZTD estimation is adapted to improve accuracy of coordinate estimations for the purpose of monitoring crustal deformation (see *Ohtani and Naito*, 1988, for details).

All the GPS data in GSI's array are not analyzed simultaneously. This is partly because

(1) the analyses including mixed receiver and/or antenna type may induce systematic errors in ZTD, and partly because (2) the volume of GPS data is too huge for quick analysis. Thus, GSI divides 610 sites into clusters composed of approximately 100 sites. They are first divided into Trimble cluster and Ashtech cluster, where Ashtech cluster of 100 sites are analyzed simultaneously, but Trimble cluster of 510 sites are again divided into five regional clusters with apertures about a few hundred km [see *Miyazaki et al.*, 1997, for details].

In general, it has been warned that ZTD obtained from a network with apertures smaller than 500 km has a common unknown bias in the network at each epoch, which is caused by incomplete separation of correlated ZTD estimations due to almost identical elevation angles of a GPS satellite observed at sites in analysis network [*e.g.*, *Bevis et al.*, 1992; *Rocken et al.*, 1993]. A simulation study by *Rocken et al.* [1993], for example, have shown that GPS can acquire absolute PWV with accuracy of 2 mm, incorporating baselines much longer than 500 km. *Duan et al.* [1996] have actually succeeded in obtaining absolute PWV with accuracy of about 1.5 mm by introducing long baseline of a few thousand kilometers in GPS/STORM network with apertures about several hundred kilometers.

Since the five regional clusters in the large Trimble cluster as shown in Fig. 3.1a have aperture of about 100 km, GSI's analysis introduces the back-bone (BB) clusters organized with fifteen BB sites distributed nationwide in the Trimble cluster, by which the aperture of the cluster reaches about 1000 km. At each BB site, five GPS analyses are done for the five regional clusters, so that five ZTD are estimated at each BB site. The PWV accuracy in the GPS clustering analyses is discussed in Section 3.1.8 in detail by using those five ZTD.

3.1.4 Data Sets Used in This Analysis

ZTD in SINEX Data of GSI

This study uses SINEX data of the daily solutions in GSI's routine GPS analysis of the array from 9(LST) of Sep.1 to 9(LST) of Sep.3, 1996, during which a front accompanied by heavy rainfalls passed over Japan, as mentioned in detail in the next section. In GSI, three-hourly ZTD at each GPS site is usually filed with SINEX format, but five three-hourly ZTD are filed at the BB sites in Trimble cluster. It should be noticed, however, that each ZTD is recorded as residual ZTD value from its a priori value. Since a priori ZTD is calculated based on Saastamoinen model with the mapping function of inverse sine of elevation angle by using a standard model of atmosphere, in which surface pressure, temperature, humidity at sea level are assumed to be 1013.25 hPa, 18° Celsius, and 50 %, respectively, it depends only on height of GPS site [*Rothacher and Mervart*, 1996]. As a result, in GPS analysis, it is generally given only as an initial value to statistically estimate a final absolute ZTD.

In consequence, this kind of analysis needs the absolute ZTD as sum of residual ZTD and a priori ZTD at each GPS site, where a priori ZTD is easily obtained from an atmospheric parameter file created by *GPSEST* of BERNESE in which correction of a priori ZTD to height above sea level is made. Computation processes to obtain PWV from ZTD will be described in Section 3.1.6.

Weather and Meteorological Data

This study chooses weather samples when a front accompanied by heavy rainfalls slowly moved eastward across the Japanese Islands in end of summer. Fig. 3.3 shows the weather maps at every 9(LST) from Sep.1 to Sep.3 of 1996 provided from JMA. During the three days, the front moved eastward across the Japanese Islands under an influence of a typhoon in the North-East Pacific Ocean moving north-eastward slowly.

Fig. 3.4 shows a distribution of integrated precipitation for six hours from 6(LST) to 12(LST) and from 18(LST) to 24(LST) during Sep.1 - Sep.3. They are based on one-hour integrated precipitation data observed by Automated Meteorological Data Acquisition System (AMeDAS) of JMA, a nationwide surface meteorological observation network for monitoring precipitation, temperature, wind, and sunshine. As the figure shows, the precipitation are observed in most part of Japan, especially with heavy rainfall amounting to about 80 mm in the coastal regions of the Sea of Japan during 18 - 24 (LST) of Sep.1.

To obtain PWV from ZTD, this analysis uses the Japan area objective analysis data for the NWP system in JMA, where the system is based on a three-dimensional optimum interpolation method and performed twelve-hourly by using JMA's regional spectral model [*JMA*, 1997]. Its computational domain has a mesh size of 257×217 corresponding to a grid spacing of 20 km in horizontal and 37 levels up to 10hPa in vertical. The analysis variables are surface pressure, geopotential height, two dimensional-wind velocity, temperature, and relative humidity.

It should be noted here that the model topography employed in the NWP system is different from the real topography. Fig. 3.1b shows the model's topographic height converted to GPS sites. Model's topography is smoother than the real topographic height of GPS sites shown in Fig. 3.1a can be seen. Fig. 3.1c shows the real topographic height minus the model's topographic height, and Fig. 3.2 shows its histogram. Average difference between the two topographic heights is about -203 m, indicating that the GPS sites are mostly located at lower heights than those in the model. This reflects the restrictions in installation of GPS monuments of GSI as mentioned in Section 3.1.3. There are huge differences in height amounting to several hundred to one thousand meters in mountain areas of the main island.

For computation of GPS PWV, surface pressure P_s and Tm in Π (see Appendix B.2) at GPS site are interpolated from these objective analysis data, where P_s is corrected to the real height at GPS site by assuming lapse rate of the temperature to be $5^o K/km$. T_m (and then Π) at GPS site is calculated from the NWP data by integrating from surface of the model's topography to top of the pressure level. Therefore, the difference between the model's topographic height and the real topographic height is not taken into account for calculating Tm and PWV. Thus obtained Π, however, has negligible effect on the estimation of GPS PWV. In case of height difference of 1000 m, for example, Π affect about 1 mm even when the front with a large amount of PWV overlies the islands. Meteorological PWV at all the GPS sites to be compared with GPS PWV are also calculated in the same way from the NWP data.

3.1.5 Distributions of Mean ZTD, ZHD, ZWD and PWV

Fig. 3.5a shows an averaged pattern of three-hourly ZTD during the analysis period of 9(LST) Sep. 1 - 9(LST) Sep. 3. The distribution pattern of ZTD is similar to that of the real topographic height shown in Fig. 3.1a, indicating that a major part of ZTD is a reflection of ZHD as will be shown in Fig. 3.5c. Fig. 3.5b shows the same pattern of ZTD as in Fig. 3.5a but obtained by averaging for two months from Aug. 1 to Sep. 30. The two patterns are almost same except for their north-south gradients. Namely, ZTD in Fig. 3.5a in the northern part of Japan shows a little larger value than that in Fig. 3.5b showing a typical pattern in summer. This seems to be a reflection of the front accompanied by heavy rainfalls in this area as mentioned above.

Fig. 3.5c shows averaged pattern of ZHD during the analysis period. It ranges from about 2.0 m in mountain areas to about 2.3 m in coastal plane areas. This reflects dependency of ZHD mainly on height above sea level. During the front passage, since gradient in atmospheric pressure was a few hPa over Japan as shown in Fig. 3.3, a major pattern in ZHD comes only from the real topographic height on which GPS sites are located.

Fig. 3.5d shows averaged pattern of ZWD during the analysis period obtained by subtracting ZHD of Fig. 3.5c from ZTD of Fig. 3.5a. It ranges 0.1 m to 0.3 m nationwide, and large ZWD can be seen in the north-eastern part of Japan. Fig. 3.5e shows averaged pattern of PWV converted from ZWD by multiplying Π. It ranges 20 mm to 50 mm corresponding to the range in the ZWD. In Fig. 3.5d and Fig. 3.5e, though a spatial pattern depending on topography can be seen, another pattern reflecting large precipitation pattern as shown in Fig. 3.4 can also be seen in the northern part of Japan.

It should also be noted here how much Π due to difference in temperature between the southern and northern parts of Japan affects PWV. During the analysis period, Π in average ranged from 0.155 in northern Japan to 0.166 in southern Japan, that induces difference in PWV less than about 3 mm. Except for these small effects, therefore, the PWV pattern of Fig. 3.5e is considered to be as same as that of the ZWD of Fig. 3.5d.

3.1.6 Temporal Anomalies of GPS PWV

Fig. 3.6 shows behavior in temporal anomalies of PWV calculated by subtracting the averaged PWV pattern shown in Fig. 3.5e from the three-hourly PWV at each GPS site during the analysis period, where surface pressure and Π calculated from the twelve-hourly NWP data are used for obtaining ZHD and PWV.

In the figure, a dense PWV belt moving across over the central mountains in the main island is clearly seen. It is partly similar to a precipitation belt seen in Fig. 3.4. Noteworthy is a fact that the intensity of the PWV belt does not seem to significantly decrease during the period of the front passage beyond the central mountains, in spite of that the heavy rainfalls were observed before its moving across over the mountains. After the front passed away from the Japanese Islands, however, PWV decrease rapidly in the western and north-eastern parts of Japan. This seems an effect of dry atmosphere moved behind the front from the north-eastern Asian Continent.

On the other hand, local variations on space scale of several ten kilometers are also seen in the figure, especially in mountain areas higher than several hundred meters above sea level (see Fig. 3.1). This implies not only a geographically constrained feature of water vapor itself but also the dense GPS array itself with space resolution of about 50 km in this analysis. One can easily imagine that adjacent two GPS sites often can have different PWV each others due to a large difference in height of the sites in mountain areas. In any case, GPS observations seem to acquire regional circulation of water vapor trapped in valleys in mountain areas.

In consequence, the PWV behavior reveal that GSI's GPS array can work as an all weather giant array sensor of PWV over the islands, though an internal error less than about 3 mm is included in PWV as will be discussed in Section 3.1.9.

3.1.7 Comparisons of GPS PWV with NWP PWV

In this section, the GPS retrieved PWV is compared with the calculated PWV from the objective analysis data of the NWP (hereafter we call these NWP PWV). Fig. 3.7a shows twelve-hourly GPS PWV from 9(LST) of Sep. 1 to 9(LST) of Sep. 3, where averaged GPS ZTD of the two estimates before and after 9(LST) and 21(LST) are converted into PWV by using twelve-hourly data of atmospheric surface pressure and II obtained from the objective analysis data for NWP in JMA. Fig. 3.7b, on the other hand, shows twelve-hourly NWP PWV calculated from the objective analysis data themselves. It should be noticed here that NWP PWV are the values at every 9(LST) and 21(LST), while GPS PWV are the averaged values of the two estimates for three hours before and after every 9(LST) and 21(LST). Thus, the obtained two data sets of PWV are a little inconsistent with each other.

Both figures show that there is a large difference in space resolution between the two data sets of PWV; *e.g.*, NWP PWV show a little smoother distribution than those of NWP PWV. The largest discrepancy between them appears in the high mountain area of the main island (see Fig. 3.1a), where GPS PWV always have positive biases with respect to NWP PWV. This bias is a reflection of the GPS sites mostly located in valleys in this region as mentioned in Section 3.1.3.

This feature is obvious in the differences between the two data sets of PWV in Fig. 3.7c, namely GPS PWV in Fig. 3.7a minus NWP PWV in Fig. 3.7b. Note, however, that it disappears after the front passed eastward away from Japan as seen in the figure of 9(LST) of Sept. 3 of Fig. 3.3c, suggesting that large positive biases in GPS PWV with respect to NWP PWV in mountain areas appeared especially when the large PWV belt overlay in this area. This provides an entirely new information for improving a regional system in NWP.

Fig. 3.8 shows residual distributions of GPS PWV minus NWP PWV in Fig. 3.7c. Noteworthy is a fact that negative biases can be seen through all the five figures in Fig. 3.8, implying that GPS PWV has a negative bias nationwide with respect to NWP PWV which is contrary to the above mentioned positive biases seen in mountain areas.

Fig. 3.9 shows relationships between GPS PWV minus NWP PWV and the real topographic height minus the model's topographic height. The regression line obtained by a least-square fitting indicates a dependency of PWV on the GPS site's height of 1.4 mm/100 m, which is considered to correspond to a possible water vapor mixing ratio in lower troposphere. Noteworthy is a fact that the above mentioned negative biases in GPS PWV are clearly shown by the regression line. This means that the negative biases appear even in regions of no difference between the real and modeled topographic heights such as Kanto

	Bias (mm)	Gradient*	RMS dev (mm)
09LST / Sep. 1	-2.0 ± 0.25	-1.3 ± 0.09	4.2
21LST	-4.3 ± 0.22	-2.0 ± 0.08	3.7
09LST / Sep. 2	-1.6 ± 0.23	-1.6 ± 0.08	3.9
21LST	-4.1 ± 0.23	-1.3 ± 0.08	3.9
09LST / Sep. 3	-4.0 ± 0.18	-1.0 ± 0.08	3.0
ALL data	**-3.2 ± 0.11**	**-1.4 ± 0.04**	**4.0**

Table 3.1: Biases and gradients of regression line between GPS precipitable water vapor (PWV) minus Numerical Weather Prediction (NWP) PWV and GPS site's topographic height minus NWP model's topographic height fitted by least-square method from 9(LST), Sep. 1 to 9(LST), Sep. 3, where rms deviations show around the regression line (also see Fig. 3.9). * Gradient = PWV/ Height (mm/ 100m)

plain, the largest plain in Japan. The histogram inside the Fig. 3.9 shows still a large rms difference of 4.0 mm with respect to the regression line, reflecting that GSI's array really can detect local behavior of water vapor never modeled in the NWP system of JMA.

Table 3.1 shows the biases and gradients of regression lines determined every twelve hours in same way. Each bias always shows negative and ranges from -1.6 mm to -4.3 mm. *Ohtani and Naito* [1998] also pointed out an existence of the same negative biases in GPS PWV with respect to those obtained from radiosonde observations especially in summer. Sources of these negative biases are not clear at present. The gradient, on the other side, reaches maximum value of -2.0 mm/100 m at 21(LST) of Sep. 1 when the front overlays the main island, and decreases to -1.0 mm/100 m after it passes away from the main island, suggesting that the above mentioned discrepancy in PWV due to difference in topography depends upon the amount of PWV itself.

3.1.8 Effects of the Clustering Analysis on PWV

As is mentioned in Section 3.1.3, since it is considered in general that ZTD from a network with apertures smaller than 500 km contain unknown biases, the nationwide Trimble cluster, for example, in GSI's analysis is divided into five regional clusters with apertures of approximately a few hundred km, and ZTD in each regional cluster are estimated with fifteen back bone (BB) sites distributed nationwide. Little systematic biases on spatial scale of the regional clusters, however, can be significantly seen in the figures shown above (see from Fig. 3.5 to Fig. 3.7).

Therefore, to discuss effects of the clustering analysis upon the estimated GPS PWV,

PWV obtained in Trimble cluster, the largest cluster in the array, are intensively investigated here. As a result, a surprising fact is found that rms difference of estimated PWV at all the fifteen BB sites is less than 1 mm during the analysis period. Fig. 3.10, for example, shows PWV's variation at three BB sites of A, B, and C in northern, central and southern parts of Japan, respectively, shown in Fig. 3.1a, where the five PWV corresponding to the five regional clusters are estimated. It is obvious in the figure that differences in PWV reach maximums of about 3 mm at all the BB sites during the front passage. These facts suggest that difference in PWV between the clusters with different receivers such as Trimble and Ashtech is also very small.

3.1.9 Summary

Progresses in accuracy of satellite's orbit as well as in analysis software of GPS relative positioning have made it possible to precisely determine precipitable water vapor (PWV) above the ground. Namely, the PWV can be obtained from zenith wet delay (ZWD) multiplied by a constant Π, where ZWD is GPS retrieved zenith tropospheric delay (ZTD) minus zenith hydrostatic delay (ZHD) calculated from atmospheric surface pressure at GPS site.

To monitor crustal deformation, Geographical Survey Institute (GSI) of Japan has deployed the nationwide GPS array amounting to 610 sites in 1996, which corresponds to the spatial resolution approximately of about 50 km. The PWV converted from the three-hourly ZTD retrieved in the array by using BERNESE software has shown good agreements with those from radiosonde observations over Japan [see *Ohtani and Naito*, 1998].

In this study, to farther evaluate the PWV in the GPS array of GSI for application to numerical weather prediction (NWP), GPS PWV obtained at 556 sites are visualized all over the Japanese Islands from 9(LST), Sep.1 to 9(LST), Sep. 3 when a front accompanied by heavy rainfalls moved slowly eastward over the Japanese Islands, where the used atmospheric pressure and Π are based upon the Japan area objective analysis data for NWP in Japan meteorological Agency (JMA).

Thus obtained GPS PWV have shown high space resolution behavior in PWV trapped in valleys in mountain areas, for example. Their temporal anomalies from their averages have clearly shown a dense PWV belt moving along with the front eastward across over the central mountains in the mainland of Japan. This feature reveals that GSI's array has ability as an all weather giant array sensor of PWV over Japan.

Comparisons of GPS PWV with PWV calculated from the objective analysis data for the NWP have shown that GPS PWV have positive biases with respect to NWP PWV amounting to 10 mm, reflecting that the GPS sites of the array are almost located in valleys in mountain areas and that their heights above sea level are almost lower than those on the model's topographic height employed in the NWP. However, GPS PWV have still shown a negative bias of 2 - 4 mm with respect to NWP PWV all over Japan not due to difference in the topographies.

Effects of the clustering GPS analysis employed in GSI's array upon the GPS PWV are found to be less than 1 mm on average and to reach maximum value of about 3 mm during the front passage, indicating that the clustering analysis employed in GSI's routine monitoring of crustal deformation also can work as a monitoring system of PWV over Japan.

All these facts above reveal that the GPS PWV acquired by GSI's GPS array are applicable to the regional NWP system in JMA for improving rainfall forecast. There remains a challenging issue of real time GPS analysis of the giant array.

3.2 A Close Relationship between Temporal Anomalies in Site Coordinates and Zenith Tropospheric Delay in GPS array over the Japanese Islands in Summer

3.2.1 Abstract

A close relationship between horizontal coordinate variation and zenith tropospheric delay (ZTD) in Global Positioning System (GPS) analyses is found in the solution of operational analysis data of the nationwide GPS array of Geographical Survey Institute (GSI), where azimuthally homogeneous distribution of water vapor is assumed in the analysis. A linear relationship between horizontal coordinate and ZTD gradient can be seen clearly, in particular, during weather conditions that systematic horizontal gradient of water vapor exists in cases of front passages and tropical cyclone passage. The ZTD gradient of 50 mm per horizontal distance of 100 km is found to cause apparent horizontal coordinate variation of about 10 mm. These relationships become useful information to diagnose if unusually large horizontal coordinate variations retrieved by the GPS analysis reflect net crustal movement or noise caused by horizontally inhomogeneous distribution of water vapor.

3.2.2 Introduction

It is known that daily Global Positioning System (GPS) coordinate solutions for the purpose of monitoring crustal movement generally show unusual variations of cm order on time-scale of several days. The major source for the variations is the delay of arrival time of GPS transmitted microwave through troposphere called tropospheric delay though the coordinate solutions are estimated simultaneously with zenith tropospheric delay (ZTD) by least square method under the assumption of no correlation between them.

ZTD is composed of two contributions; one is zenith hydrostatic delay (ZHD) of about 2.0 m to 2.4 m, which depends on surface atmospheric pressure at the GPS sites, and another is zenith wet delay (ZWD) of $\sim$ 0.6 m, which depends on the integrated water vapor in the zenith direction. In general, the former and the latter changes with synoptic and local scale, respectively, which correspond to several days and several ten minutes time-scale. In addition, the magnitude of the variations in ZHD is generally 0.01m order while ZWD is 0.1m order. Thus, the apparent variations of the coordinate solution are considered to reflect misestimation of ZWD.

Those apparent coordinate variations are serious noise for monitoring crustal movement of mm order associated with the occurrence of earthquakes. Thus, it is necessary to diagnose if such variations of coordinate reflect net crustal movement or noises caused by water vapor distributions.

In general, precision of vertical components in GPS analyses is worse than that of horizontal components mainly because the direction of the component is same with ZTD. Accordingly, misestimation of ZTD sometimes causes unusual variations reaching about 10 cm in vertical coordinate solution. Another main reason is that satellite configuration is limited in GPS analysis; GPS satellites having elevation angle of more than 15 degree are generally used [*e.g.*, *Heki*, 1990]. A preliminary study on the relationship between the ZTD and the vertical component by *Chida et al.* [1999] have shown some relationships beteen them. It is necessary to advance the study with long data if the relationships are universal or occasional.

On the other hand, ZTD gradients induce apparent variations of horizontal coordinate when azimuthally inhomogeneous distributions of water vapor are not considered in GPS analysis as shown in Fig. 3.11. For example, *Heki et al.* [1997] have detected a slow earthquake related to Sanriku-Haruka-Oki earthquake based on GPS data in the northern Japan observed in the nationwide GPS array of Geographical Survey Institute (GSI). In the time-series of coordinates for about one year, horizontal coordinate variations of about 2-3 cm in east-west component and about 5 cm in the north-south component, having periods of several days, can be seen especially in summer season. One of the major sources of such unusual variations are considered to be distributions of water vapor along with fronts as shown in Section 3.1 and *Iwabuchi et al.* [1998], because stationary fronts extending from east and west directions over the northern Japan are confirmed frequently in weather maps during the period. If the 'apparent' variations can be explained by water vapor distributions and then removed, it must be possible to predict earthquakes based on GPS detected signals of minute crustal movement.

Such horizontal coordinate variations are also shown in daily solutions of GSI's routine analysis for the GPS array where a simple mapping function $1/\sin(\theta)$ (see Appendix B.2), indicating no consideration of azimuthally inhomogeneous distributions of water vapor, is applied in the GPS analysis of the array. It may be explained by horizontal gradient of ZTD since the GSI's analysis system assumes the azimuthally homogeneous distributions of water vapor. Thus, main purpose of the study is to clarify relationships between the GPS horizontal coordinate solution and the horizontal gradient of water vapor distributions. The relationships are investigated in the cases of the severe weather conditions such as front passages shown in Section 3.1 in which systematic horizontal gradients of ZTD exist over the Japanese Islands.

3.2.3 Data and Computation

This study uses Software-INdependent EXchange Format (SINEX) data of GSI (see Section 3.1.4 for detail) in 1996. Solutions of daily coordinate in international terrestrial reference frame (ITRF) and three-hourly ZTD in each site are estimated by least square method simultaneously with initial phase ambiguity in Bernese GPS Software [*Rothacher and Mervart*, 1996] (see Appendix B.1), and the results are filed in the SINEX data everyday.

We select three cases that systematic horizontal gradients of water vapor distribution exist over the Japanese Island (see weather maps at 9 (LST) in Fig. 3.12); fronts extending east and west at July 17, 1996 and north and south at Sep. 1, 1996 (same case with Section 3.1), and stationary tropical cyclone in central Japan at Jul. 20, 1996.

The daily average of eight 3-hourly ZTD is calculated to compare the ZTD with coordinate solution in same time-resolution. Then daily anomalies from the averaged ZTD for two weeks including the three cases shown in Fig. 3.12, (A) Jul. 16 to Jul. 29, 1996 and (B) Aug. 28 to Sep. 11, 1996 (hereafter, we refer the two periods as periods A and B), are calculated in each sites. We can consider that the variation of ZWD can be shown in the ZTD anomalies because the averaged ZTD includes systematic biases in each station caused by ZHD which depends on topography and the specific feature of GPS antennas and receivers. For example, it is confirmed that little differences in variation are seen between ZTD and the converted PWV from ZWD in the case of the front passage shown in Fig. 3.6. These facts support that most of variations in ZTD reflect those in ZWD. The daily horizontal coordinate anomalies in each station are calculated in a similar way to calculate the ZTD anomalies. The daily anomalies of horizontal coordinate vectors are shown by fixing a GPS site showing relatively small ZTD gradients.

3.2.4 Results

Figs. 3.13a,b,c show anomalies of horizontal coordinate vectors on contour maps of ZTD anomalies in the three cases of (a) Jul. 17, 1996, (b) Jul. 20, 1996, and (c) Sep. 1, 1996, where reference points of coordinate are (a) Tsukuba , (b) Sinjyo, and (c) Shigaraki, respectively. The vectors intersect the contour of ZTD anomalies and point the region where ZTD anomaly is relatively small, namely the vectors point to relatively dry regions. The magnitudes of the vectors are in inversely proportional to the contour interval showing the magnitude of the ZTD gradient.

Fig. 3.14 shows averaged ZTD anomalies, these gradients, and the averaged horizontal coordinate anomalies every 25 km from a line AB showing the maximum value of ZTD in Fig. 3.13a, where we assume that isogram of the ZTD gradients in Fig. 3.13a is approximately parallel to AB within the distance of 200 km from AB. The figure shows linear relationship between the gradient of ZTD anomalies and the horizontal coordinate anomalies in regional scale. It also supports that the unusual variations of horizontal coordinate frequently shown in GSI's GPS array is mainly due to systematic spatial gradient of water vapor distribution caused by meteorological events as shown in Fig. 3.11.

3.2.5 Discussions

In the above section, the existence of a linear relationship between the gradient of ZTD anomaly and the horizontal coordinate anomaly in the cases of the front passages and the tropical cyclone is suggested. Figs. 3.15a,b,c (corresponding to Figs. 3.13a,b,c) are correlation diagrams showing relationship between the coordinate anomalies and gradients of ZTD anomaly in north-south and east-west directions by using whole GPS sites, where Tsukuba is fixed as a reference point. The gradients of ZTD anomalies in each GPS site are computed by polynomial interpolation with GMT (Generic Mapping Tool Ver. 3.0; *Wessel and Smith*, 1991) software. Those involve some biases especially in coastal region corresponding to data boundaries. Note that biases in linear regressions in the correlation diagrams in Fig. 3.15 have no physical meanings between the ZTD gradients and the horizontal coordinate anomalies because the biases vary with reference sites, which corresponds to the translation of axis x in the correlation diagrams. Thus, we discuss only the gradients of the figure below.

In Fig. 3.15, when the east-west front stays over the Japanese Islands (Fig. 3.12a) , some correlation can be seen in north-south component while no correlation in east-west component. On the other hand, in the case of the north-south front (Fig. 3.12c), some correlation is identified in both components though it is not so significant as (a). This is considered to reflect that the front extends northeast-southwest rather than north-south. The case of tropical cyclone (Fig. 3.12c) also shows some correlation.

Table 3.2 shows correlation coefficient ρ between the gradients of ZTD anomalies and the coordinate anomalies of north-south and east-west components, respectively, and coefficient C in the equation

$$\Delta COD_{ns,ew} = C \times \frac{\partial ZTD}{\partial D_{ns,ew}} \tag{6}$$

which expresses linear relationship between the gradients of ZTD anomalies and the coordinate anomalies as suggested in Figs. 3.13a and 3.15. In Eq. (6), COD shows variations of north-south and east-west coordinate (mm), D shows horizontal distance (km), suffixes ns and ew show north-south and east-west directions, respectively (see Fig. 3.11). The stronger correlation can be seen when fronts or the tropical cyclone stay over the Japanese Islands. Moreover, the north-south component shows stronger correlation than the east-west component throughout the two periods. One reason is considered as the difference of typical time-scale of water vapor variations in the two directions, that is synoptic weather conditions change mainly from west to east over the Japanese Islands due to the effect of the prevailing westerlies. We can expect that correlation between the gradients of ZTD anomalies and the coordinate anomalies become strong if we use ZTD and coordinate data with high temporal resolution which can follow water vapor variations. Other reasons are considered as the systematic biases such as difference of absolute water vapor distribution in north-south direction due to climatological north-south gradient of averaged temperature, or effects of satellite configuration showing blank region in the north direction.

The strongest correlation through the two periods can be seen in north-south component at Jul. 17 when the front extending east and west stays over the Japanese Islands as shown in Fig. 3.12a. A magnitude of C at that time is about 0.19×10^5. Assuming the linear relationship between gradients of ZTD anomalies and the horizontal coordinate anomalies, we can predict apparent variation in horizontal coordinate caused by the ZTD gradient based on Eq. (6). In the case (a), the apparent horizontal coordinate variation of about 10 mm is induced by the ZTD difference of 50 mm per horizontal distance of 100 km. Considering that the ZTD difference of 100 mm per 100 km distance can be seen at the maximum in Fig. 3.15a, we can expect that apparent horizontal coordinate variation of about 40 mm arises when a site with maximum ZTD gradient is used as reference site. These results show that it is possible to diagnose if the unusual horizontal coordinate variations are caused by net crustal movement or noises induced by horizontally inhomogeneous distributions of water vapor without meteorological data when the simple mapping function $1/\sin(\theta)$ is applied in the GPS analysis.

On the other hand, in calm weather conditions, Table 3.2 and Fig. 3.15 suggest that gradients of ZTD anomalies and horizontal coordinate anomalies do not show strong correlation. For example, the east-west component of Jul. 16 in (Fig. 3.12c) shows no correlation between gradients of ZTD anomalies and horizontal coordinate anomalies and therefore C can not be fixed. *MacMillan* [1995] has shown that an application of mapping function considering the ZTD gradient for VLBI observations improves repeatabilities of coordinate solutions.

(A) Date	N-S		E-W	
Jul., 1996	ρ	C	ρ	C
16	0.24	0.62	0.11	1.24
17	0.64	0.19	-0.02	-7.09
18	0.24	0.60	0.25	0.62
19	0.21	0.63	0.46	0.31
20	0.47	0.31	0.36	0.43
21	0.30	0.47	0.29	0.46
22	0.23	0.45	0.21	0.70
23	0.41	0.39	0.34	0.42
24	0.36	0.40	0.28	0.49
25	0.41	0.33	0.30	0.46
26	0.12	1.09	0.29	0.61
27	0.39	0.38	0.20	0.73
29	0.32	0.53	0.17	1.03

(B) Date	N-S		E-W	
Aug., 1996	ρ	C	ρ	C
28	0.24	0.56	0.26	0.42
29	0.32	0.38	0.22	0.55
30	0.42	0.37	0.22	0.71
31	0.35	0.55	0.32	0.84
Sep. 1	0.40	0.34	0.26	0.44
2	0.38	0.30	0.29	0.36
3	0.51	0.24	0.23	0.43
4	0.39	0.44	0.10	0.98
5	0.53	0.24	-0.02	-9.35
6	0.50	0.22	0.05	1.88
7	0.40	0.34	0.10	0.92
8	0.43	0.36	0.12	1.12
9	0.35	0.45	0.07	2.76
10	0.34	0.41	0.23	0.45

Table 3.2: Correlation coefficient ρ between horizontal coordinate variation and ZTD gradient, and proportional coefficient C throughout the two periods with GSI's GPS sites of 612.

Bar-Sever [1998] has also shown improvements of precision, accuracy, and repeatability in coordinate solution of GPS analysis with estimation of the ZTD gradient. Therefore, it is expected that most of the apparent horizontal variations of coordinate in severe weather conditions disappear if the ZTD gradients are estimated in GPS analysis. However, in the calm weather conditions, it may be unnecessary to estimate ZTD gradients due to relatively large random error as shown in Table 3.2. Thus, estimation of the ZTD gradients require temporal resolution which suits the time-scale of water vapor variations.

The coefficient C in Eq. (6) is related to scale height of water vapor [*MacMillan*, 1995; *Heki*, 1999]. Table 3.2 shows that C is relatively small during front passages as compared with calm weather conditions. In addition, the feature of water vapor distributed near the surface is shown incase of the front passage in Section 3.1,. Thus, difference of C may reflect the difference in structure of vertical distributions of water vapor in each weather condition.

Miyazaki et al. (1999) have investigated the apparent horizontal coordinate variations shown in this study by re-analyzing GSI's GPS data with mapping function considering the ZTD gradient, and have shown that most of the apparent horizontal coordinate variations shown in Fig. 3.13 disappeared. However, horizontal coordinate variations of a few cm remain after removing the apparent coordinate changes caused by the ZTD gradients. It may reflect the net crustal movement, systematic biases due to satellite configuration suggested in *MacMillan* [1995], and variations of water vapor in a high frequency. Therefore, it is required to find out causes of the variations with further comprehensive studies.

3.2.6 Conclusion and Further Studies

A close relationship between GPS determined horizontal coordinate variation and the ZTD gradient is found. The relationship is useful to diagnose if unusual large horizontal coordinate variations reflect net crustal movement or azimuthally inhomogeneous distributions of water vapor. Comparison studies with mapping functions including ZTD gradient are needed to verify effectiveness in its application under the various weather conditions.

Studies on relationships between ZTD and vertical coordinate variation are also required to find methods for diagnosing if unusual large vertical variations estimated in GPS analysis are caused by real crustal movement concerned with occurrence of the earthquakes or not since the vertical movement is also important for the Japanese Islands locating near subduction zone of plate boundaries.

3.3 Diurnal Variation of Precipitable Water Vapor Retrieved by GPS Array over the Japanese Islands in Summer

3.3.1 Abstract

Behavior of the summer diurnal variation of water vapor over the Japanese Islands is visualized based on three-hourly zenith tropospheric delay (ZTD) data routinely retrieved from the nationwide Global Positioning System (GPS) array in Geographical Survey Institute (GSI). Composites of the ZTD data show characteristic spatio-temporal variations of water vapor closely related to topography of the Japanese Islands. The variations are considered to be caused by thermally excited local circulation. In principal component analysis (PCA) of the composite ZTD, the first dominant empirical orthogonal function (EOF)s in July and August whose contribution rates are 67.1% and 58.7%, respectively, show time coefficients having sudden increase from dawn till dusk and gentle decrease from evening to night. The temporal variations can be seen over the Japanese Islands except for the region which surrounds the central mountainous are of Japan. The similar feature is also confirmed in precipitation caused by convergence of water vapor toward evening in mountainous area. These are consistent with results of model simulation on thermally induced local water vapor circulation.

3.3.2 Introduction

With the advent of Global Position System (GPS), the application of GPS for water vapor sensor has been considered and tested [*e.g.*, *Bevis et al.*, 1992; *Businger et al.*, 1996]. The concept is to regard tropospheric delay of GPS carrier wave as a meteorological signal, while the delay is considered to be noise for the purpose of positioning and monitoring crustal movement.

The GPS observable of water vapor is included in zenith tropospheric delay (ZTD), where ZTD is composed of zenith hydrostatic delay (ZHD) which depends upon atmospheric pressure and zenith wet delay (ZWD) due to water vapor in the zenith direction. ZWD can be converted to precipitable water vapor (PWV), integrated water vapor in atmospheric column, by multiplying a constant of proportionality Π of about 0.15 (For further details, see Appendix B.2). The excellent ability of GPS as water vapor sensor has been confirmed in many studies showing that GPS retrieved PWV has almost the same accuracy as those from radiosonde and water vapor radiometer [*e.g.*, *Rocken et al.*, 1993; *Elgered et al.*, 1997].

In Japan, a dense nationwide GPS array which consists of 612 GPS sites in 1996 (see Fig. 3.1) has been deployed by Geographical Survey Institute (GSI) for the purpose of monitoring crustal deformations and constructing highly precise geodetic network [*Miyazaki et al.* 1997]. Results of routine analyses of the GSI's array operated by GSI with Bernese GPS Software [*Rothacher and Mervant*, 1996] are filed with Software INdependent EXchange (SINEX) format. The SINEX data contains three-hourly ZTD at each site as a byproduct with daily solution of coordinates, where the three-hourly estimation of ZTD is empirically applied while daily estimation of coordinates is applied to average errors or biases below diurnal time-scale such as GPS satellite configurations, thermal expansion of GPS monuments caused by solar radiation, and crustal deformations due to loading of the oceanic tide. PWV based on the SINEX data of GSI's GPS array has also shown good agreement with those from radiosonde observation over the Japanese Islands within 3 mm [*Ohtani and Naito*, 1998] and its spatial consistency has also confirmed by *Iwabuchi et al.* [1998] (see Section 3.1).

It is known that thermally induced local and mesoscale circulation such as the land- and sea- breeze and the valley wind prevail over the Japanese Islands especially in summer season when the westerlies over the Japanese Islands become weak. The land- and sea- breeze is caused by difference of heat capacity between land and ocean, and the valley wind is caused by difference of the absorption rate of the solar radiation between in mountainous regions and the basins. The converged water vapor in mountainous region by those diurnal circulation, for example, sometimes cause heat thunderstorm with severe rainfall and lightning especially in central Japan [Kuwagata, 1997].

Such diurnal variations of the water vapor have not been routinely predicted by numerical weather prediction (NWP) system in Japan Meteorological Agency (JMA). One of the reasons is that no instruments to observe the diurnal circulation of water vapor with high spatio-temporal resolution over the Japanese Islands exist at present. Thus, researches on mechanism and verification of the diurnal circulation of water vapor have relied on other meteorological data such as precipitation and wind data [*e.g.*, *Kuwagata*, 1997] or model approaches [*e.g.*, *Kimura and Kuwagata*, 1995] in place of the water vapor data.

We can expect that the GSI's GPS array can provide new information on the thermally induced local circulation with spatial resolution of about 50 km, corresponding to the spatial resolution of the array. The understandings of behavior of water vapor circulation are important not only for predicting heavy rainfall in NWP system but also for developing meso- and local- scale model. Thus, in this study, we first visualize the summer diurnal variations of composite PWV over the Japanese Islands based on ZTD retrieved from the

GSI's nationwide GPS array, and secondly we extract dominant spatio-temporal modes for the ZTD based on principal component analysis (PCA).

3.3.3 Data and Computation

We use SINEX data in the GSI's nationwide GPS array of 612 GPS sites (see Section 3.1.4 for detail) in 1996, which contains eight three-hourly ZTD simultaneously estimated with daily coordinate solutions in each site. One-hourly integrated precipitation data observed by Automated Meteorological Data Acquisition System (AMeDAS) of JMA in 1996 is also used to investigate relationship of diurnal variations between ZTD and precipitation. Surface pressure data at weather stations of JMA in 1996 is used to estimate the contribution of the diurnal variations in ZHD to those in ZTD.

Daily composites of three-hourly ZTD in each site are calculated every month from July to December, 1996 based on the SINEX data, and then, ZTD anomalies are calculated by subtracting averaged ZTD during one month in each site. Systematic bias during each month in each site such as characteristics of GPS receivers and antennas, conditions of sight of sky, and ZHD which depends on topography are considered to be removed by the subtraction. In addition, ZHD variations of several days-scale corresponding to surface pressure changes of less than several hPa in synoptic variations are also considered to be removed by calculating monthly composites of three-hourly ZTD. Hence, the ZTD anomalies approximately reflect diurnal variations of ZWD.

The composite ZTD anomalies are also used for PCA (principal component analysis) [*e.g. Preisendorfer*, 1988] to extract dominant features of diurnal variations of water vapor over the Japanese Islands, where PCA can extract dominant mode of spatial distribution pattern from original data by finding smaller number of linear combination of original variables that maximize the variance accounted for in the original data. The spatial pattern is called empirical orthogonal function (EOF) which is equal to an eigenvalue analysis of the covariance or correlation matrix. For further details, see Appendix C.

3.3.4 Results and Discussions

Visualized Diurnal Variation of Composite ZTD

Figs. 3.16 and 3.17 show composite maps of three-hourly diurnal variations of ZTD anomalies during one month of July and August, 1996, respectively. The diurnal variations of ZTD ranging up to about 30 mm, that is almost equal to those of PWV ranging up to about 5 mm, can be seen over the Japanese Islands. The figures show a common spatial pattern in mountainous area where the ZTD anomalies become maximum from evening to midnight. The phase of ZTD anomalies seem to depend on horizontal scale of mountainous area, that is, phase in low mountainous area lead to that of high mountainous area distributed in central Japan. The facts are qualitatively consistent with suggestion from two dimensional model simulation study on thermally induced water vapor circulation over the simple sinusoidal topography [*Kimura and Kuwagata*, 1995].

The diurnal variations of ZTD at several sites where the distance between GPS site and weather station is less than 10 km are also shown in Figs. 3.18, 3.19, 3.20, and 3.21 with those of ZHD. The amplitude of the temporal variation of ZTD is relatively large not only in mountainous area but also valley area surrounded by mountains. Note that the largest amplitude in the figs. is seen at Turugisan (mountain) station, the highest station (1371 m) in Shikoku Islands. Because the station is several ten km away form the Pacific Ocean and Seto-nai Kai, the Inland Sea of Japan, the largest amplitude is considered to be the reflection of the strong coupling of land- and sea- breeze and valley wind.

We have to consider that the composite ZTD anomalies in Figs. 3.16 and 3.17 contain small contributions of diurnal variation in ZHD as mentioned in Section 3.3.3. The diurnal variations of ZHD shown in from Fig. 3.18 to Fig. 3.21 show similar semidiurnal variations each other reaching maximum value at around 9 and 21 and ranging from 2 to 4 mm over the Japanese Islands. The ZHD variations are considered to be caused by diurnal and semidiurnal variations of the atmospheric tide caused by mainly inertial gravity wave in atmosphere excited by heating of the solar radiation, and partly caused by heat low, local-scale atmospheric depression which develops around the mountainous area induced by heating in spring and summer daytime. Considering that the heat low is regional phenomenon, large differences of the ZHD's diurnal variation between July and August at some sites are considered to reflect differences of magnitude in the heat low between the two months.

Figs. 3.22 and 3.23 show composite maps of three-hourly diurnal variations of ZHD anomalies during one month of July and August, 1996, respectively. The figures show that magnitude of the diurnal variation of ZHD is large in mountainous area. To compare the diurnal variation of ZHD of July with that of August, differences of magnitude between July and August can be seen during 3 to 9 and 12 to 18 especially in mountainous area of the central Japan. On the other hand, phase of the diurnal variation of ZHD does not show significant difference between July and August.

Consequently, we can consider that the diurnal variations in ZTD shown in Figs. 3.16 and 3.17 include ZHD contributions of less than 20%.

EOF mode	Jul.	Aug.	Sep.	Oct.	Nov.	Dec.
1	67.1	58.7	68.7	54.8	65.8	74.3
2	18.7	30.0	17.9	25.3	23.3	12.0
3	8.3	5.9	8.1	14.1	5.7	6.1
4	3.4	3.3	2.8	2.8	2.6	3.4
5	1.1	0.9	1.1	1.4	1.3	2.3
6	0.8	0.7	0.8	1.0	0.8	1.2

Table 3.3: Percentage (or proportion) of the total variance in ZTD composite for one month explained by each EOF mode.

Figs. 3.24 and 3.25 show composite maps of precipitation calculated in a similar way of the ZTD in Figs. 3.16 and 3.17. The maximum of precipitation observed in mountainous area from evening to midnight can be considered to correspond with convergence of water vapor shown in Figs. 3.16 and 3.17. However, there are some patterns that can not be explained by the convergence of water vapor especially in the southwestern Japan. These are considered to reflect effects of heavy rainfall caused by front- and typhoon- passages in each month.

According to *Oki and Musiake* [1994], rainfall pattern in central Japan belongs to a category which reaches its peak at evening time in summer. In addition, *Kuwagata* [1997] has shown dependencies of diurnal variation of summer precipitation on topography in central Japan. Thus, we also show the dependencies of precipitation on topography in Fig. 3.26, where AMeDAS stations are divided into three categories according to height of the stations; (a) less than 500m, (b) 500m to 1000m, (c) more than 1000m. Precipitation peak at evening in July and those both at morning and evening in August are remarkable at relatively high stations. This suggests that convergence of water vapor in mountainous area shown in Fig. 3.16 and 3.17 cause rainfall at the stations.

Dominant EOFs and their Time Coefficients

Common characteristics shown in the composite analyses of ZTD's diurnal variations can be extracted by PCA. Figs. from 3.27 to 3.32 show distribution maps of the first to third EOFs in composite ZTD and their time coefficients from July to December, 1996. The percentage (or proportion) of the total variance in composite ZTD anomalies explained by each EOF mode is shown in Table 3.3. In this study, we discuss till the third mode of EOF because forth and the larger modes of EOF can explain less than 5% of the total variance.

The distribution map of the first EOF (proportion = 67.6%) for composite ZTD in

July and its time coefficient in Fig. 3.27 show a temporal variation of sudden increase of ZTD from dawn till dusk and gentle decrease from evening to night is prominent over the Japanese Islands except Kanto plane and Kinki district displayed in gray color in the map, where these regions show negative value in the first EOF. Also, the similar pattern can be seen in distribution map of the first EOFs and their time coefficients from August to November (Figs. from 3.28 to 3.31). The pattern can not be seen in the distribution map of December EOF (Fig. 3.32). Thus, the temporal variations of the time coefficients from July to November that can explain more than 50% of the total variance of composite ZTD, are considered to reflect thermally induced water vapor circulation over the Japanese Islands.

The negative value of the first EOF in Kanto plane and Kinki district can be seen only the distribution maps in July and August (Figs. 3.27 and 3.28), while such negative value of the first EOF can not be seen from September to November. *Kimura and Kuwagata* [1995] have shown that phase of local circulation depends on spatial extent of sinusoidal topography. Considering that the Kinki district and Kanto plain are regions around 100 km-scale mountainous area in central Japan and that they face the ocean, the negative value of the first EOF in these regions from July to August may reflect diurnal variations caused by strong and complicated coupling of land- and sea- breeze and valley wind in summer season.

The distribution map of the second EOFs for composite ZTD from July to September shows a spatial pattern characterized by monopole centered in the central Japan. When we consider a reverse spatial distribution for the second EOF in July and therefore reverse time coefficient for the EOF, we can interpret the variation of the coefficients as thermally induced water vapor circulations prominent in the large mountainous area of central Japan. The temporal variations seem to be gentler than those for the first EOF from July to November and phase delay of about 3 to 6 hours for phases of the time coefficients of the first EOF can be seen. The phase delay in the relatively large mountain is consistent with result of *Kimura and Kuwagata*, [1995].

We have shown that the relatively large amplitudes of composite ZTD anomalies in July and August can be seen in small mountainous regions in the network. Thus, in summer, we can consider that the first EOF reflects large variations or variances of ZTD in relatively small-scale mountainous area, while the second EOF reflects small variations of ZTD in relatively large-scale mountainous area.

In the third EOFs and their coefficients in Figs. from 3.27 to 3.32, the time coefficients show distinctive semi-diurnal variations not only in summer but also in winter though proportions are relatively small (less than 10% except October). The peaks and troughs of the time coefficient occur roughly in phase with the diurnal variation of ZHD shown in Figs. from 3.18 to 3.21. However, we can not simply regard the EOFs as reflection of diurnal variation of ZHD because their distribution maps show complicated pattern every month.

3.3.5 Concluding Remarks

Large diurnal variations of water vapor over the Japanese Islands caused by thermally induced local circulation in summer are detected by the GSI's nationwide GPS array. The temporal variations show increase of water vapor during daytime and decrease during nighttime over the Japanese Islands except regions surrounded by relatively large mountains region in central Japan. The phase of the diurnal variations seems to be determined by spatial size of mountains as the study of model simulation on water vapor circulation has suggested. It is expected that GPS retrieved ZTD or PWV greatly contribute to development in mesoscale meteorology in future.

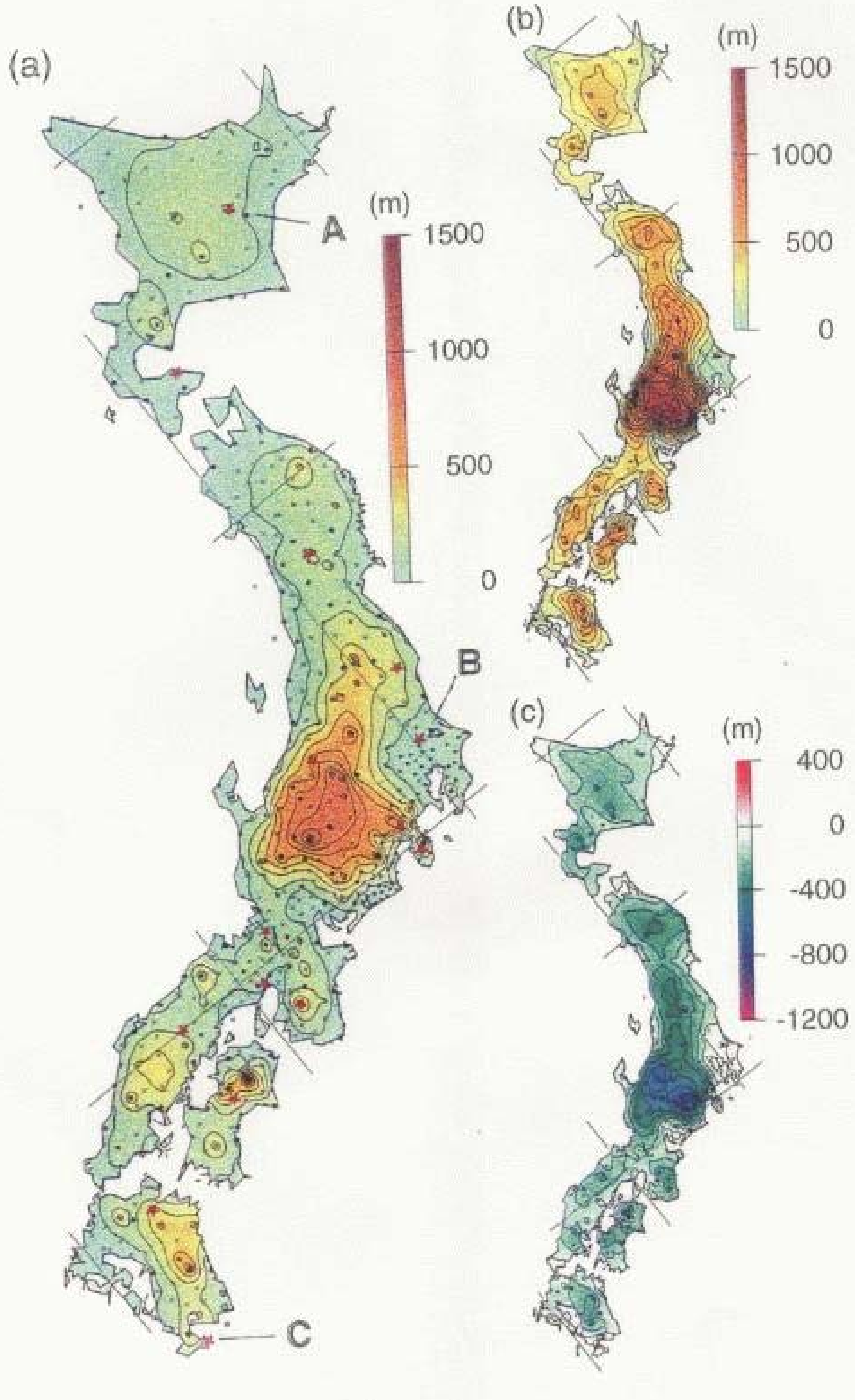

Figure 3.1: (a) Topographic height based on the 556 GPS sites of nationwide GPS array of Geographical Survey Institute (GSI) used in this study, the three types of array are shown; *Trimble*^{TM} 4000 SSE at 107 sites (solid triangle), *TOPCON*^{TM} GR-R1DY which is equivalent with *Ashtech*^{TM} Z-XII at 87 sites (solid circles), and *Trimble*^{TM} 4000 SSI at 263 sites (crosses). Red stars indicate the back-bone (BB) sites in Trimble cluster. (b) Topographic height at the 556 GPS sites converted from the model's topographic heights employed for the Japan area regional numerical weather prediction (NWP) system in JMA. (c) Difference between the two topographic heights, that is, (a) - (b). All contour intervals are 100 m.

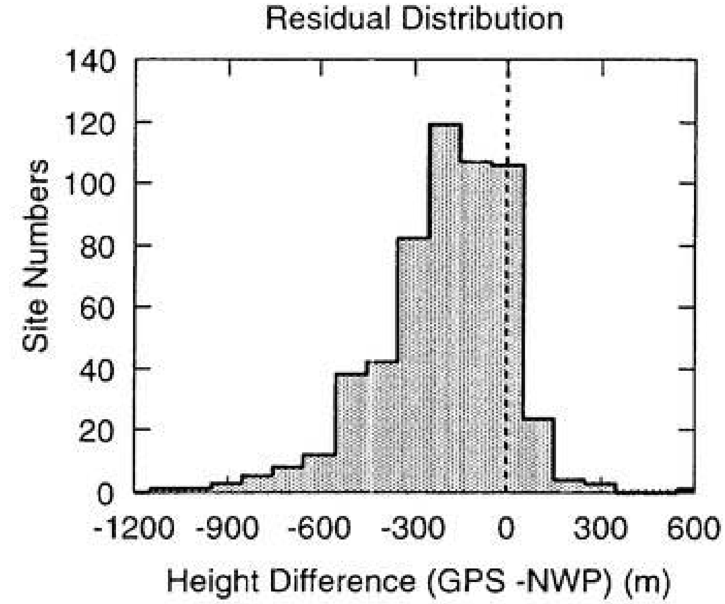

Figure 3.2: Residual distribution of Fig. 3.1c, where the average value is -203 m which indicates that GPS sites are almost located below the model's topographic height for the NWP.

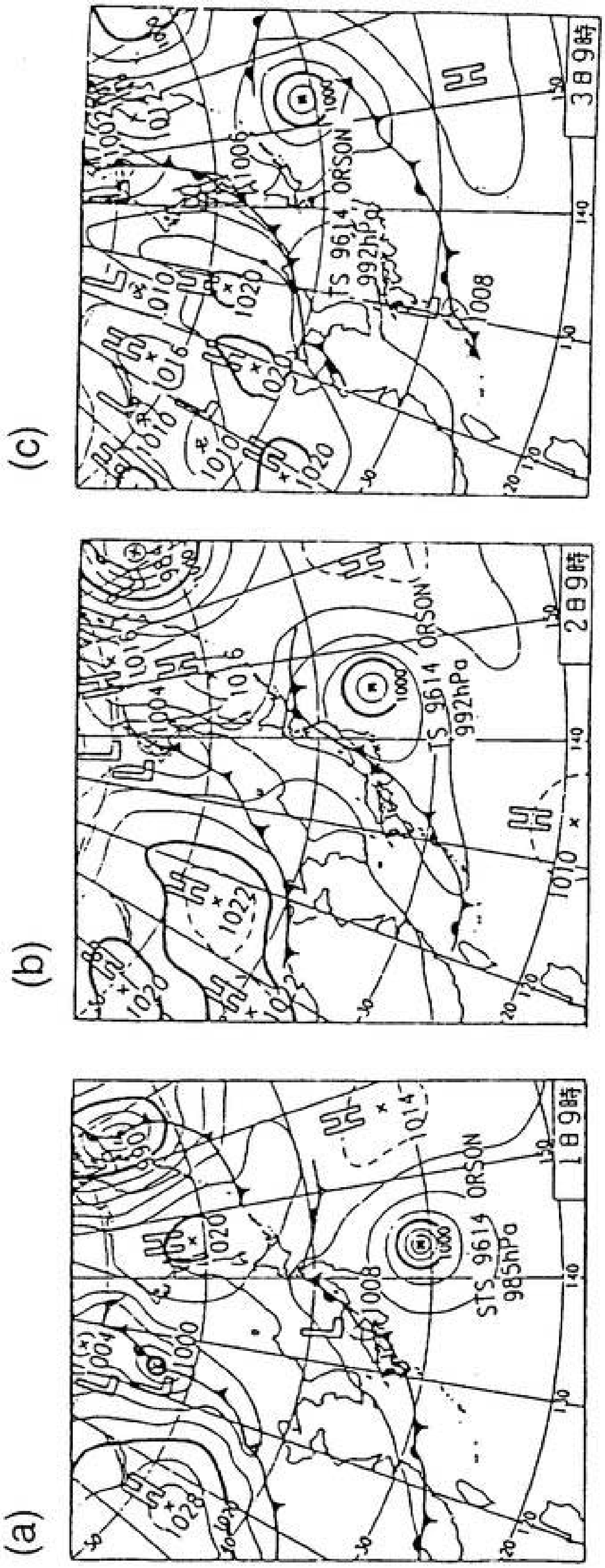

Figure 3.3: Weather maps at every 9(LST) of (a) Sep. 1, (b) Sep. 2, and (c) Sep. 3, 1996 (courtesy of JMA). The maps show that during these three days a front moved eastward across the Japanese Islands.

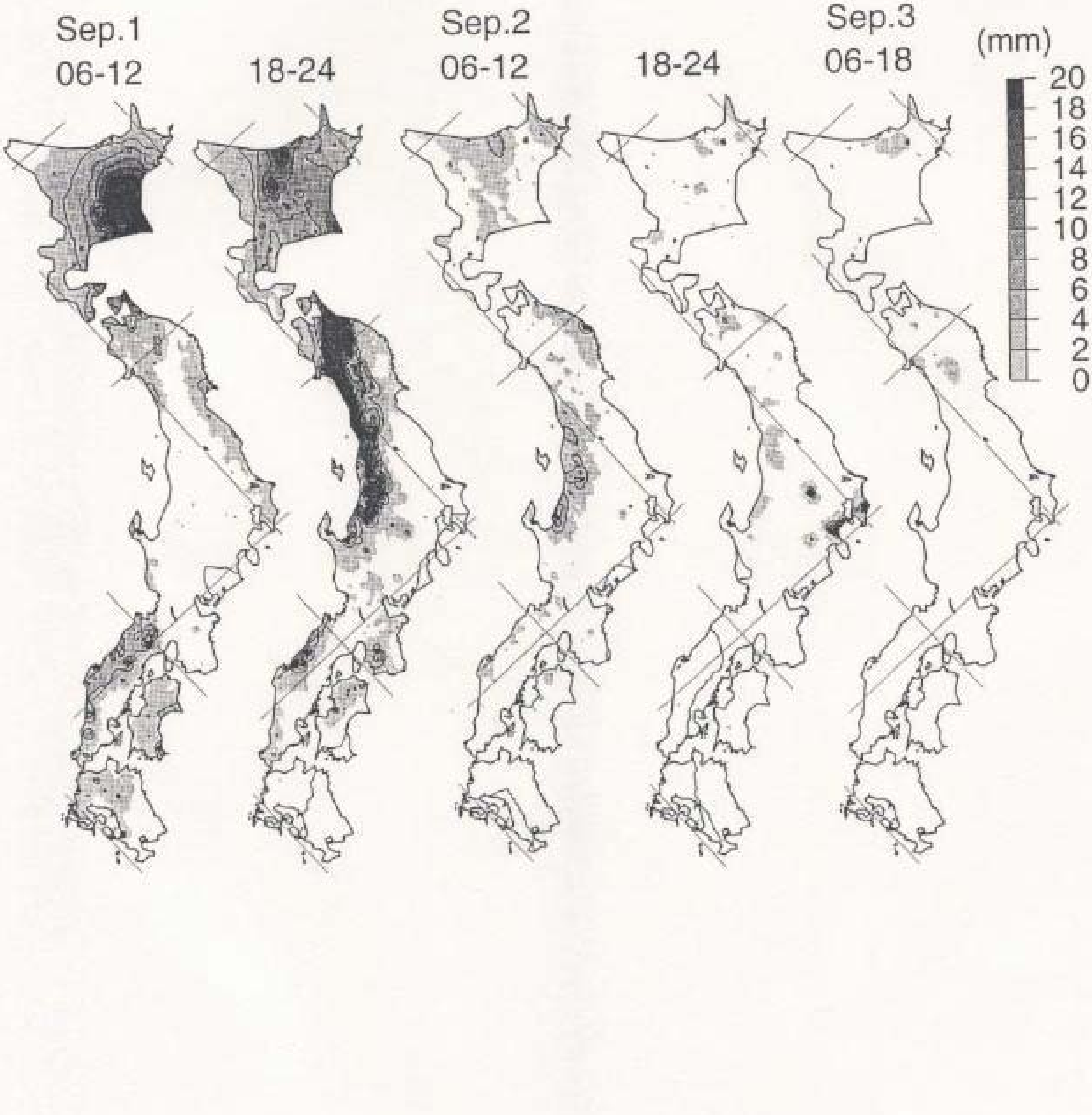

Figure 3.4: Precipitation over the Japanese Islands observed by AMeDAS for six hours before and after every 9(LST) and 21 (LST) from Sep. 1 to Sep. 3.

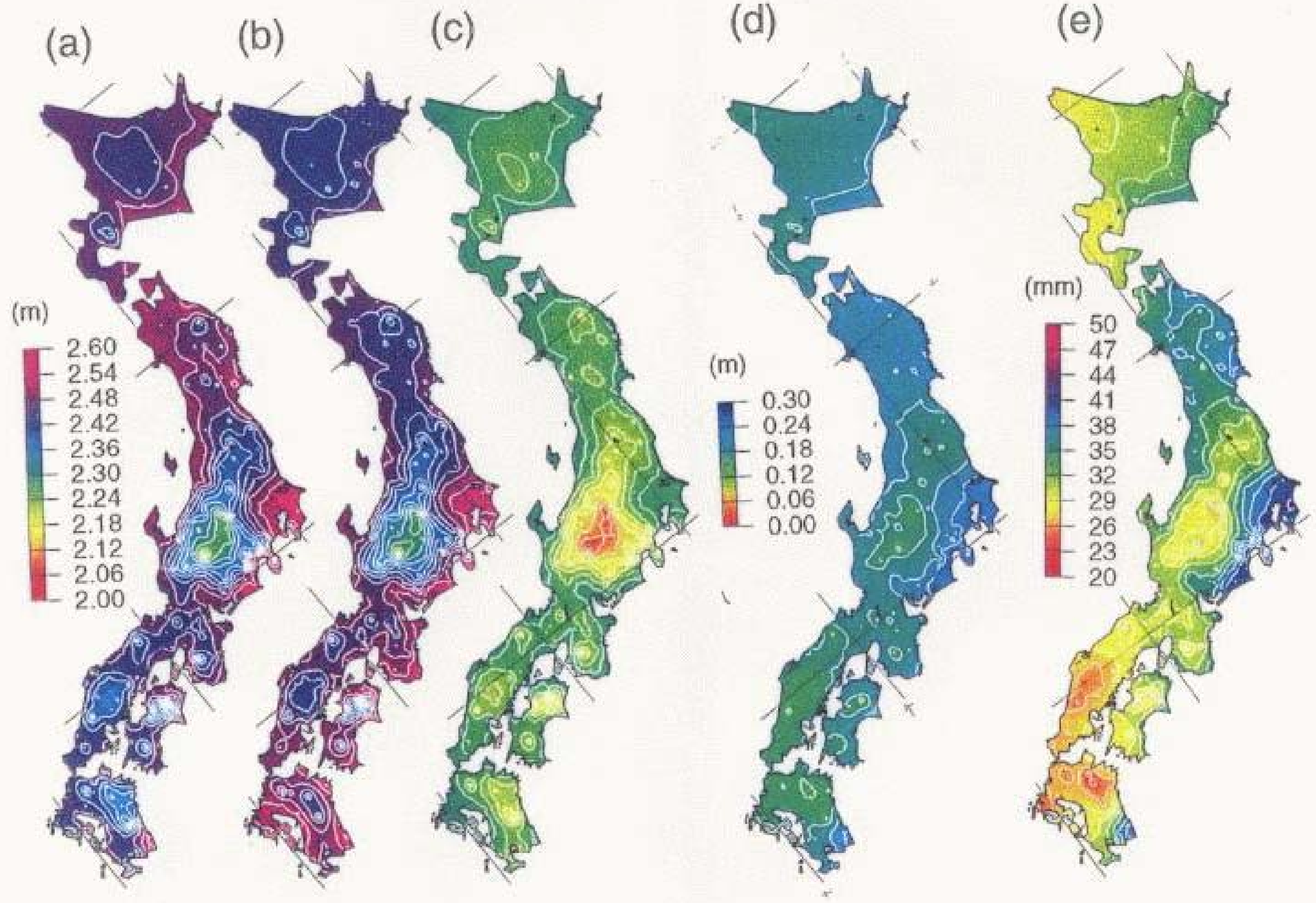

Figure 3.5: (a) Averaged ZTD retrieved three hourly from GSI's GPS array from 9(LST), Sep. 1 to 9(LST), Sep. 3, 1996. (b) Same as (a) but for during two months of August and September, 1996. (c) Averaged ZHD from 9(LST), Sept. 1 to 9(LST), Sept. 3, 1996 calculated half-daily from the Japan area objective analysis data in JMA. Note that color scales in (a), (b), and (c) are shown in left sides of the figures. (d) Averaged ZWD obtained by subtracting (c) from (a). (e) Averaged GPS retrieved PWV converted from (d). Contour intervals from (a) to (d) are 30 mm, and those for (e) are 1.5 mm.

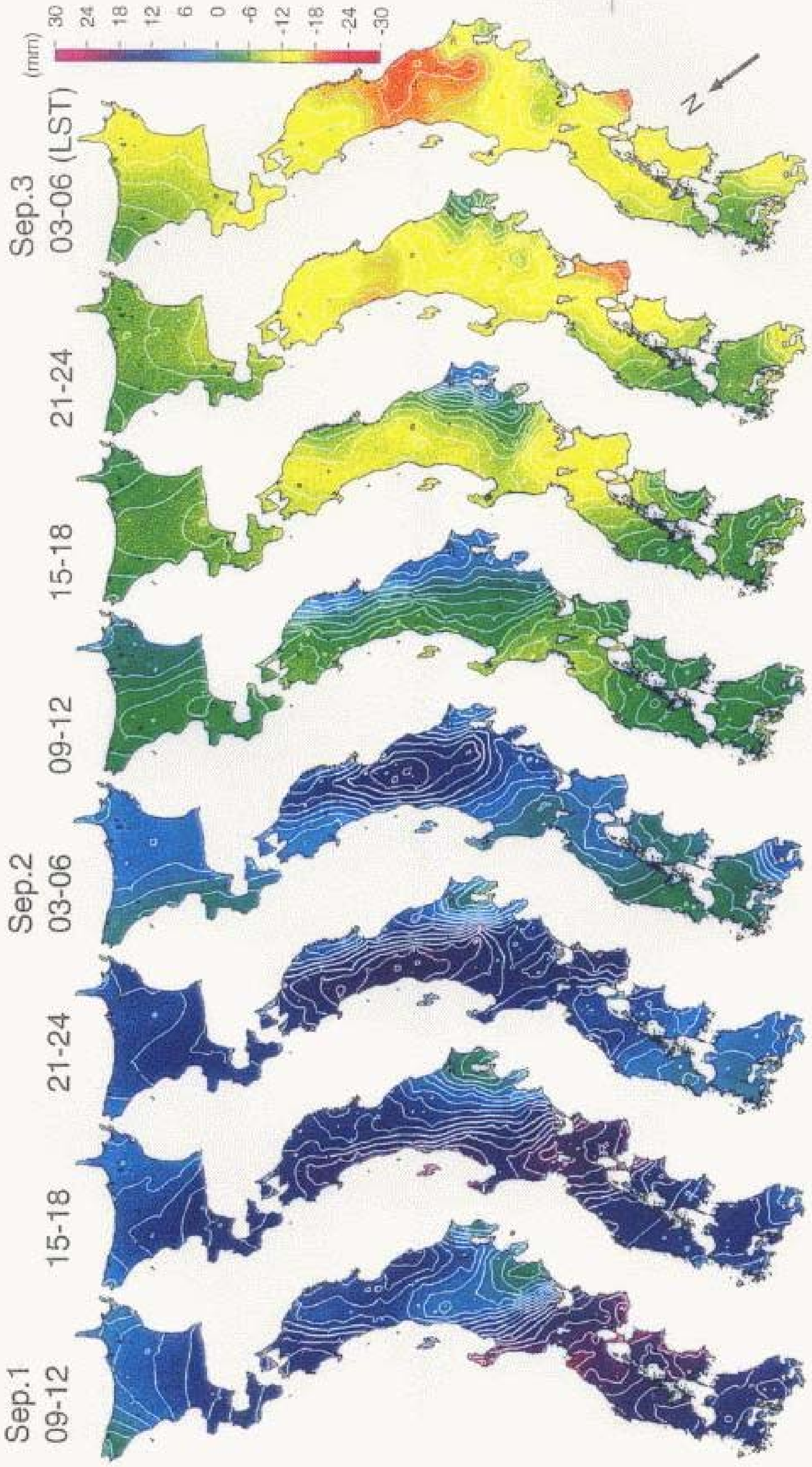

Figure 3.6: GPS retrieved six-hourly anomalies of PWV from the averaged PWV in Fig. 3.5e. Interpolated data of atmospheric surface pressure and Π from the half-daily Japan area objective analysis data are used for calculations of ZHD and conversion from ZWD into PWV. Contour interval is 2 mm.

(a) 09LST / Sep. 1 21LST 09LST / Sep.2 21LST 09LST / Sep.3

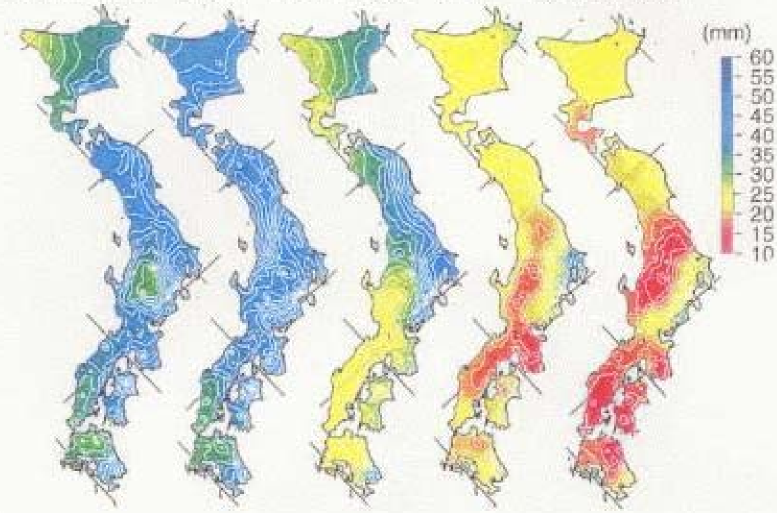

(b) 09LST / Sep. 1 21LST 09LST / Sep.2 21LST 09LST / Sep.3

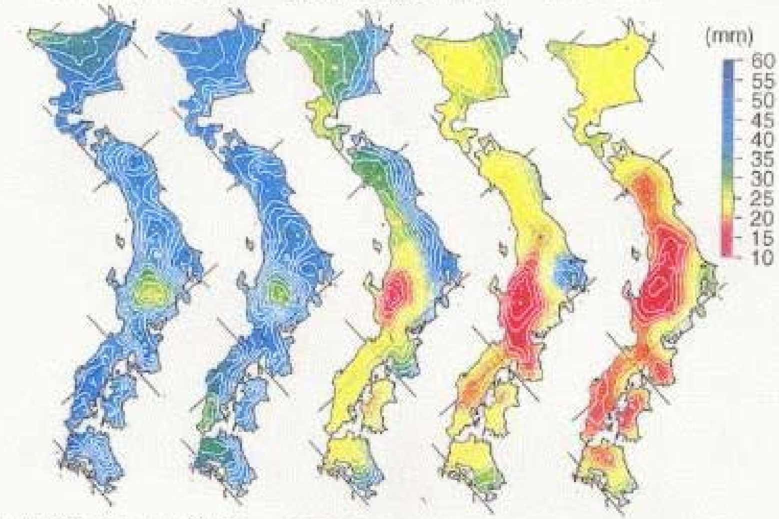

(c) 09LST / Sep. 1 21LST 09LST / Sep.2 21LST 09LST / Sep.3

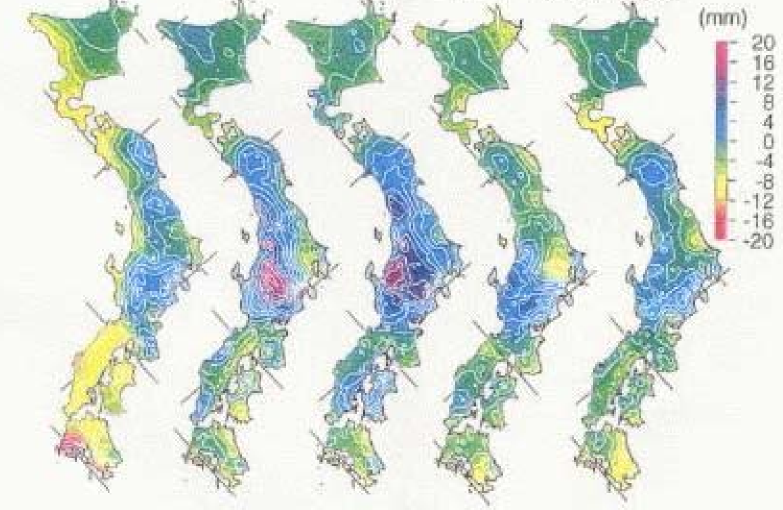

Figure 3.7: (a) Twelve-hourly GPS PWV from 9(LST), Sep. 1 to 9(LST), Sep. 3 calculated from ZTD for six hours before and after every 9(LST) and 21(LST) from Sep. 1 to Sep. 3, where twelve-hourly Japan area objective analysis data are used for computing ZHD and Π. (b) Same as (a) but for NWP PWV. (c) GPS PWV minus NWP PWV obtained by subtracting (b) from (a).

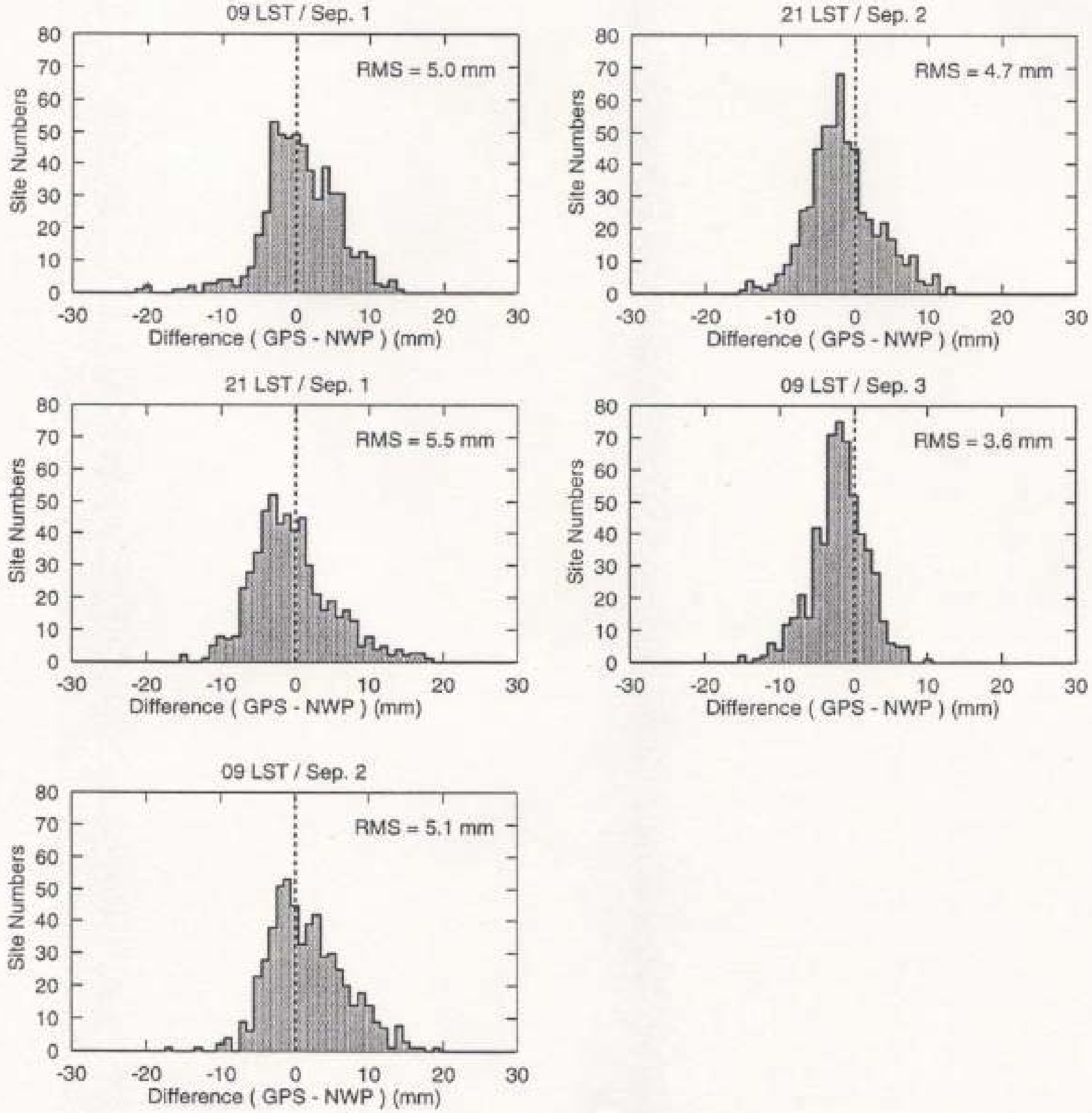

Figure 3.8: Histograms of GPS PWV minus NWP PWV shown in Fig. 3.7c.

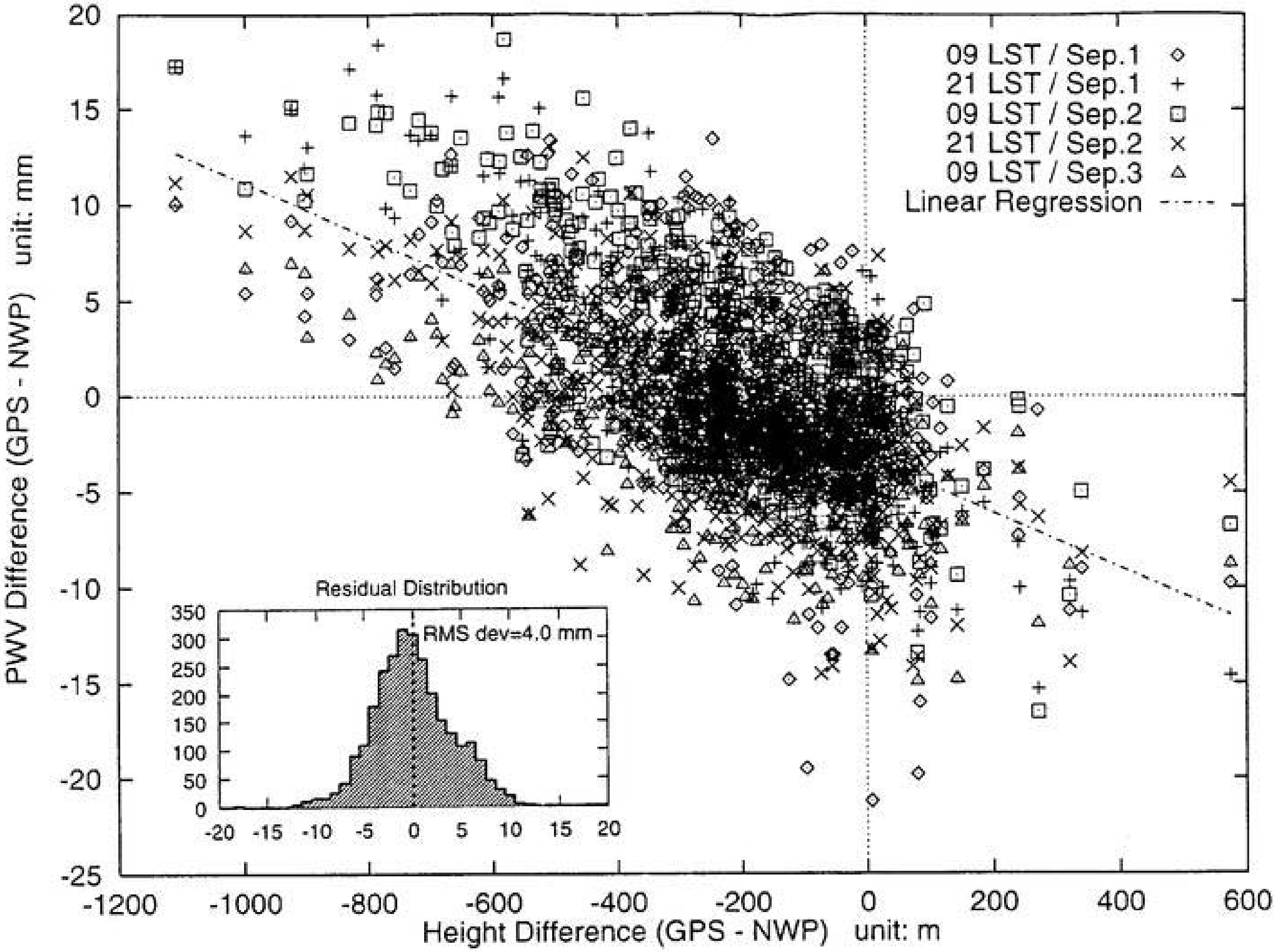

Figure 3.9: Dependency of GPS PWV minus NWP PWV shown in Fig. 3.7c upon GPS site's topographic height minus NWP model's topographic height shown in Fig. 3.1c, where a dashed line indicates the linear regression line obtained by least-square fitting through the all data. There still exists a mean bias of -3.2 mm not due to difference in height, suggesting underestimation of GPS PWV with respect to NWP PWV. The gradient in the regression line is -1.4 mm/100 m. The histogram shows the distribution of residuals around the regression line.

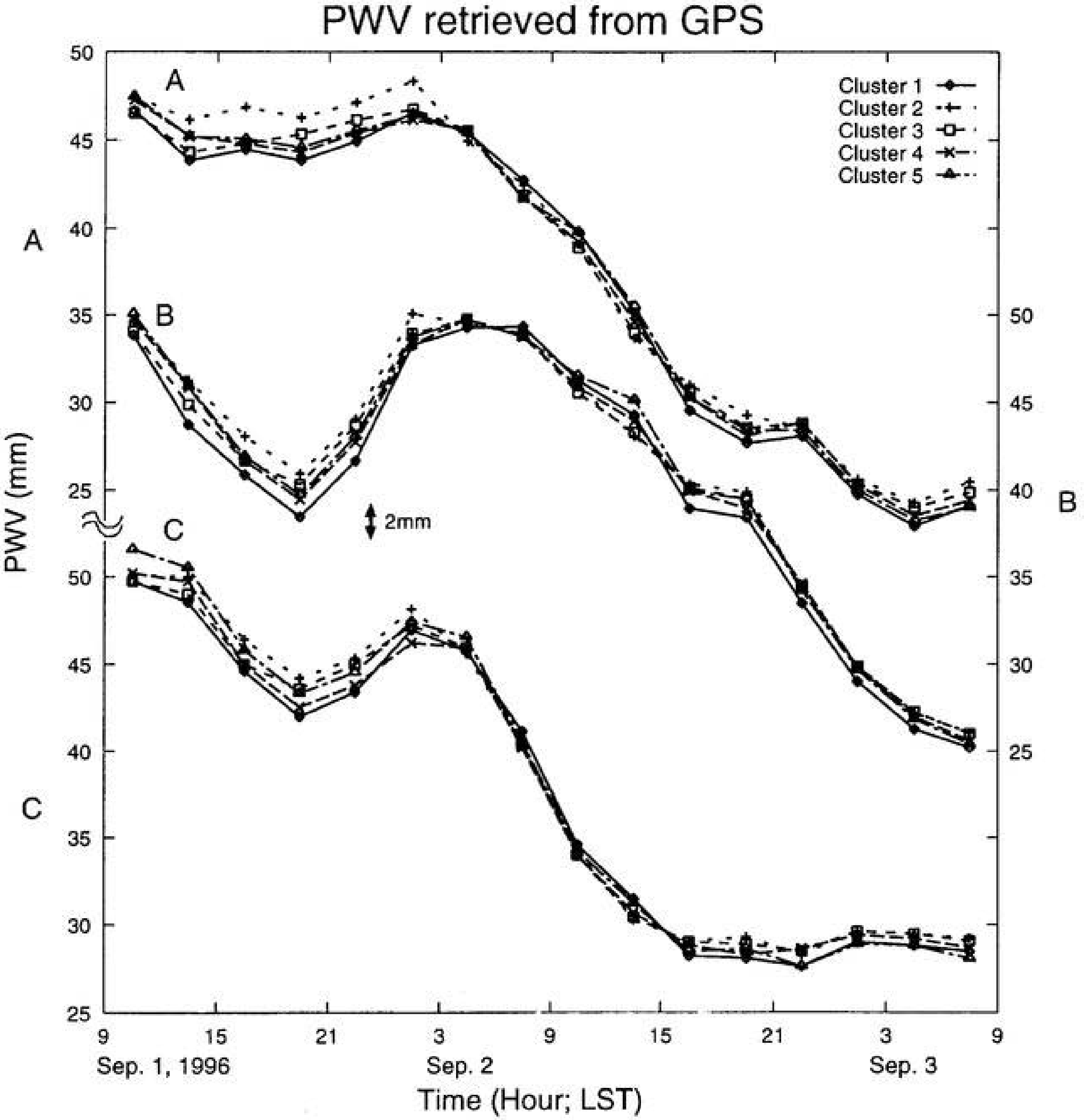

Figure 3.10: GPS PWV series from 9(LST), Sep.1 to 9(LST), Sep.3 for the three back-bone (BB) sites in Trimble cluster indicated as A, B, and C of northern, central, and southern parts of Japan, respectively, shown in Fig. 3.1a, at which five values of PWV are estimated for the five regional clusters.

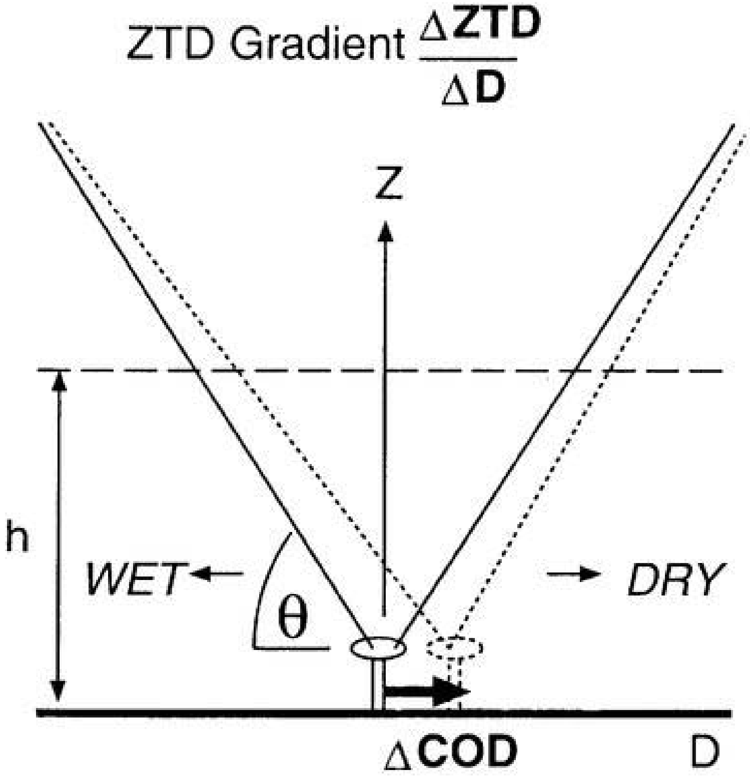

Figure 3.11: A conceptual figure showing a relationship between horizontal coordinate variation and ZTD gradient. θ, COD, h, D show the elevation angle of GPS satellites, horizontal coordinate solution, scale height of water vapor, distance on the surface, and ΔCOD and $\frac{\Delta ZTD}{\Delta D}$ show horizontal coordinate variation and ZTD gradient, respectively.

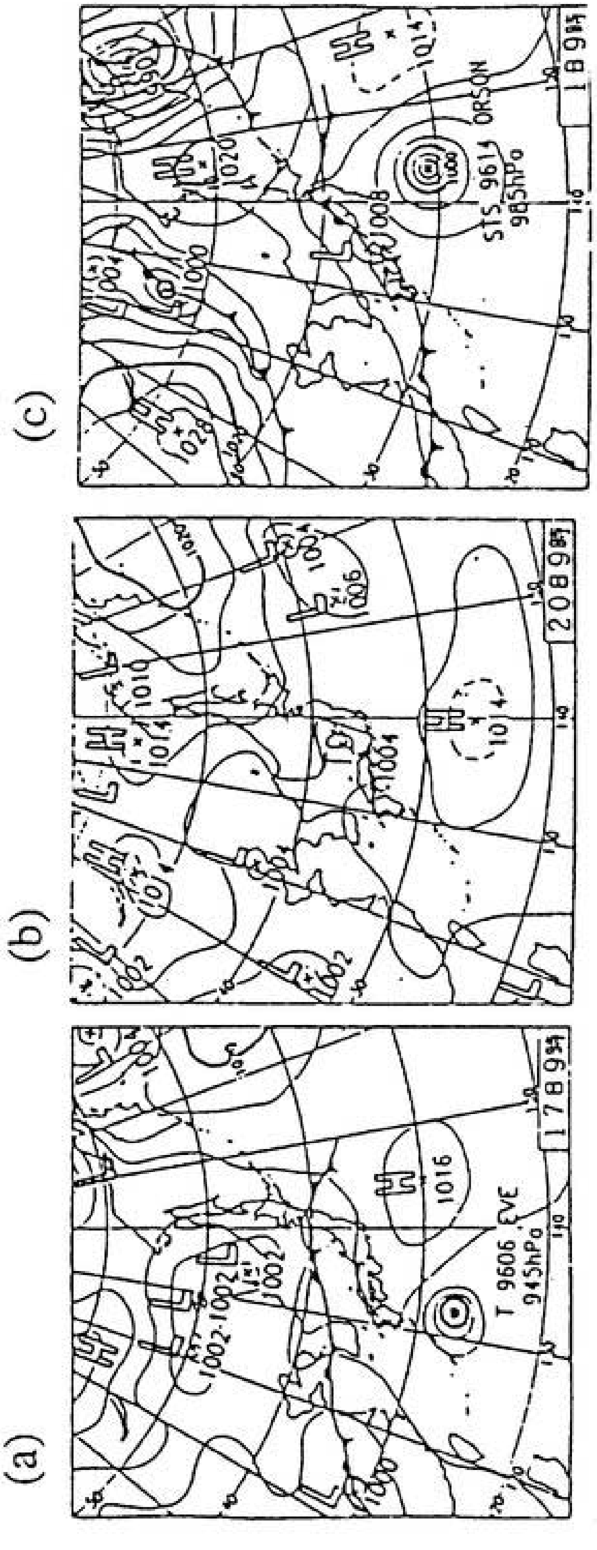

Figure 3.12: Weather maps at every 9(LST) of (a) Jul. 17, (b) Jul. 20, and (c) Sep. 1, 1996 (courtesy of JMA). (a) and (c) show fronts extended E-W and N-S over the Japanese Island, respectively, and (b) shows tropical cyclone over the central region of Japan.

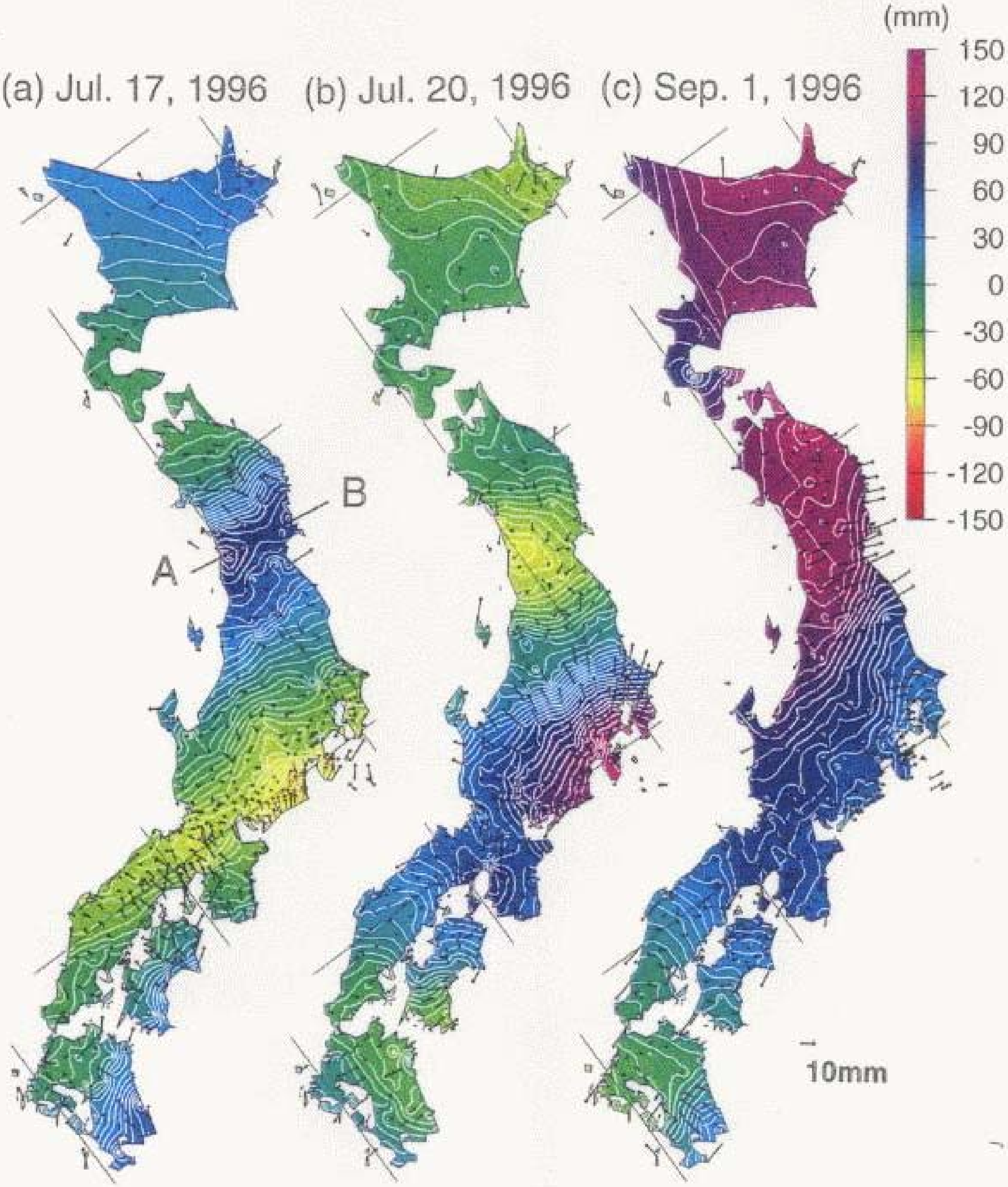

Figure 3.13: Horizontal coordinate anomalies in three cases from 14 days - averaged value of the periods (a) Jul. 16 to Jul. 29, and (b) Aug. 28 to Sep. 10 with distribution map of ZTD anomaly calculated in a similar way. The sites which show smallest ZTD gradient are selected as reference points The case (c) corresponds to Fig. 3.6. Contour interval is 10 mm.

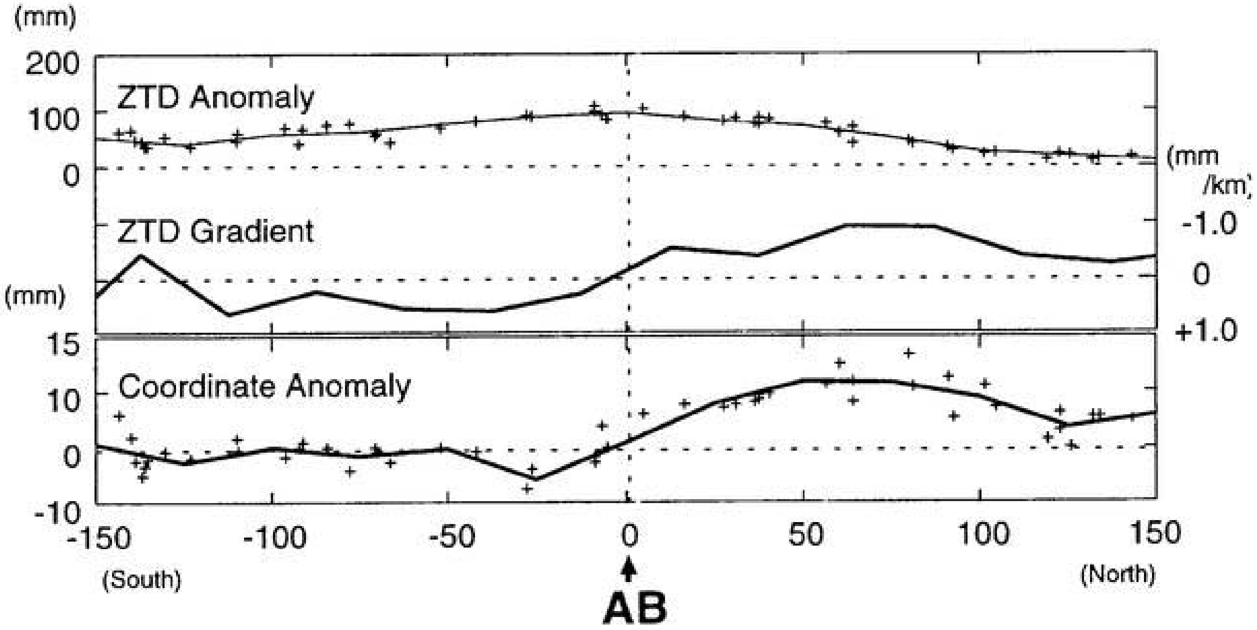

Figure 3.14: ZTD anomaly, its gradient, and coordinate anomaly in GPS sites around line AB showing maximum value of ZTD in Fig. 3.13a. The x-axis shows length from AB. Solid lines show averaged value every 25 km AB in Fig. 3.13a.

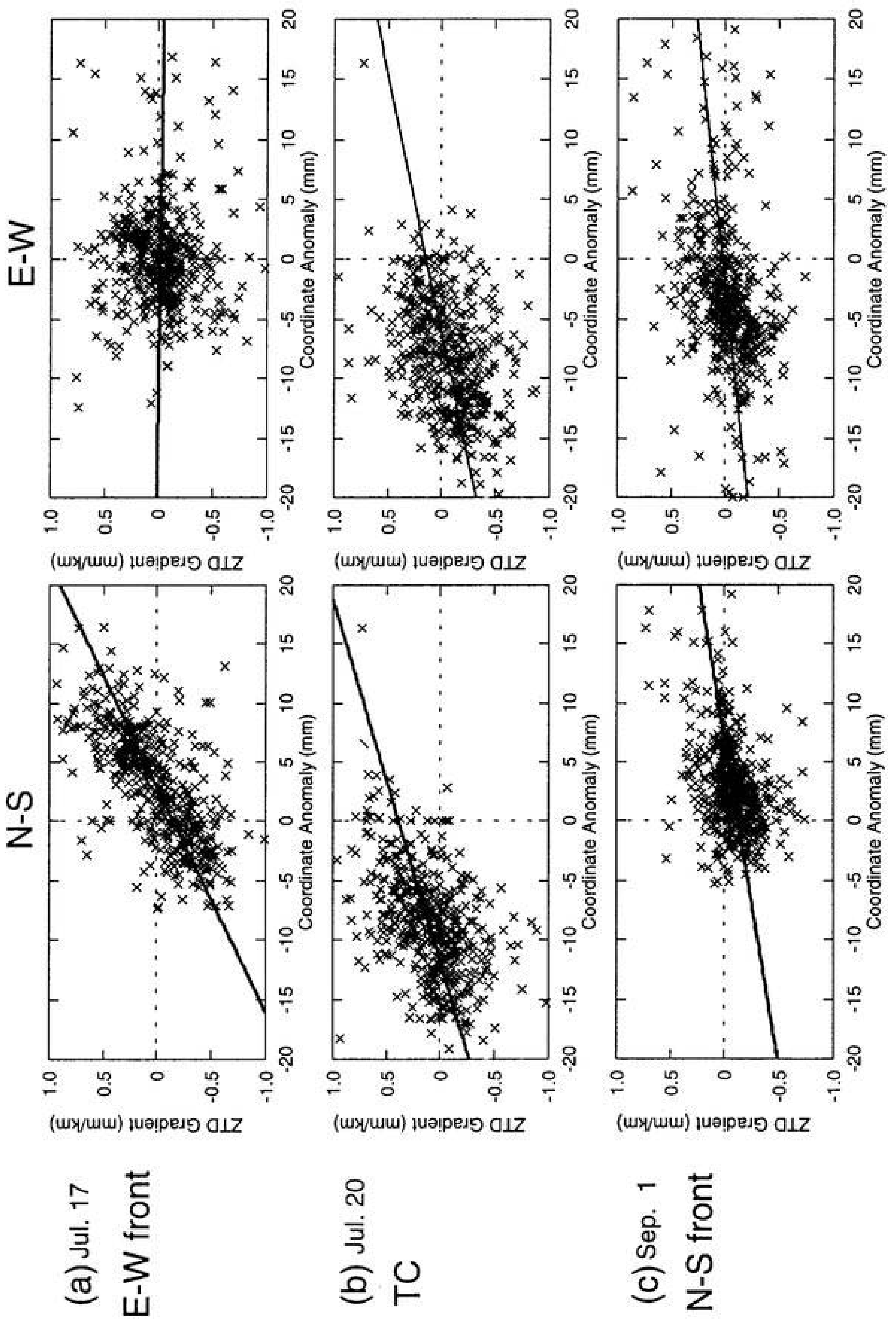

Figure 3.15: Correlation diagrams of three cases in Fig. 3.12, which show the relationship between horizontal coordinate variations and the ZTD gradients in N-S and E-W components.

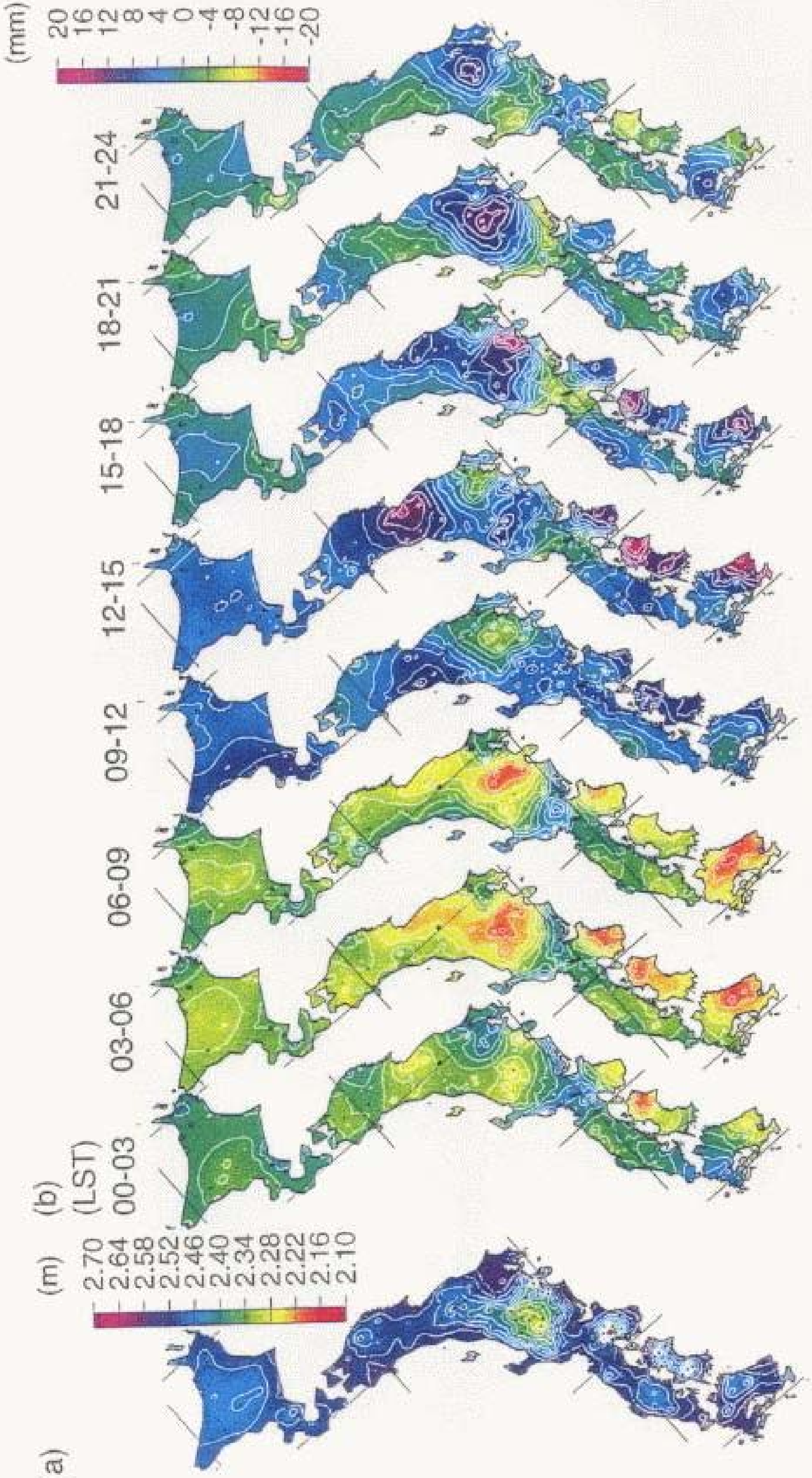

Figure 3.16: (a) Averaged ZTD retrieved three hourly from GSI's GPS array for during one month of July, 1996. Contour interval is 0.03 m. (b) three-hourly anomalies of monthly composite ZTD from (a). Contour interval is 2 mm

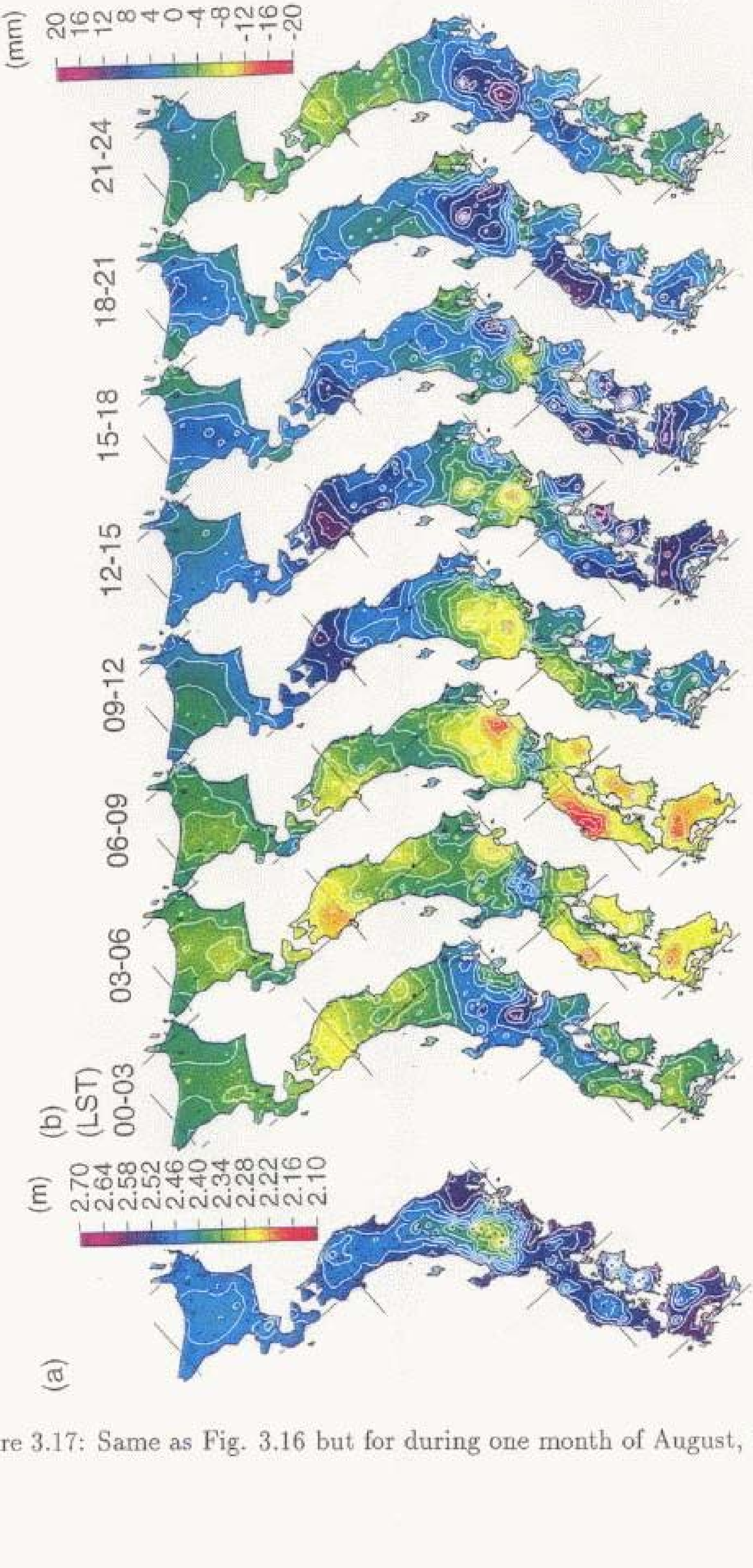

Figure 3.17: Same as Fig. 3.16 but for during one month of August, 1996.

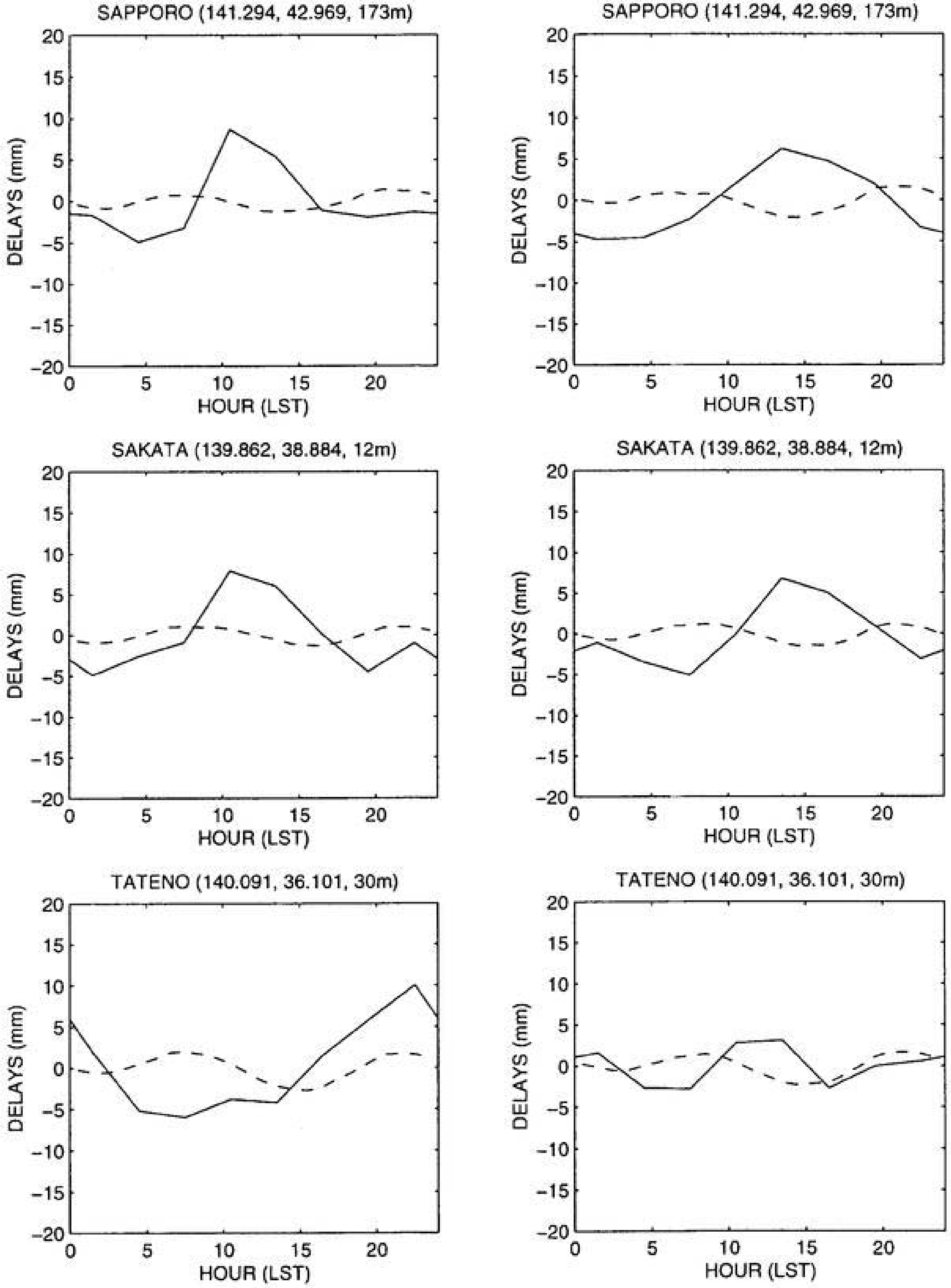

SAPPORO (141.294, 42.969, 173m)

SAPPORO (141.294, 42.969, 173m)

SAKATA (139.862, 38.884, 12m)

SAKATA (139.862, 38.884, 12m)

TATENO (140.091, 36.101, 30m)

TATENO (140.091, 36.101, 30m)

Figure 3.18: Diurnal variations of ZTD (solid line) and ZHD (dashed line) at Sapporo, Sakata, and Tateno in July (left panels) and August (right panels), 1996.

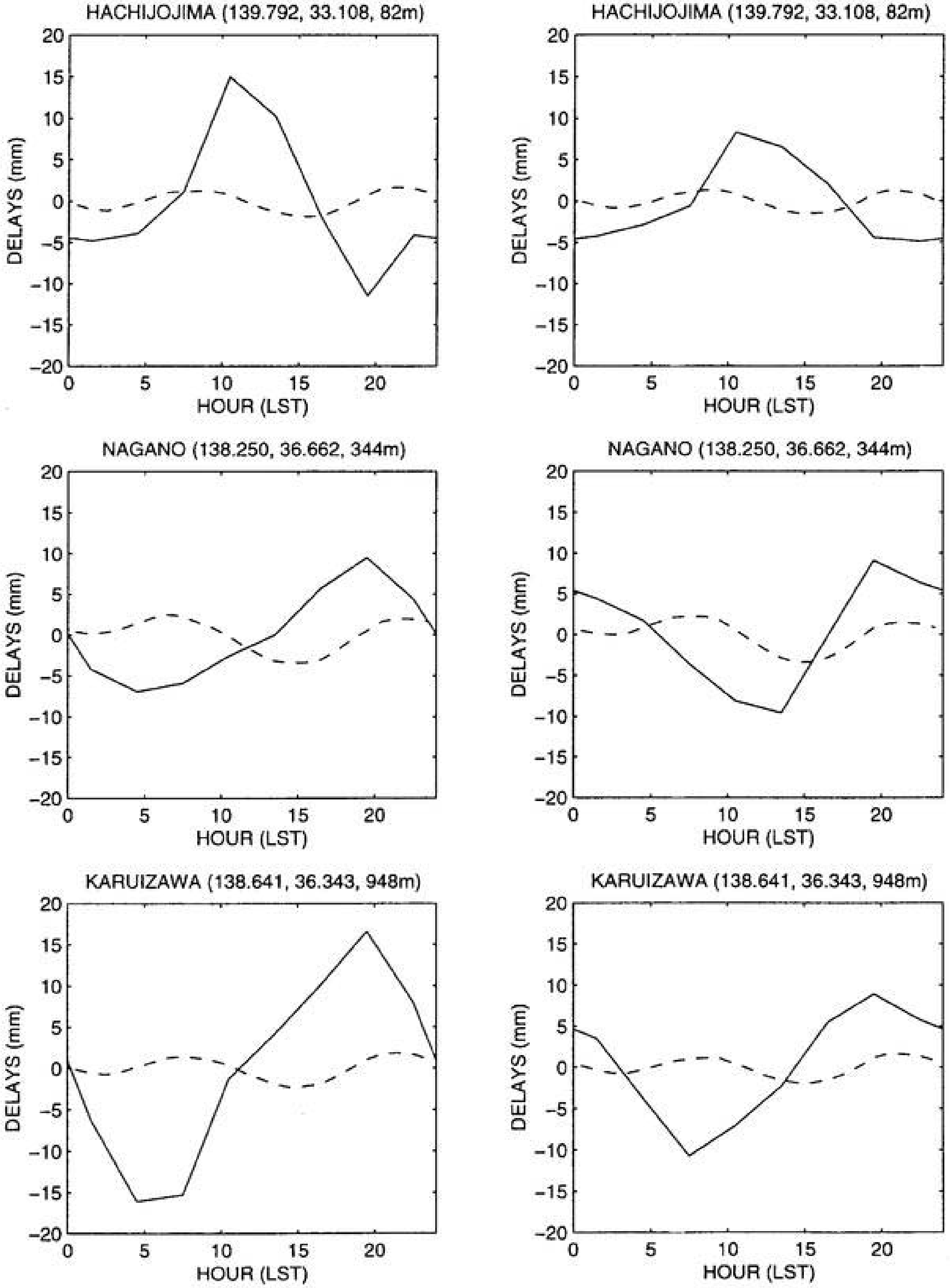

Figure 3.19: Same as Fig. 3.18 but at Hachijojima, Nagano, and Karuizawa.

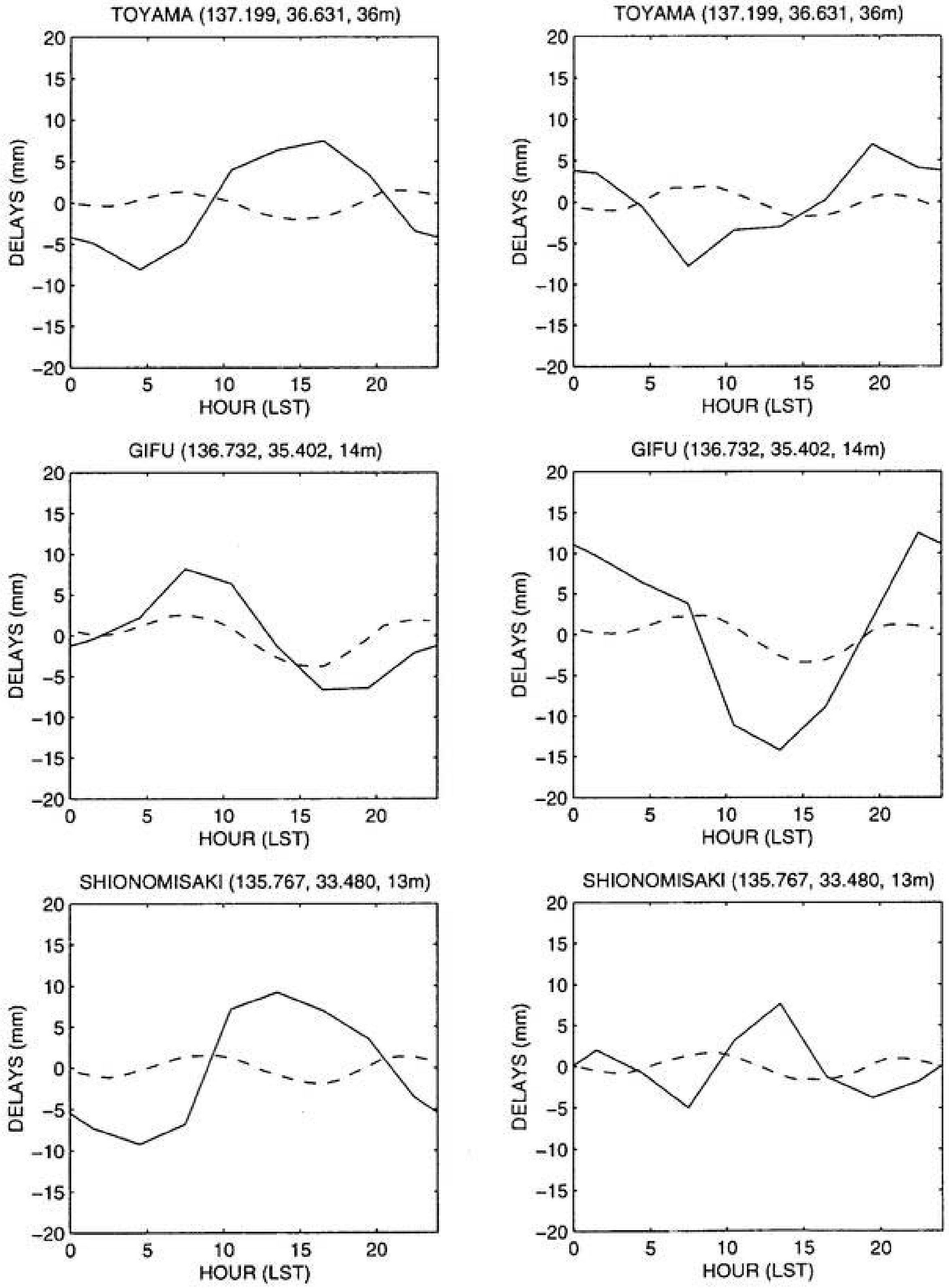

Figure 3.20: Same as Fig. 3.18 but at Toyama, Gifu, and Shionomisaki.

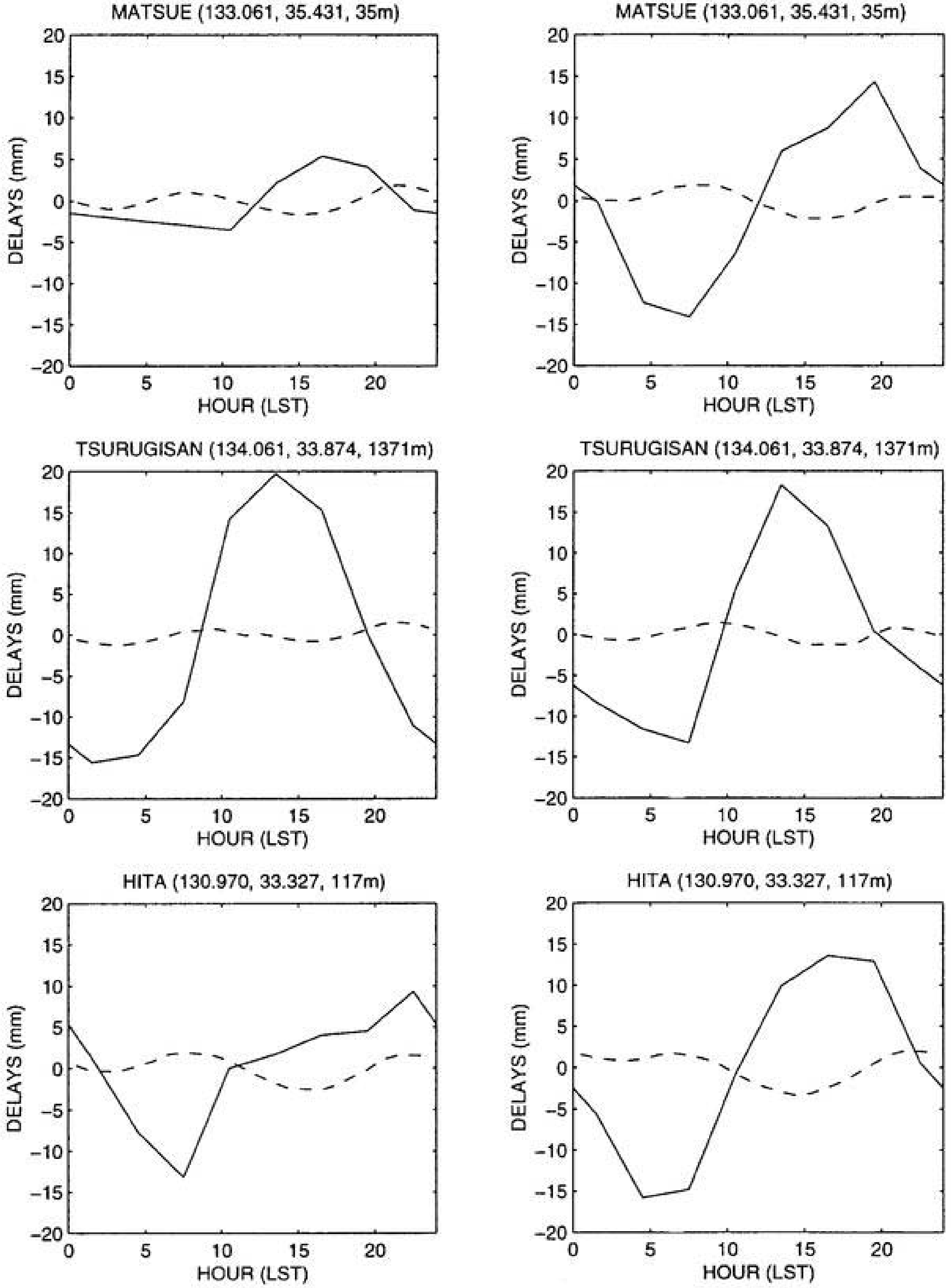

Figure 3.21: Same as Fig. 3.18 but at Matsue Tsurugisan, and Hita.

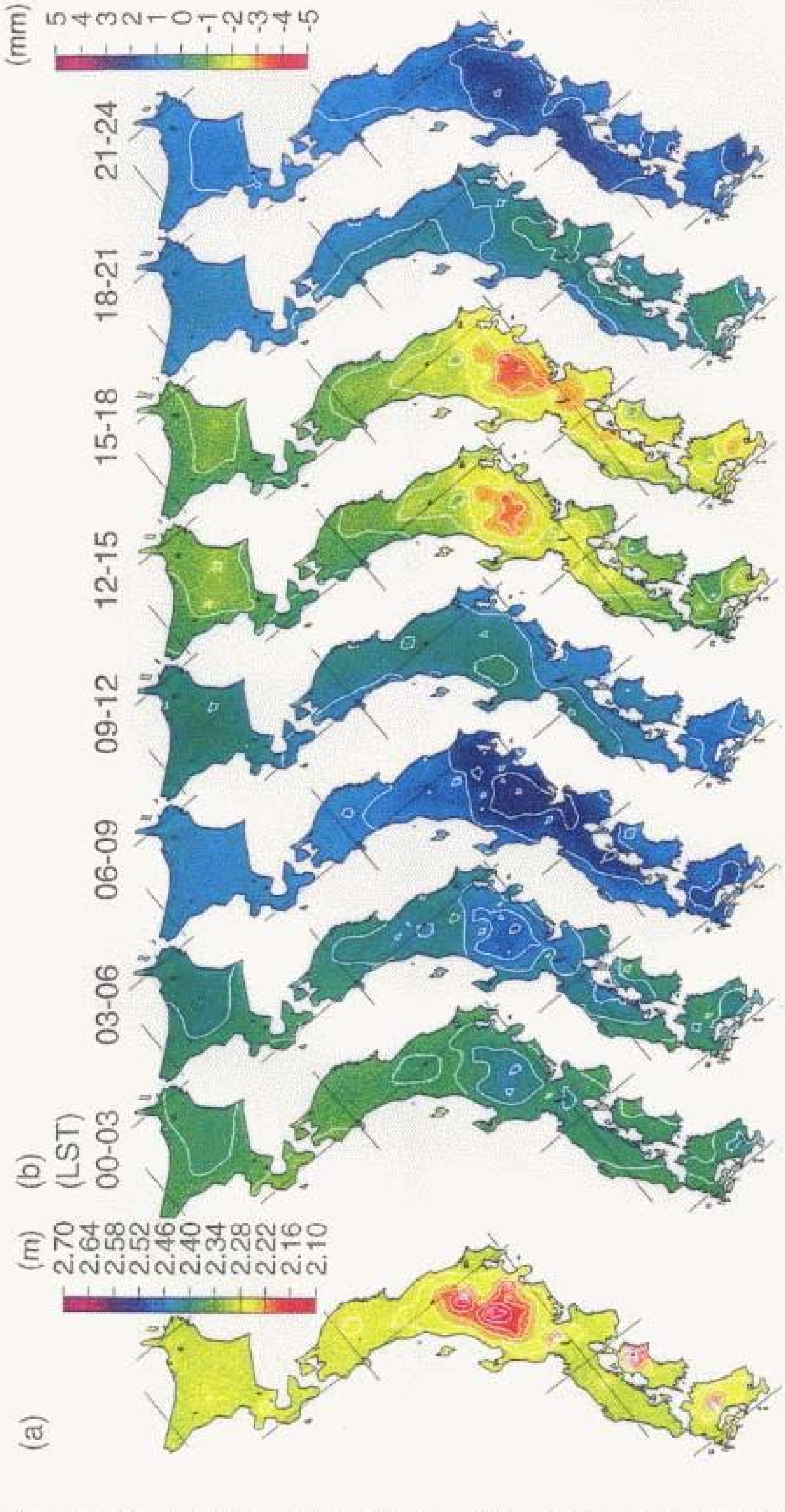

Figure 3.22: (a) Averaged ZHD calculated from surface pressure at weather stations of JMA for during one month of July, 1996, which corresponds to Fig. 3.16. Contour interval is 0.03 m. (b) three-hourly anomalies of monthly composite ZHD from (a). Contour interval is 1 mm.

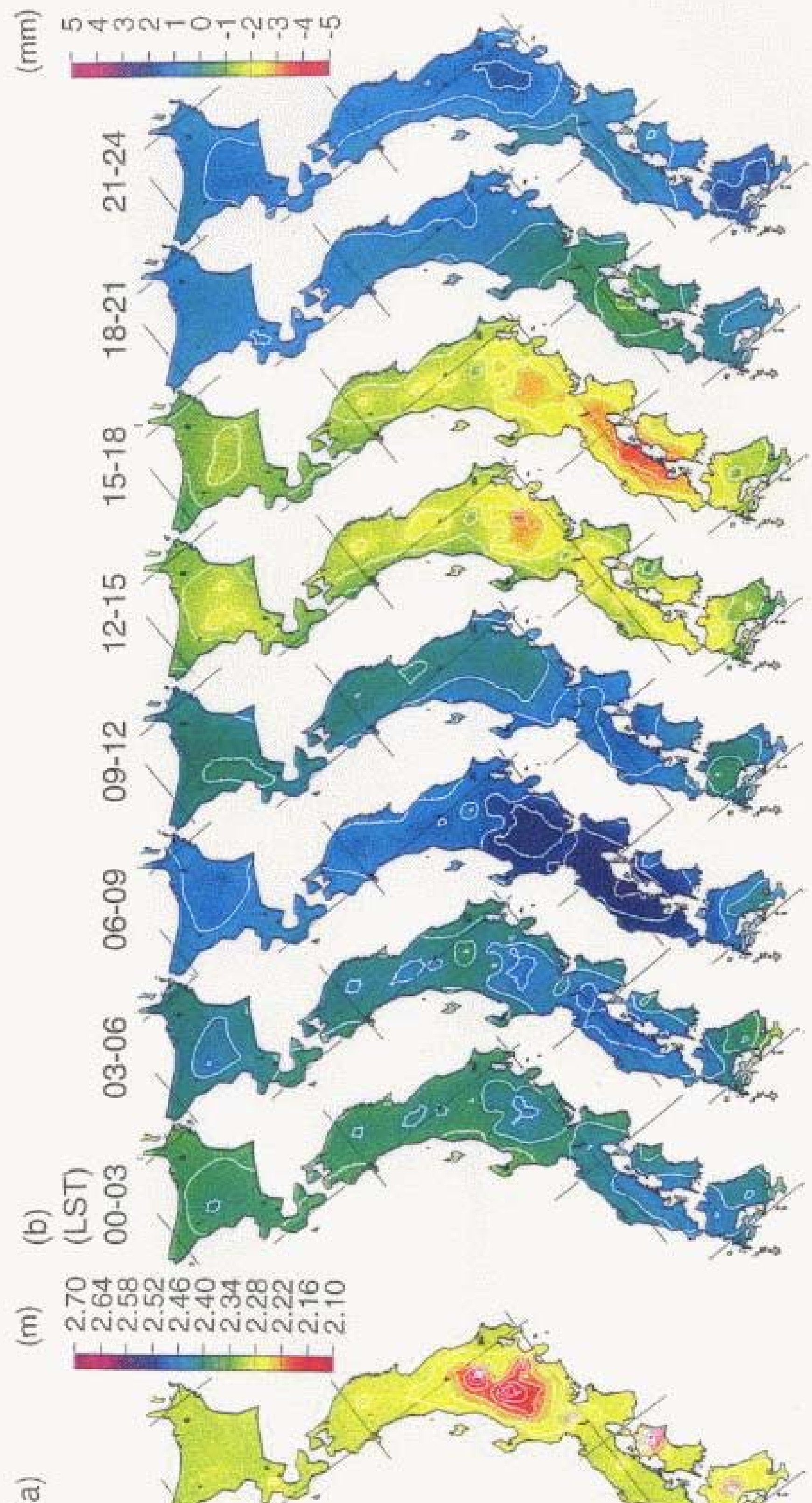

Figure 3.23: Same as Fig. 3.22 but for during one month of August, 1996, which corresponds to Fig. 3.17.

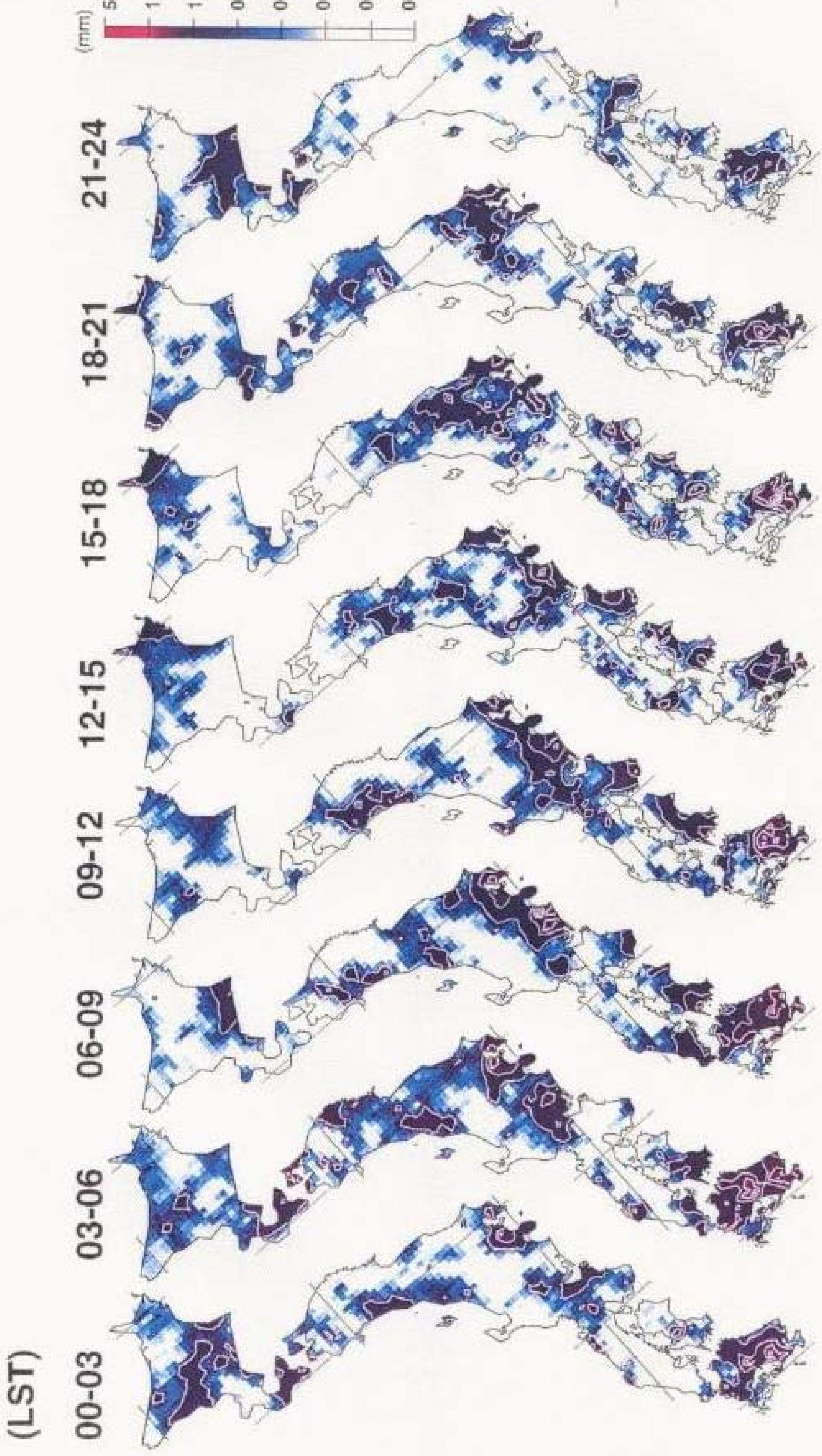

Figure 3.24: Diurnal variation of three-hourly precipitation over the Japanese Islands observed by AMeDAS during one month of July, 1996, which corresponds to Fig. 3.16. Contour interval is 1.0 mm.

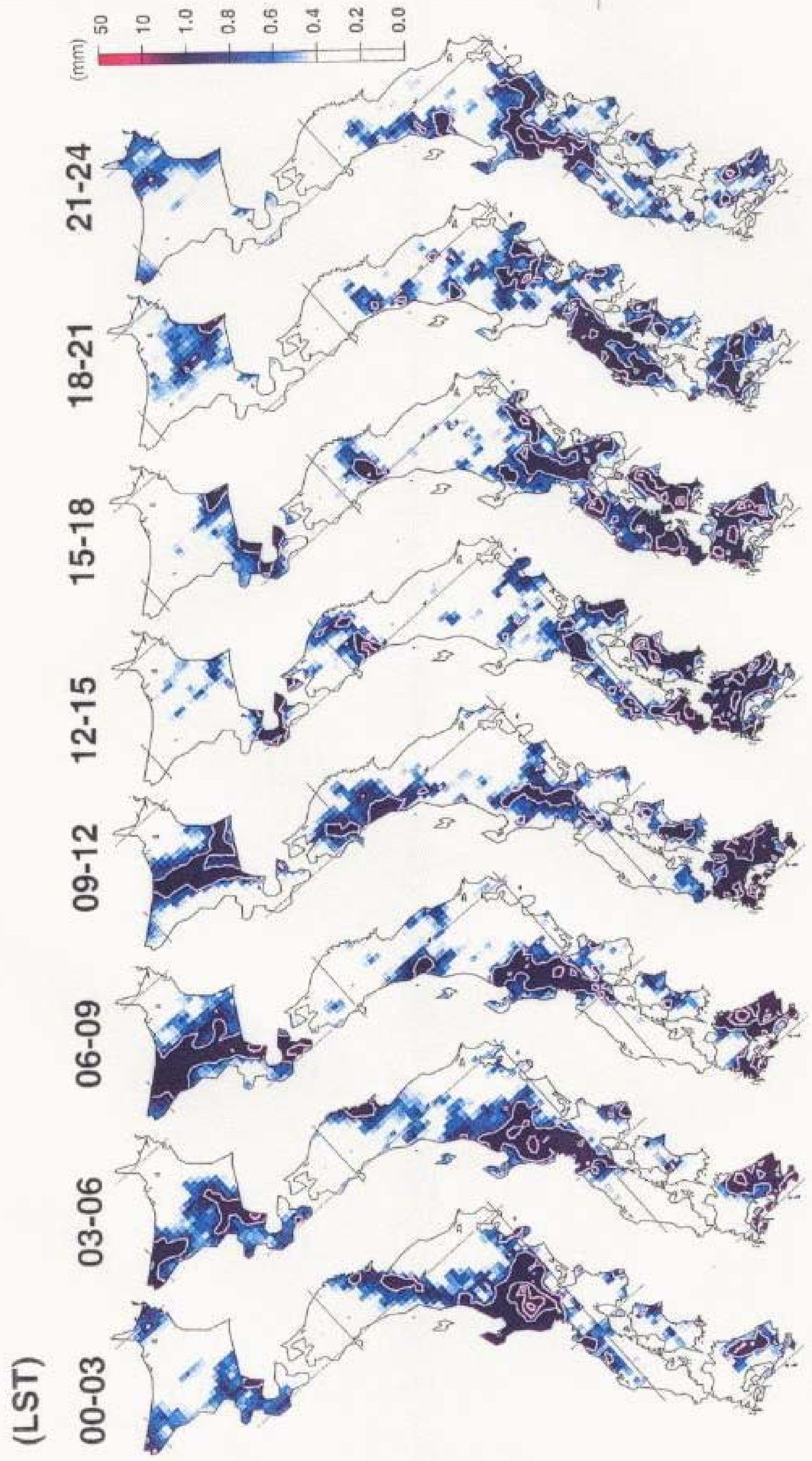

Figure 3.25: Same as Fig. 3.24 but during one month of August, 1996, which corresponds to Fig. 3.17.

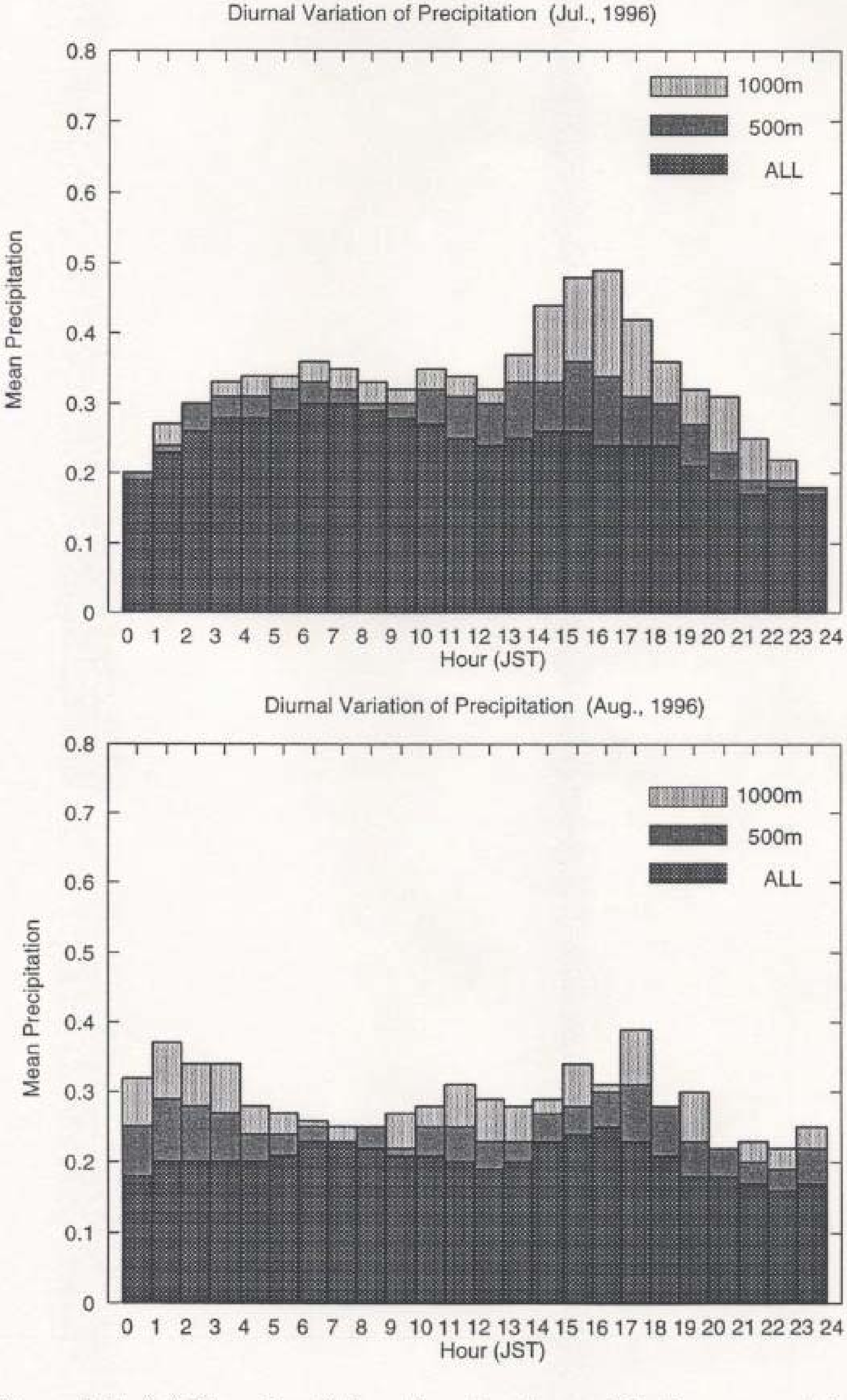

Figure 3.26: (a) Diurnal variation of one-hourly precipitation averaged for 1315 stations of AMeDAS of JMA (indicated by a sign ALL), for 258 stations whose height are more than 500m (500m), for 78 stations whose height are more than 1000m (1000m) for during one month of July (upper panel) and August (lower panel), 1996 (see Fig. 3.24).

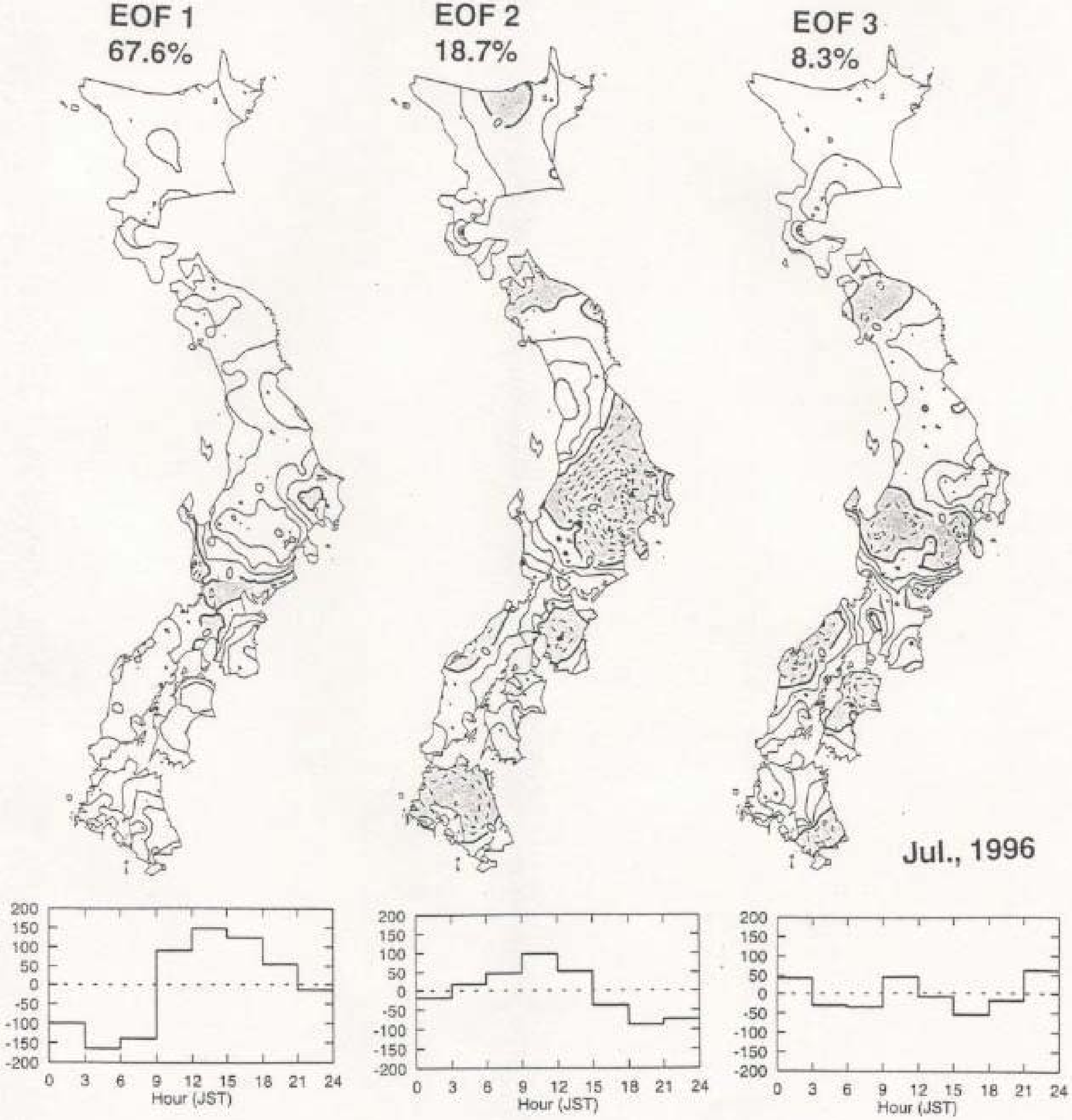

Figure 3.27: Distribution map of the first, second, and third EOFs of ZTD in July, 1996 over the Japanese Islands and its time coefficient. The contour interval is 0.02. Solid (dashed) lines represent positive (negative) value. The shaded regions show negative value of EOF.

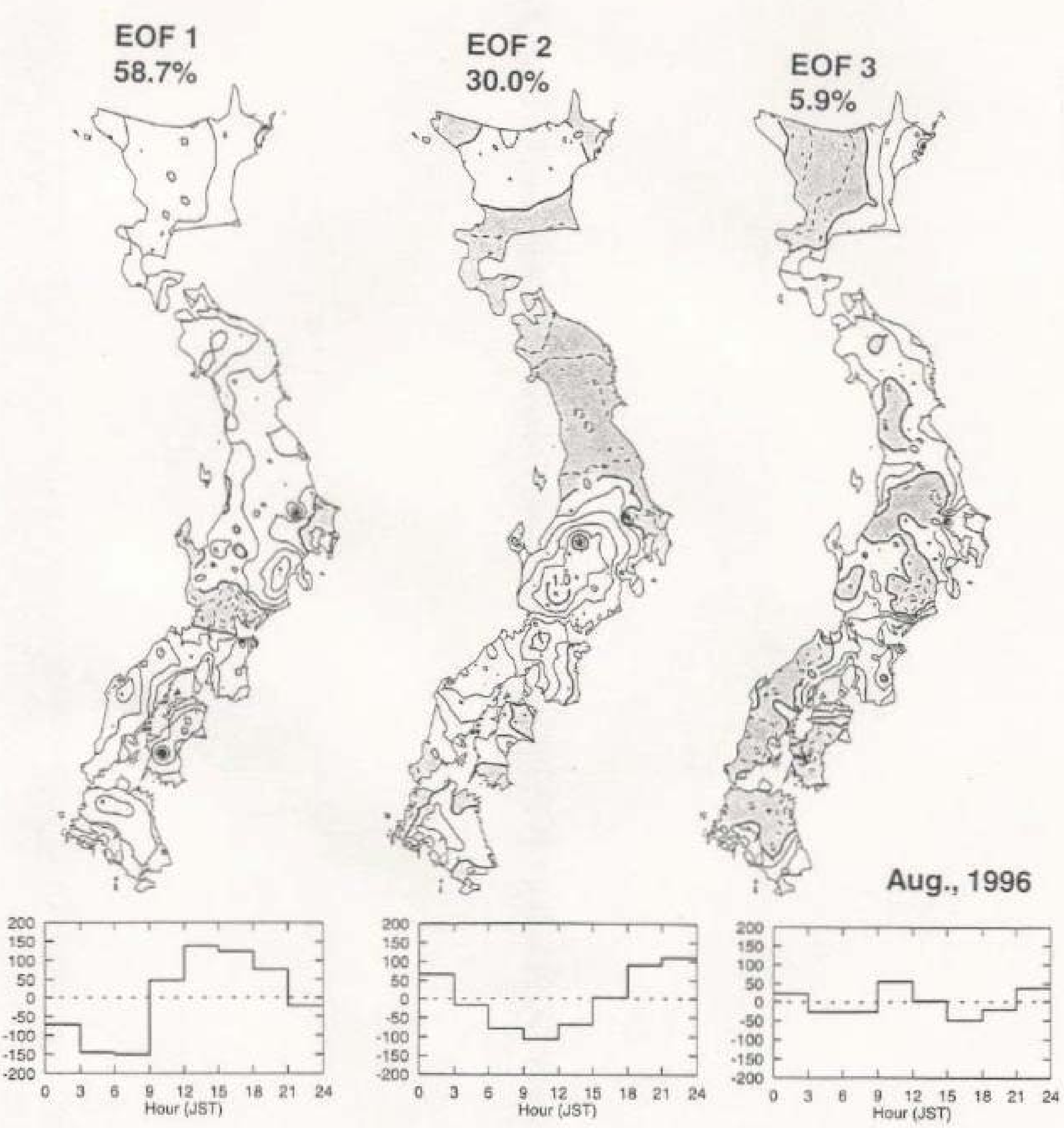

Figure 3.28: Same as Fig. 3.27, but in August, 1996

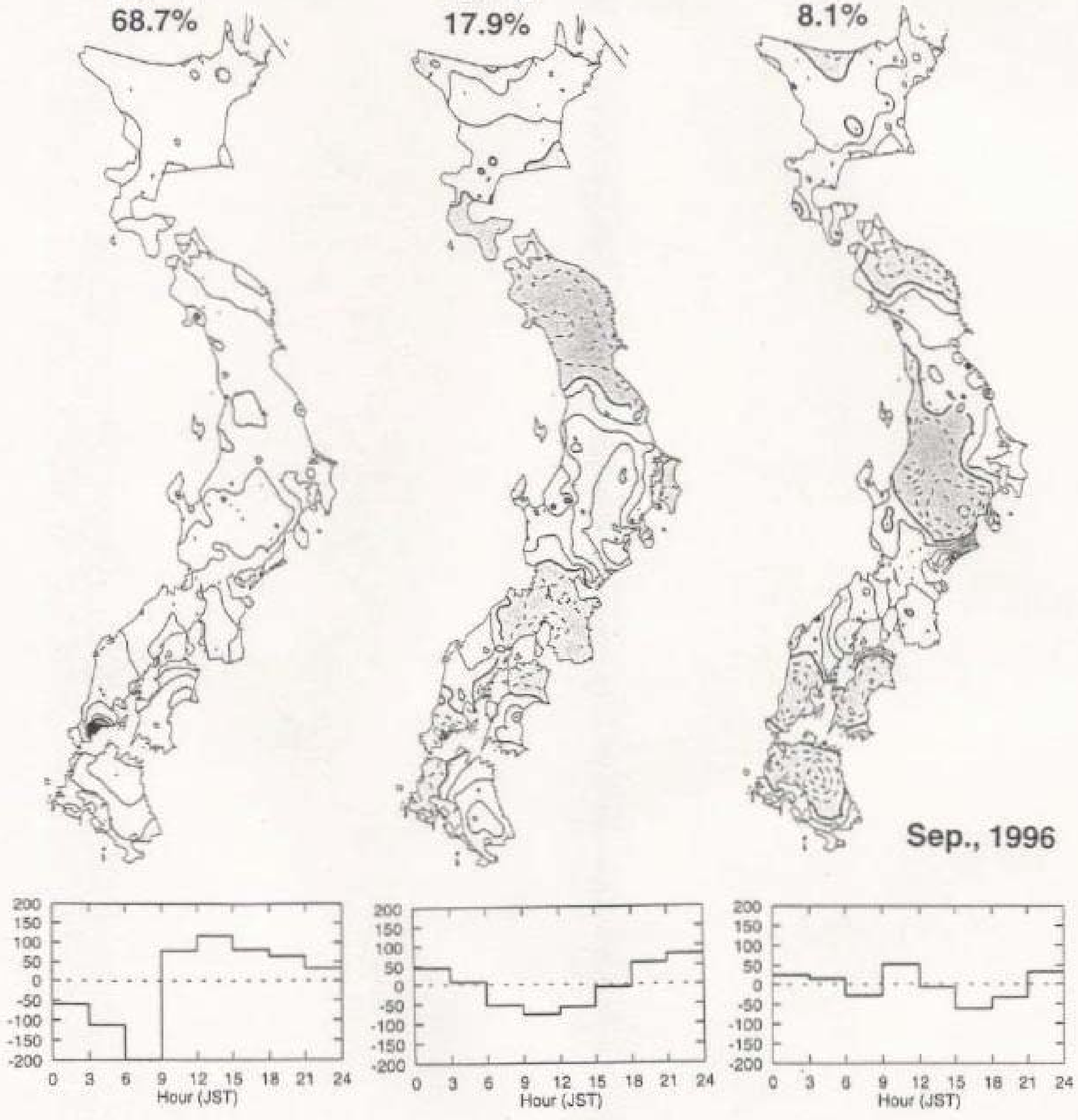

Figure 3.29: Same as Fig. 3.27, but in September, 1996

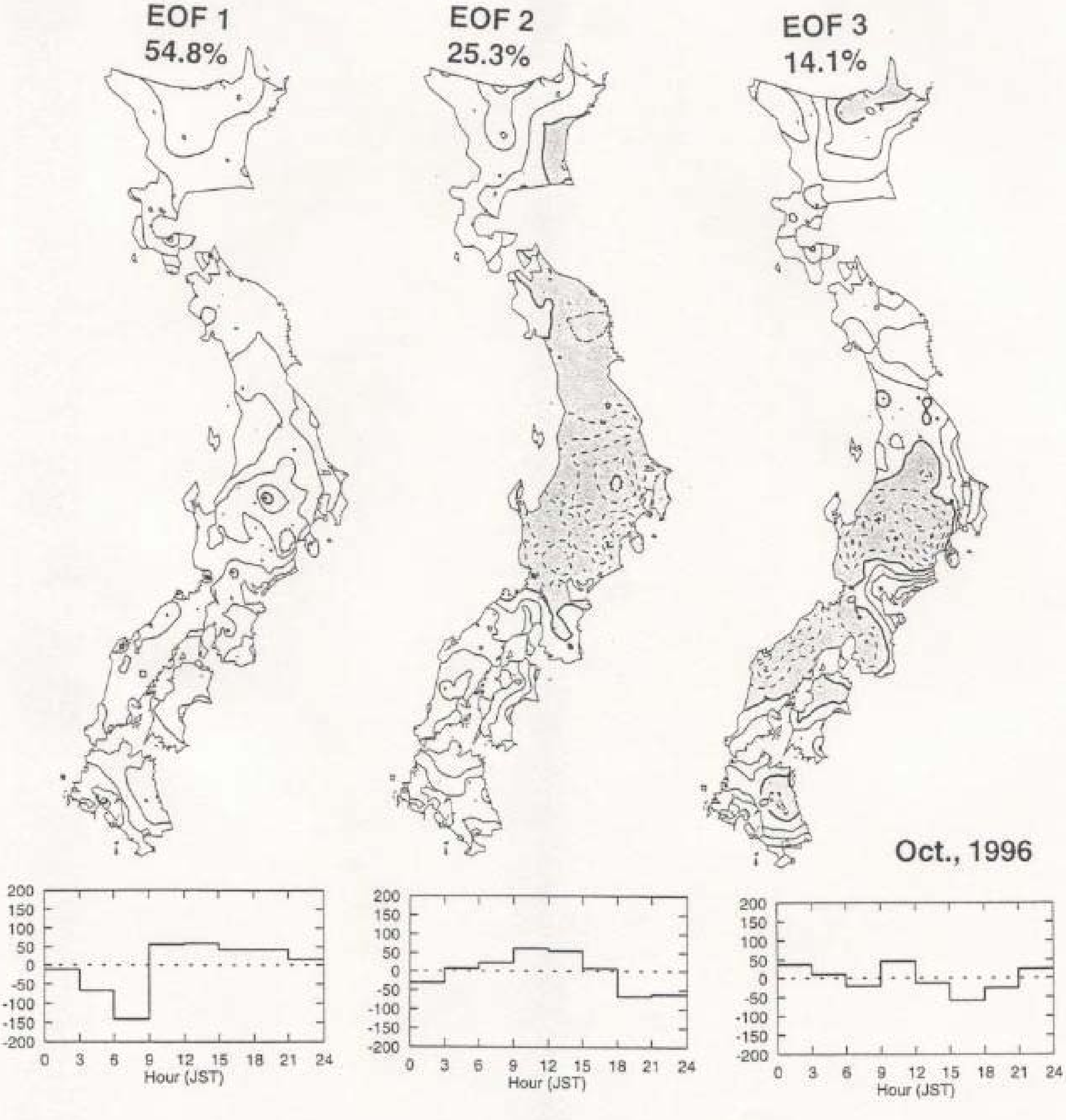

Figure 3.30: Same as Fig. 3.27, but in October, 1996

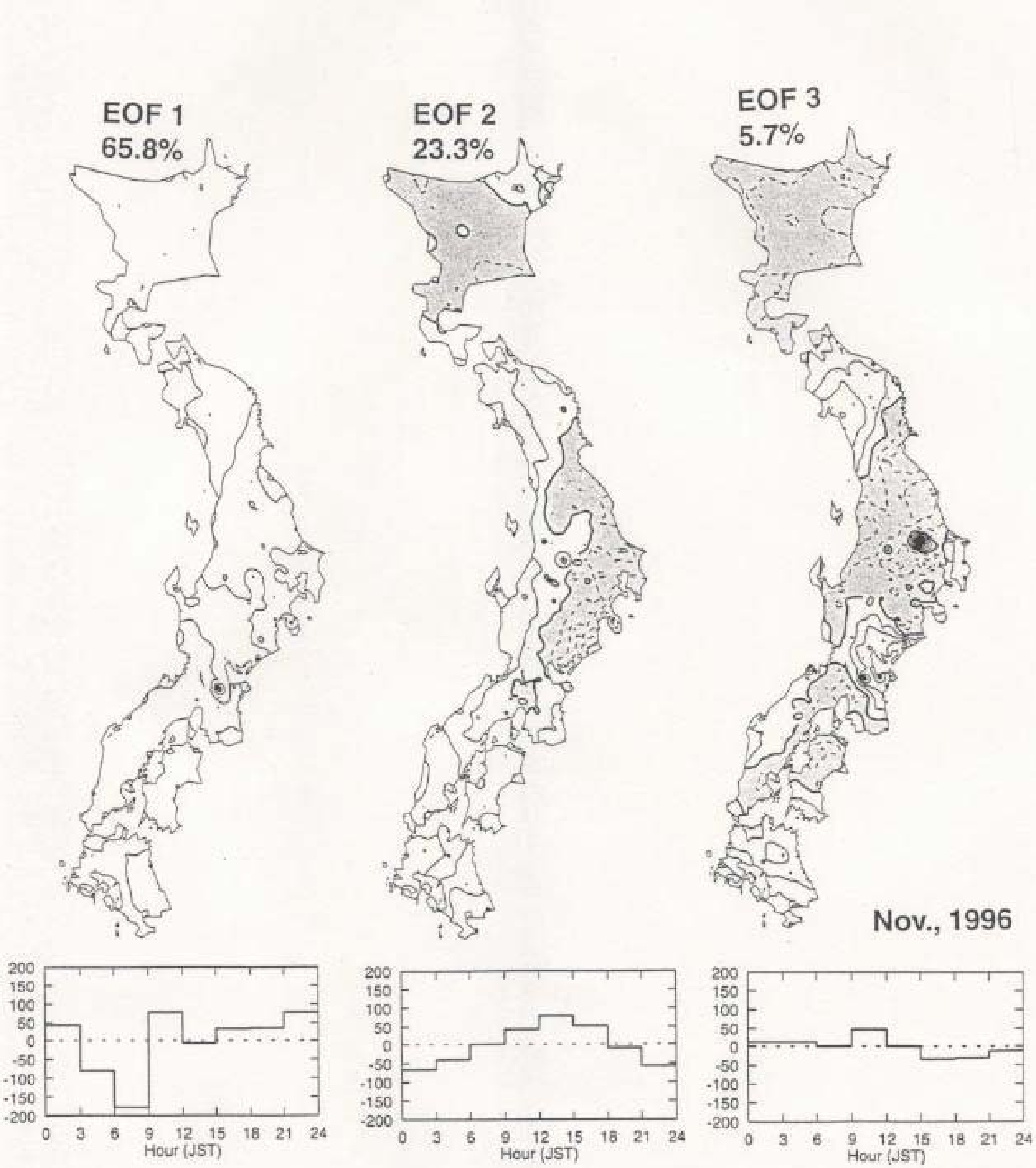

Figure 3.31: Same as Fig. 3.27, but of November, 1996

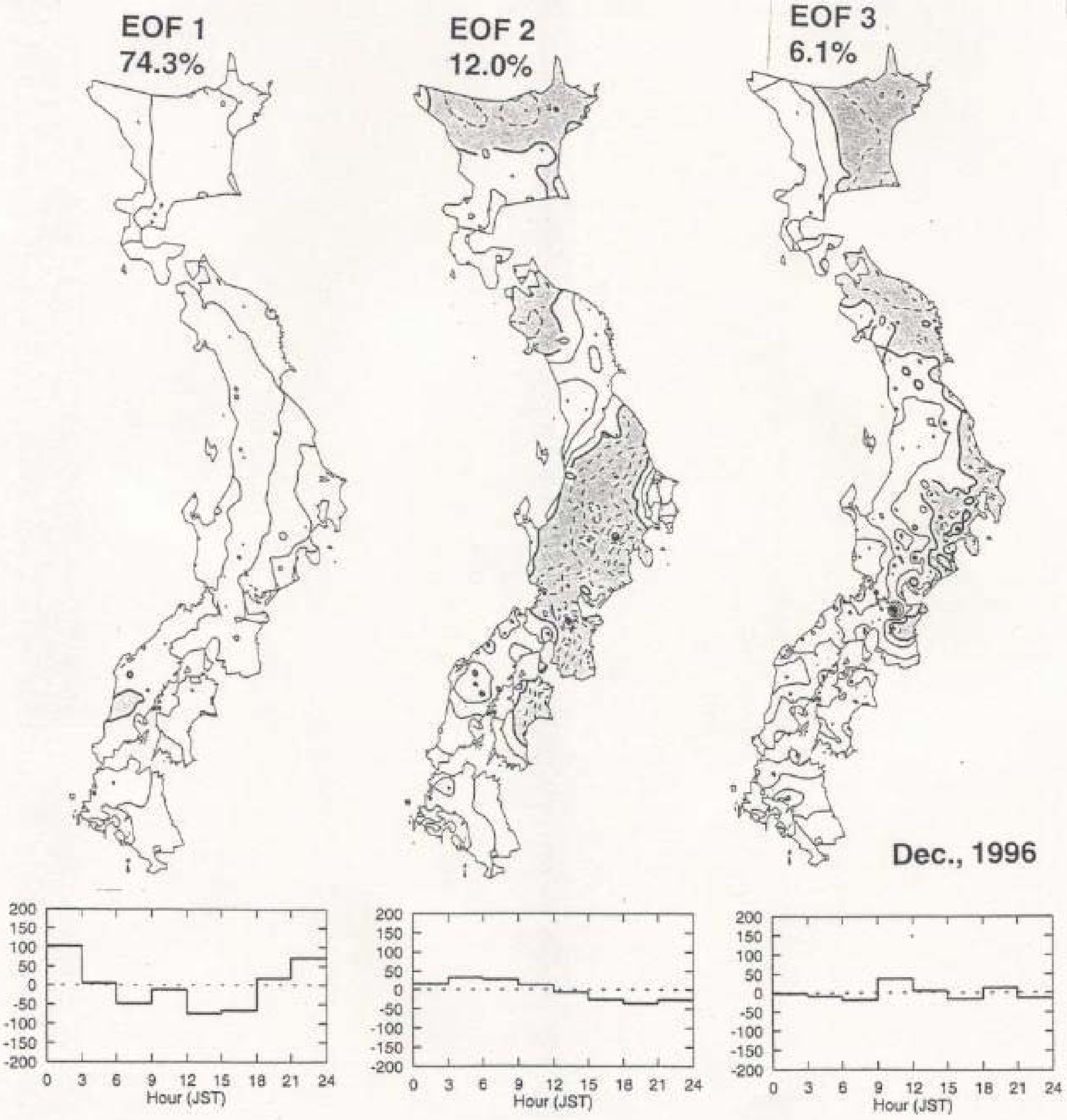

Figure 3.32: Same as Fig. 3.27, but in December, 1996

Bibliography

[*Bevis et al.*, 1992] Bevis, M., S. Businger, T. A. Herring, C. Rocken, R. A. Anthes, and R. H. Ware, GPS Meteorology: Remote Sensing of Atmospheric Water Vapor Using the Global Positioning System, *J. Geophys. Res.,* **97**, 15787-15801, 1992.

[*Businger et al.*, 1996] Businger, S., S. R. Chiswell, M. Bevis, J. Duan, R. A. Anthes, C. Rocken, R. H. Ware, M. Exner, T. VanHove, and F. S. Solheim, The Promise of GPS in Atmospheric Monitoring, *Bull. Am. Meteorol. Soc.,* **77**, 5-18, 1996.

[*Chida et al.*, 1999] Chida, K., I. Naito, T. Iwabuchi, in preparation, 1999.

[*Davis et al.*, 1985] Davis, J. L., T. A. Herring, I. I. Shapiro, A. E. E. Rogers, and G. Elgered, Geodesy by Radio Interferometry: Effects of Atmospheric Modeling Errors on Estimates of Baseline Length, *Radio Sci.,* **20**, 1593-1607, 1985.

[*Duan et al.*, 1996] Duan, J., M. Bevis, P. Fang, Y. Bock, S. Chiswell, S. Businger, C. Rocken, F. Solheim, T. Van Hove, R. Ware, S. McClusky, T. A. Herring, and R. W. King, GPS Meteorology: Direct Estimation of the Absolute Value of Precipitable Water, *J. Appl. Meteor.,* **35**, 830-838, 1996.

[*Elgered et al.*, 1997] Elgered, G., J. M. Johansson, B. O. Ronnang, and J. L. Davis, Measureing Regional Atmospheric Water Vapor Using the Swedish Permanent GPS Network, *Geophys. Res. Lett.,* **24**, 2663-2666, 1997.

[*Heki*, 1990] Three Approaches to Improve the Estimation Accuracies of the Vertical VLBI Station Positions, *Journal of the Geodetic Society of Japan,* **36**, 143-154, 1990.

[*Heki et al.*, 1997] Heki, K., S. Miyazaki, and H. Tsuji, Silent Fault Slip Following an Interplate Thrust Earthquake at the Japan Trench, *Nature,* **386,** 595-598, 1997.

[*Heki et al.*, 1998] Heki, K., in preparation, 1998.

[*Hogg et al.*, 1981] Hogg, D. C., F. O. Guiraud, and M. T. Decker, Measurement of Excess Transmission Length on Earth-Space Paths, *Astron. Astrophys.,* **95,** 304-307, 1981.

[*Iwabuchi et al.*, 1997] Iwabuchi, T., I. Naito, S. Miyazaki, and N. Mannoji, Behaviors of GPS Precipitable Water Vapor During A Front Passage, *Tenki,* **44,** 765-766, 1997, in Japanese.

[*Iwabuchi et al.*, 1998] Iwabuchi, T., I. Naito, N. Mannoji, and F. Kimura, Behaviors of Precipitable Water Vapor Retrieved by GPS array in Geographical Survey Institute of Japan, a special number issue on 'GPS Meterology Japan', Meteorological Research Note, Meteorological Society of Japan, Chapter 9,133-144, 1998, in Japanese.

[*Iwabuchi et al.*, 1998] Iwabuchi, T., I. Naito, and N. Mannoji, Behaviors of GPS Retrieved Precipitable Water Vapors over the Japanese Islands, to be submitted to *J. Geophys. Res.,* 1999.

[*Iwabuchi et al.*, 1998] Iwabuchi, T., I. Naito, and K. Chida, A Close Relationship between Temporal Anomalies in Site Coordinates and Zenith Tropospheric Delays in GPS Array over Japan, to be submitted to *Geophys. Res. Lett.,* 1999.

[*Iwabuchi and Naito*, 1998] Iwabuchi, T. and I. Naito, Diurnal Variation of GPS Retrieved Precipitable Water Vapors over the Japanese Islands in Summer, in preparation.

[*JMA*, 1997] Japan Meteorological Agency, Outline of the Operational Numerical Weather Prediction at the Japan Meteorological Agency, Appendix to Progress Report on Numerical Weather Prediction, Japan Meteorological Agency, pp126, 1997

[*Kimura and Kuwagata*, 1995] Kimura, F. and T. Kuwagata, Horizontal Heat Fluxes over Complex Terrain Computed Using a Simple Mixed Layer Model and a Numerical Model, *J. Appl. Meteor.,* **34**, 549-558.

[*Kuwagata*, 1997] An Analysis of Summer Rain Showers over Central Japan and its Relation with the Thermally Induced Circulation, *J. Meteor. Soc. Japan,* **75**, 513-527.

[*Leick*, 1990] Leick, A., GPS Satellite Surveying, John Wiley & Sons, 352 pp., 1990.

[*MacMillan*, 1995] MacMillan, D. S., Atmospheric Gradients from Very Long Baseline Interferometry Observations, *Geophys. Res. Let.,* **22**, 1041-1044., 1995.

[*Miyazaki et al.*, 1997] Miyazaki, S., T. Saito, M. Sasaki, Y. Hatanaka, and Y. Imura, Expansion of GSI's Nationeide GPS Array, Bulletin of the Geographical Survey Institute, 43, 23-34, 1997.

[*Ohtani and Naito*, 1998] Ohtani, R. and I. Naito, Evaluations of GPS retrieved Precipitable Water Vapors with Radiosonde Observations over Japan, submitted to *J. Meteor. Soc. Japan,* 1998.

[*Oki and Musiake*, 1994] Oki, T. and K. Musiake, Seasonal Change of the Diurnal Cycle of Precipitation over Japan and Malaysia, *J. Appl. Meteor.,* **33,** 1445-1463.

[*Preisendorfer*, 1988] Preisendorfer, R. W., Principal Component Analysis in Meteorology and Oceanography, 425pp, 1988.

[*Rocken et al.*, 1993] Rocken, C., R. Ware, T. Van Hove, F. Solheim, C. Alber, J. Johnson, M. Bevis, and S. Businger, Sensing Atmospheric Water Vapor with the Global Positioning System, *Geophys. Res. Lett.,* **20,** 2631-2634, 1993.

[*Rocken et al.*, 1995] Rocken, C., T. Van Hove, J. Johnson, F. Solheim, R. Ware, M. Bevis, S. Chiswell, and S. Businger, GPS/STORM - GPS Sensing of Atmospheric Water Vapor for Meteorology, *J. Atmos. Oceanic Technol.,* **12,** 468-478, 1995.

[*Rothacher and Mervart*, 1996] Rothacher, M. and L. Mervart (ed.), Documentation of the Bernese GPS Software Version 4.0, Astronomical Institute, University of Bern, 1996.

[*Thayer*, 1974] Thayer, G. D., An Improved Equation for the Radio Refractive Index of Air, Radio *Science,* **9,** 803-807, 1974.

[*Tobita*, 1994a] Tobita, M., Development of Coordinate Transformation Program TKY2WGS, Technical Memorandum of the Geographical Survey Institute, B1-No.23, 1994.

[*Tobita*, 1994b] Tobita, M., Applications of the Precise Geodetic Network and Integration of the Coordinate Systems, Technical Memorandum of the Geographical Survey Institute, B1-No.24, 1994.

[*Ware et al.*, 1996] Ware, R., M. Exner, D. Feng, M. Gorbunov, K. Hardy, B. Herman, Y. Kuo, T. Meehan, W. Melbourne, C. Rocken, W. Schreiner, S. Sokolovskiy, F. Solheim, X. Zou, R. Anthes, S. Businger, and K. Trenberth, GPS Sounding of the Atmosphere from Low Earth Orbit: Preliminary Results, *Bull. Am. Meteorol. Soc.,* **77,** 19-40, 1996.

[*Wessel and Smith*, 1991] Wessel, P. and W. H. F. Smith, Free Software Helps Map and Display Data, *EOS Trans. Amer. Geophys. U.,* **72,** 441, 445-446, 1991.

[*Yuan et al.*, 1993] Yuan, L., R. Anthes, R. Ware, C. Rocken, W. Bonner, M. Bevis, and S. Businger, Sensing Climate Change Using the Global Positioning System, *J. Geophys. Res.,* **98,** 14,925-14,937, 1993.

Epilogue

Summary and Further Research for Geodetic Monitoring of Effects of the Global Warming

We have done the basic discussions on phenomena caused by the global warming.

In chapter 2, we show that 37 % of the decadal polar motion can be explained by precipitation changes in North America and Eurasia with discussions based on the exponential decay model of the land water storage supplied by precipitation, and that more than 80% of the decadal polar motion can be explained by assuming decay time of 6 to 7 months. We advocate a new conceptual model on the decadal hydrologic cycle through the North Atlantic Ocean in atmosphere-hydrosphere system. Water and water vapor play an important role in thermal energy transport among atmosphere, hydrosphere, and lithosphere. In particular, water vapor is important for the global warming because of the most effective greenhouse effect gases in atmosphere, which accelerates the global warming by its positive feedback as mentioned in chapter 1. Thus, some new understandings of the decadal hydrologic cycle found in this study would be expected to contribute to the future prediction of the global warming.

In Chapter 3, the potential of the nationwide GPS array of GSI as an excellent all weather water vapor sensor has been clearly shown by visualizing ZTD and PWV retrieved by the GPS array during the front passages. In such severe weather conditions, a close relationship between horizontal coordinate variation and ZTD gradient has been found, suggesting that apparent horizontal coordinate variations can be diagnosed if they reflect the net crustal movement or not without meteorological data. Moreover, we have shown that the GPS array also detects the signal of diurnal variation of water vapor due to thermally induced local circulation over the Japanese Islands in summer, at the first time. All these facts indicate that GPS can detect basic information on water vapor if ground based GPS network distributed globally employs at a similar density of the GSI's GPS array. The increase of water vapor due to the global warming (see Section 1.2) will be also detected near future. In addition, a satellite-based GPS meteorology, a technique to retrieve temperature and water vapor with GPS receiver mounted on low Earth orbiting satellite based on the radio occultation technique, plays an important role in getting vertical information of the observable as a complementary observation for the ground-based method. An accumulation of those data is also expected to make it possible to clear transportation patterns of water vapor connected with the decadal hydrological cycle discussed in Chapter 2.

It will be possible to monitor both the minute crustal movement in connection with the occurrence of earthquakes and sea level rise due to the global warming by removing the effects of the crustal movement from tide gage data if precision of GPS coordinate estimation is improved by modeling behavior of water vapor. Of course, to understand behavior of water vapor lead not only to the improvement of GPS coordinate estimations but also to evaluations of role of water vapor in the global warming. Those are important subjects to be studied in the giant GPS array of Japan because of their complicated geographical conditions and ever changing wet climate condition there. Thus, the Japanese Islands are considered to be suitable for experimental field on GPS PWV.

Improvements of the quality of geodetic data due to employing space geodetic techniques make it possible to monitor and verify the effects of the global warming. Their rapid developments now in progress are remarkable. For example, Gravity Recovery and Climate Experiment (GRACE) mission now planned in USA is considered to be able to observe variations of land water storage of about 10mm in 100,000km^2 from the subtle orbital changes of the satellites caused by gravity anomalies near the Earth's surface. Geodetic data have peculiar property of being hard to be degraded in comparison with meteorological data because the former is based on the statistical processing of the artificial or natural periodic signal while the latter is based on the analog observation of intensity such as radiation or emission. In this thesis, we have tried to investigate effects connected with the global warming by using the space geodetic data. It is expected that the global warming and its effects will be well understood using the space geodetic techniques near future.

Appendix A

A.1 Physics of Polar Motion

The polar motion, changes in the orientation of the Earth's rotational axis relative to the Earth's figure axis, is caused by external torques and internal exchanges of angular momentum of the Earth, while variations in the Earth's axial angular velocity are expressed with length of day (LOD) changes.

We show physics of polar motion by referring to the descriptions of *Gross* [1992] and *Barnes et al.*, [1983]. Referred to set of Earth-fixed axes x_i ($i = 1, 2, 3$) aligned with the principal axes of the solid Earth and rotating with angular velocity $\boldsymbol{\omega}$ about its center of mass. Let $\boldsymbol{H}$ be the angular momentum vector of the Earth and $\boldsymbol{L}$ be the external torques acting upon the Earth. The conservation of angular momentum equation within the rotating reference frame (Euler's dynamical equations) is expressed by

$$\frac{d\boldsymbol{H}}{dt} + (\boldsymbol{\omega} \times \boldsymbol{H}) = \boldsymbol{L} \tag{A.1}$$

The angular momentum of the Earth $\boldsymbol{H}$ is given by

$$\begin{aligned} \boldsymbol{H} &= I_{ij} \cdot \boldsymbol{\omega} + \int (\boldsymbol{r} \times \boldsymbol{v}) dm \\ &= I_{ij} \cdot \boldsymbol{\omega} + \boldsymbol{h}, \end{aligned} \tag{A.2}$$

where I_{ij} is inertia tensor of the Earth, $\boldsymbol{v}$ is velocity of a particle which exists at radius vector $\boldsymbol{r}$ from Earth's center, and $\boldsymbol{h}$ is the angular momentum associated with relative motion.

Based on the conservation of the Earth's total angular momentum without external torque, the polar motion is described by perturbation equations for the equatorial angular velocities of the Earth. In initial condition, let the Earth model be in a state of uniform rotation at Ω about its figure axis and let no relative angular momentum be present. We consider a perturbation approach given by

$$I_{ij} = \begin{pmatrix} A & 0 & 0 \\ 0 & A & 0 \\ 0 & 0 & C \end{pmatrix} + \Delta I_{ij} \tag{A.3}$$

$$\omega = \Omega(m_1, m_2, 1 + m_3)^T \tag{A.4}$$

where C and A are the Earth's axial and equatorial principal moments of inertia, respectively, $\Omega = 0.7292115 \times 10^{-4} rad/s$ is Earth's mean angular velocity, and the dimensionless quantities m_i $(i = 1, 2, 3)$ are perturbations to the angular velocity. If we assume that all perturbations are small:

$$|\Delta I_{ij}| \ll C, |m_i| \ll 10^{-7}, \tag{A.5}$$

their products can be ignored, so that the linearized conservation of angular momentum equation becomes

$$\frac{i}{\sigma_r}\frac{d\tilde{m}}{dt} + \tilde{m} = \tilde{\chi}, \tag{A.6}$$

where $\tilde{m} = m_1 + im_2 = (\Delta\omega_1 + i\Delta\omega_2)/\Omega$ is written in complex form with m_1 (0^o E component) and m_2 (90^o E component), $\sigma_r = (C - A)\Omega/A$ is Eulerian frequency, and $\tilde{\chi} = \chi_1 + i\chi_2$ is dimensionless excitation function for the polar motion in complex form [*Gross*, 1992].

Eq. (A.6) was derived assuming the solid Earth to be perfectly rigid. However, in reality, variations in centrifugal forces of ω fluctuate and variations in surface loading due to changes of fluid mass distribution can deform the Earth, where the former is called rotational deformation and the latter is called surface loading deformation. To consider those effects, let introduce secular Love number $k_0 = [3(C - A)G]/\Omega^2 R^5$ by *Munk and MacDonald* [1975], second order rotational Love number k_2, and load Love number k_2'. With corrections to account for dissipation and for the lengthening of the free period due to non-rigid nature of the Earth, the conservation of angular momentum equation can be expressed as

$$\frac{i}{\tilde{\sigma_0}}\frac{d\tilde{m}}{dt} + \tilde{m} = \tilde{\chi} \tag{A.7}$$

$$\tilde{\sigma_0} = (k_0 - k_2)\sigma_r/k_0 + i\alpha \tag{A.8}$$

[for details see *Eubanks*, 1993]. In Eq. (A.7), $\tilde{\sigma_0} = 2\pi\{F_c(1 + 1/2Q_c)\}$ is complex-valued frequency of Chandler wobble, that is one of the Earth's free oscillation, F_c is frequency (0.843cpy) of Chandler wobble, and $1/Q_c$ is the factor which indicates the dissipation of energy near F_c [*e.g.*, *Munk and MacDonald*, 1960; *Wilson*, 1985].

The excitation function in Eq. (A.7) is expressed by

$$\tilde{\chi} = \frac{1 + k_2'}{1 - (k_2/k_0)} \widetilde{\Delta I}/(C - A) + \frac{1}{1 - (k_2/k_0)} \widetilde{\Delta h}/[\Omega(C - A)], \tag{A.9}$$

where the first and second term on the right-hand side are generally called 'matter term' due to mass redistribution effect and 'motion term' due to relative angular momentum effect, respectively [*Barnes et al.*, 1983]. $\widetilde{\Delta I}$ and $\widetilde{\Delta h}$ are inertia products and equatorial component of relative angular momentum of atmosphere and hydrosphere written as

$$\widetilde{\Delta I} = -\int (r^2 \cos\phi \sin\phi) \exp(i\lambda) \rho dV \tag{A.10}$$

$$\widetilde{\Delta h} = -\int (ur \sin\phi + irv) \exp(i\lambda) \rho dV, \tag{A.11}$$

where $\int \rho dV$ shows mass integration of the whole volume of fluids with the density ρ, r is the Earth's mean radius, ϕ and λ are latitude and longitude, and u and v are eastward and northward velocities, respectively. When traditional coefficients; $k_0 = 0.942, k_2 = -0.285, k_2' = -0.30$ [*Barnes et al.*, 1983], are substituted in Eq. (A.9), the excitation function is written as

$$\tilde{\chi} = 1.00 \widetilde{\Delta I}/(C - A) + 1.43 \widetilde{\Delta h}/[\Omega(C - A)] \tag{A.12}$$

where the coefficients 1.00 and 1.43 on the right-hand side are called the transfer functions caused by Love number corrections for elastically deformable Earth with respect to rigid Earth.

Eq. (A.7) can be simplified at frequencies much lower than the Chandler wobble frequency F_c yielding as

$$\tilde{m} \cong \tilde{\chi}. \tag{A.13}$$

[*Eubanks*, 1993]. Thus for physical discussion, we can apply Eq. (A.13) to variations on decadal time-scale.

Appendix B

B.1 Outline of GPS Measurement

Global Positioning System (GPS), satellite-based navigation system with on board atomic clock developed in the USA, provides precise three-dimensional position, navigation, and time better than μs [*Leick*, 1990; *Günter*, 1993; *Gilbert and Kai*, 1997]. The system consists of three segments; (1) Space segment composed of 24 satellites in almost circular orbits in six orbital planes at the height of 20000 km and the orbital period of 12 hours of sidereal time, where GPS satellites transmit two carrier frequency (L1: 1575.42 MHz and L2: 1227.60 MHz) based on the fundamental frequency 10.23 MHz of the atomic clock, (2) Control segment to monitor and control GPS satellites such as uploading broadcast ephemerides to the satellites for providing satellite orbit information to users, and (3) User segment composed of GPS receiver, GPS analysis software, and observers. The receiver measures its distance to each satellite with an accuracy of several ten meters, which is enough for instantaneous positioning for mobile vehicle or vessel navigation with broadcast ephemerides. For geodetic purpose, the accuracy can be improved to several mm to cm in post-processing by using offset value from a fixed receiver (relative positioning) or by using accurate clock information of satellites (precise point positioning). Both also need precise satellite orbit information (precise ephemerides) generally provided after several days of the observation.

We show outline of GPS measurement by referring to the descriptions of *Günter* [1993]. We define that the carrier phase $\Phi_c(t_s)$ leaves the satellite at epoch t_s in satellite time frame and reaches the GPS antenna at epoch t_r in receiver time frame. Since the carrier phase observation does not provide us its initial wave number between t_s and t_r in the start of the observation, $\Phi_c(t_s)$ is written as

$$\Phi_c(t_s) = 2\pi \cdot N + \phi_c(t_s), \tag{B.1}$$

where the first term of the right-hand side is the integer part with integer ambiguity N, the second term is the real part. The observable in carrier phase observation is the difference between the Doppler shifted carrier phase transmitted from satellite $\phi_c(t_s)$ and the phase of the reference signal produced by receiver $\Phi_r(t_r)$. The observed phase $\phi_{obs}(t_r)$ is

$$\phi_{obs}(t_r) = \phi_s(t_s) - \Phi_r(t_r), \tag{B.2}$$

where t_s is expressed as

$$t_s = \frac{\Phi_c(t_s)}{2\pi f_c} = \frac{\phi_c(t_s)}{2\pi f_c} + \frac{N}{f_c}, \tag{B.3}$$

where f_c is carrier frequency. The second term on the right-hand side multiplied signal propagation velocity c is called ambiguity term. The measured distance between receiver and satellite is called pseudorange PR because it is true range R plus some biases and errors of satellite clock error dt_s, clock synchronization error in receiver dt_u, atmospheric propagation delay dt_a, and observation noise ϵ. Thus, observation equation for phase measurement is

$$PR = R + cdt_u + cdt_a + cdt_s + c\frac{N}{f_c} + \epsilon. \tag{B.4}$$

In relative positioning, precise estimation of site coordinates is made possible by method to calculate phase difference of several carrier phase observations to remove satellite- and receiver- clock errors. Here, we define two receivers i, j and two satellites p, q and introduce operators for difference of the two receivers Δ and for difference of the two satellites ∇ by following the notation of *Wells et al.* [1986] and *Günter* [1993]. When the carrier phase difference between the two receivers (single difference) with Eq. (B.4) is formed as

$$\begin{aligned}\Delta PR_{ij} &= \Delta R_{ij} + c(dt_{u_j} - dt_{u_i}) + c(dt_{a_j} - dt_{a_i}) + c(dt_s - dt_s) + \frac{c}{f_c}(N_j - N_i) + \epsilon_\Delta \\ &= \Delta R_{ij} + c\Delta dt_{u_{ij}} + c\Delta t_{a_{ij}} + \frac{c}{f_c}\Delta N_{ij} + \epsilon_\Delta, \end{aligned} \tag{B.5}$$

satellite clock error dt_s is removed. Similarly, when difference of the two single differences between the two satellites (double difference) with Eq. (B.5) is formed as

$$\begin{aligned}\nabla\Delta PR_{ij}^{pq} &= (\Delta R_{ij}^p - \Delta R_{ij}^q) + c(\Delta t_{u_{ij}} - \Delta t_{u_{ij}}) + c(\Delta t_{a_{ij}}^p - \Delta t_{a_{ij}}^q) + \frac{c}{f_c}(\Delta N_{ij}^p - \Delta N_{ij}^q) + \epsilon_{\nabla\Delta} \\ &= \nabla\Delta R_{ij}^{pq} + c\nabla\Delta t_{a_{ij}}^{pq} + \frac{c}{f_c}\nabla\Delta N_{ij}^{pq} + \epsilon_{\nabla\Delta}, \end{aligned} \tag{B.6}$$

receiver clock synchronization error $\Delta t_{u_{ij}}$ is removed. Consequently, both satellite and receiver clock errors are removed skillfully, and other common errors in the both sites also can be partly canceled in double difference. In addition, improvements of precision in satellite orbit estimation of about 10 cm and progress of the analysis technique in GPS software have contributed to precise coordinate estimation in the relative positioning.

The atmospheric propagation delay error dt_a consists of ionospheric delay which depends on electron content along the signal path and tropospheric delay due to neutral air in atmosphere. The former can be removed by using the two-carrier frequency due to the dispersion relationship, that is, it is known to be proportional to frequency to the power minus two. However, tropospheric delay can not be removed easily due to that non-dispersion relationship.

Unknown parameters estimated simultaneously by least square method in the relative positioning analysis applied in GSI(Geographical Survey Institute)'s routine analyses, for example, are (1) initial- and accidental- integer ambiguities in double differences (Eq. B.6), (2) daily three dimensional positions of phase center of GPS antennas, and (3) three-hourly zenith tropospheric delay (ZTD), where tropospheric delays in each elevation angle of satellites are mapped into zenith direction due to shortage of observation to unknown parameters (see Appendix B.2). The daily resolution for coordinate estimations is applied to average errors caused by different satellite configurations, heat expansion of GPS monuments by solar radiation, crustal deformation by tidal loading effects of the ocean, thermally induced local circulation such as land- and sea- breeze and valley wind etc., and three-hourly estimation of ZTD is empirically applied since variations of atmosphere can not be followed in daily resolution, while higher temporal resolution, which corresponds to increase of unknown parameters, also degrade precision of coordinate estimation.

In general, no correlation between coordinate solution and ZTD is statically assumed in GPS analysis. However, it is difficult to separate both parameters perfectly due to agreement of the both directions, especially vertical component.

B.2 Physics of GPS Tropospheric Delay

We show physics of GPS toropospheric delay by referring to the descriptions of *Ohtani and Naito* [1999]. In general, tropospheric delay ΔL can be written as

$$\begin{aligned} \Delta L &= \int_L n ds - G \\ &= \int_L (n-1) ds + (S-G) \end{aligned} \tag{B.7}$$

where $n(s)$ is atmospheric refractive index as a function of positions along the curved path L, $S(= \int_L ds)$ is path length along L, and G is the geometrical straight-line path length between the satellite and the GPS site at the ground [*e.g.*, *Bevis et al.*, 1992]. The first term on the right-hand side of Eq. (B.7) is called the speed term due to slowing effect of the ray, and the second term is called the curvature term due to bending of the ray. Only the speed term has often been considered in usual GPS observations because the curvature term is negligible for paths with elevation angles greater than about 15 degrees applied in general GPS observations [*e.g.*, *Bevis et al.*, 1992; *Ichikawa et al.*, 1995].

Since $(S-G)$ in Eq. (B.7) becomes zero in zenith direction, ZTD is expressed as

$$ZTD = \int (n-1) dz. \tag{B.8}$$

In GPS analysis, tropospheric delay at arbitrary elevation angle is, in general, expressed as a product of zenith tropospheric delay (ZTD) and mapping function $m(\theta)$ where θ is elevation angle [see *Leick*, 1990 for details, for example]. The mapping function is used to obtain only one ZTD from various tropospheric delays observed at various elevation angles during an observational session. A basic mapping function $m(\theta)$ at arbitrary elevation angle θ is described as

$$m(\theta) = 1/sin(\theta), \tag{B.9}$$

with assuming azimuthally homogeneous distributions of atmospheric air density. Thus, if a typical scale height of water vapor, for example, is assumed to be about 3 km, GPS observations using all GPS satellites with elevation angles above 15 degrees can acquire the information of averaged water vapor inside an inverse cone with diameter of about 24 km at height of 3 km. Although Eq. (B.9) does not consider inhomogeneous distribution of water vapor for horizontal direction, the mapping function is advantageous to restrict the number of estimated parameters by least square method.

The atmospheric refractive index in zenith direction can be expressed as

$$10^6(n-1) = k_1 \frac{P_d}{T} Z_d^{-1} + k_2 \frac{P_v}{T} Z_v^{-1} + k_3 \frac{P_v}{T^2} Z_v^{-1}, \tag{B.10}$$

where T (K) is temperature, P_d (hPa) is the partial pressure of dry air, P_v (hPa) is partial pressures of water vapor, $k_i (i = 1,2,3)$ are experimental constants; $k_1 = 77.64 \pm 0.05 K/hPa$, $k_2 = 70.4 \pm 2.2 K/hPa$, and $k_3 = (3.739 \pm 0.012) \times 10^5 K^2/hPa$, for example [*Bevis et al.*, 1994], Z_d and Z_v are compressibility of dry air and wet air, respectively, where the compressibility which is nearly equal to 1 account for corrections for departure of air from an ideal gas.

When Eq. (B.10) is substituted into Eq. (B.8) and then Eq. (B.10) is integrated by using equation of state of atmosphere, ZTD is rewritten as

$$ZTD = 10^{-6}\left(\int k_1 \frac{R}{m_d} \rho dz + \int k_2' \frac{P_v}{T} Z_v^{-1} dz + \int k_3 \frac{P_v}{T^2} Z_v^{-1} dz\right) \tag{B.11}$$

where

$$k_2' \equiv k_2 - k_1 \frac{m_v}{m_d}, \tag{B.12}$$

ρ is density of mixed atmosphere of dry air and water vapor, m_d and m_v are molar masses of dry air ($28.9644 kg/kmol$) and water vapor ($18.0152\ kg/kmol$), respectively, and R is universal gas constant ($8314.34\ J/kmolK$). Since the first term on the right-hand side of Eq. (B.11) only depends on the total density of atmosphere, its vertical integration assuming hydrostatic equilibrium gives zenith hydrostatic delay (ZHD) given as

$$ZHD = 10^{-6} k_1 \frac{R}{m_d g_m} P_s, \tag{B.13}$$

where P_s is total pressure in hPa, and g_m can be approximated to

$$\begin{aligned} g_m &= 9.784(1 - 0.00266 \cos 2\phi - 0.00028H) \\ &= 9.784 f(\phi, H). \end{aligned} \tag{B.14}$$

In Eq. (B.14), $f(\phi, H)$ is factor accounting for gravity dependency on latitude ϕ and height H of GPS site in km [*Davis et al.*, 1985]. Hence, ZHD is rewritten as

$$ZHD = (2.2779 \pm 0.0024) \frac{P_s}{f(\phi, H)}. \tag{B.15}$$

Eq. (B.15) indicates that ZHD can be calculated by atmospheric pressure and height of site. If the atmospheric pressure can be given with accuracy of better than 0.4 hPa, ZHD can be determined with accuracy better than 1 mm.

By using thus obtained ZHD, the wet delay in zenith direction (*i.e.*, Zenith Wet Delay (ZWD)) is calculated as

$$ZWD = ZTD - ZHD, \tag{B.16}$$

where ZTD is estimated from GPS data. Since the second and third terms on the right-hand side of Eq. (B.11) contribute to ZWD, ZWD depends only on temperature and water vapor pressure.

ZWD has been known to be nearly proportional to PWV [*Hogg et al.*, 1981; *Davis et al.*, 1985] as below [*Askne and Nordius*, 1987],

$$\begin{aligned} ZWD &= 10^{-6}(\int k_2{}' \frac{P_v}{T} Z_v^{-1} dz + \int k_3 \frac{P_v}{T^2} Z_v^{-1} dz) \\ &= 10^{-6} R_v (k_2{}' + k_3 \frac{\int \frac{P_v}{T^2} dz}{\int \frac{P_v}{T} dz}) \int \frac{P_v}{R_v T} Z_v^{-1} dz \\ &= 10^{-6} R_v (k_2' + k_3 \frac{\int \frac{P_v}{T^2} dz}{\int \frac{P_v}{T} dz}) \int \rho_v dz \\ &= \Pi^{-1} PWV, \end{aligned} \tag{B.17}$$

where

$$\Pi^{-1} = 10^{-5}(\frac{k_3}{T_m} + k_2')R_v, \tag{B.18}$$

$$T_m = \frac{\int \frac{P_v}{T} dz}{\int \frac{P_v}{T^2} dz}, \tag{B.19}$$

where R_v and ρ_v are specific gas constant and density for water vapor, and T_m is mean temperature calculated by weighted integration with partial pressure of water vapor P_v, and Π is constant of proportionality [*Davis et al.*, 1985; *Askne and Nordius*, 1987].

Bevis et al. [1992] showed GPS retrieved PWV to be formulated with a constant of proportionality Π as

$$PWV = \Pi \cdot ZWD. \tag{B.20}$$

Here, Π can be determined with accuracy to about 2% based on atmospheric surface temperature [*Bevis et al.*, 1992] or to about 1% based on Numerical Weather Prediction (NWP) data [*Bevis et al.*, 1994].

In consequence, retrieval of PWV from GPS data need first to estimate ZTD from GPS data, second to calculate ZHD from atmospheric surface pressure and height at GPS site, third to subtract ZHD from ZTD to obtain ZWD, and last to obtain PWV by multiplying ZWD with Π calculated from radiosonde data or NWP data.

Appendix C

C.1 Principal Component Analysis

Principal component analysis is one of statistical method to find smaller number of linear combination of original variables maximizing the variance accounted for in the original data. This is equal to an eigenvalue analysis of the covariance or correlation matrix. Principal component analysis is also called empirical orthogonal function (EOF) analysis and eigen-analysis.

We state the algebraic essentials of principal component analysis simply by referring to the descriptions of *Preisendorfer, R. W.* [1988]

Let $z(t,x)$ be data at point x and time t, where time average at each x should be subtracted from raw data. Let the observation of z be taken over the set of location $x = 1, ..., p$ at times $t = 1, ..., n$. We then have the $n \times p$ data matrix Z in $z(t,x)$ as

$$Z = \begin{pmatrix} z(1,1) & \dots & z(1,p) \\ \vdots & \ddots & \vdots \\ z(n,1) & \dots & z(n,p) \end{pmatrix}. \tag{C.1}$$

The elements of data matrix form a swarm of points about the origin of p-dimensional euclidian space E_p.

From points in E_p, the $p \times p$ symmetric scatter matrix $\boldsymbol{S}$ is formed as

$$\boldsymbol{S} = \boldsymbol{z}\boldsymbol{z}^T. \tag{C.2}$$

This matrix has a set of p orthogonal eigenvectors $\boldsymbol{e} = [e_j(1), ..., e_j(p)]^T, j = 1, ..., p$. These called EOF (empirical orthogonal function), where 'empirical' derived from data, 'orthogonal' derived from no correlation over space formulated by

$$\sum_{x=1}^{p} e_j(x)e_k(x) = \begin{cases} 0 & (j \neq k) \\ 1 & (j = k) \quad (j,k = 1,...,p). \end{cases} \tag{C.3}$$

We can construct the principal components (or amplitudes) a_j of the data set from $\boldsymbol{e}_j$ as

$$a_j(t) = \sum_{x=1}^{p} z(t,x)e_j(x) = \boldsymbol{z}^T(t)\boldsymbol{e}_j \tag{C.4}$$
$$(t = 1,...,n; j = 1,...,p).$$

These $a_j(t)$ $(t = 1,...,n)$ have no temporal correlation. They carry information about the variance of the data set along the direction $\boldsymbol{e}_j$ as

$$\sum_{t=1}^{n} a_j(t)a_k(t) = \begin{cases} 0 & (j \neq k) \\ l_j & (j = k) \quad (j,k = 1,...,p). \end{cases} \tag{C.5}$$

where l_j is the j^{th} eigenvalue of $\boldsymbol{S}$. The original centered data set $z(t,x)$ can be represented in the form

$$z(t,x) = \sum_{j=1}^{p} a_j(t)e_j(x) \tag{C.6}$$
$$(t = 1,...,n; x = 1,...,p).$$

The percentage (or proportion) P of the total variance in the data matrix Z explained by j^{th} eigen vector is expressed by

$$P_j = \frac{l_j}{\sum_{x=1}^{p} l_x}. \tag{C.7}$$

The accumulated proportion AP of the total variance of j principal components is thus given by

$$AP_j = \frac{\sum_{x=1}^{j} l_x}{\sum_{x=1}^{p} l_x}. \tag{C.8}$$

The individual principal modes approximate the dominant features of the observed variation because principal modes are empirically designed to fit the particular data set. Thus, in general, only a few modes are required for adequate approximation to that variation.

Bibliography

[*Askne and Nordius*, 1987] Askne, J. and H. Nordius, Estimation of Tropospheric Delay for Microwave from Surface Weather Data, *Radio Sci.,* **22,** 379-386, 1987.

[*Barnes et al.*, 1983] Barnes, R. T. H., R. Hide, A. A. White, and C. A. Wilson, Atmospheric Angular Momentum Function, Length-of-Day Changes and Polar Motion, *Proc. E. Soc. Lond.,* **A387,** 31-73, 1983.

[*Bevis et al.*, 1992] Bevis, M., S. Businger, T. A. Herring, C. Rocken, R. A. Anthes, and R. H. Ware, GPS Meteorology: Remote Sensing of Atmospheric Water Vapor Using the Global Positioning System, *J. Geophys. Res.,* **97,** 15787-15801, 1992.

[*Bevis et al.*, 1994] Bevis, M., S. Businger, S. Chiswell, T. A. Herring, R. A. Anthes, C. Rocken, and R. H. Ware, GPS Meteorology: Mapping Zenith Wet Delay onto Precipitable Water, *J. Appl. Meteor.,* **33,** 379-386, 1994.

[*Davis et al.*, 1985] Davis, J. L., T. A. Herring, I. I. Shapiro, A. E. E. Rogers, and G. Elgered, Geodesy by Radio Interferometry: Effects of Atmospheric Modeling Errors on Estimates of Baseline Length, *Radio Sci.,* **20,** 1593-1607, 1985.

[*Eubanks*, 1993] Eubanks, T. M., Variations in the Orientation of the Earth, in Contributions of Space Geodesy to Geodynamics: Earth Dynamics, 24, pp. 1-54, eds. Smith, D. E. and Turcotte, D. L., American Geophysical Union, Washington, DC., 1993.

[*Gilbert and Kai*, 1997] Gilbert, S. and Kai, B., Linear Algebra, Geodesy, and GPS, Wellesley-Cambridge Press, 624pp., 1997.

[*Gross*, 1992] Gross, R. S., Correspondence between Theory and Observations of Polar Motion, *Geophys. J. Int.,* **109**, 162-170, 1992.

[*Günter*, 1993] Günter, S., Satellite Geodesy: Foundations, Methods, and Applications, Walter de Gruyter, 209-355, 531pp., 1993.

[*Hogg et al.*, 1981] Hogg, D. C., F. O. Guiraud, and M. T. Decker, Measurement of Excess Transmission Length on Earth-Space Paths, *Astron. Astrophys.,* **95**, 304-307, 1981.

[*Ichikawa et al.*, 1995] Ichikawa, R, M. Kasahara, N. Mannoji, and I. Naito, Estimations of Atmospheric Excess Path Delay Based on Three-dimensional Numerical Prediction Model Data, *J. Geod. Soc. Japan,* **31**, 379-408, 1995.

[*Lambeck*, 1980] Lambeck, K., The Earth's Variable Rotation, Cambridge University Press, Cambridge, 1980.

[*Leick*, 1990] Leick, A., GPS Satellite Surveying, John Wiley & Sons, 352 pp., 1990.

[*Munk and MacDonald*, 1960] Munk, W. H., and G. J. F. MacDonald, The Rotation of the Earth. Cambridge University Press, Cambridge, 323pp, 1960.

[*Ohtani and Naito*, 1998] Ohtani, R. and I. Naito, Evaluations of GPS retrieved Precipitable Water Vapors with Radiosonde Observations over Japan, submitted to *J. Meteor. Soc. Japan, 1998.*

[*Preisendorfer*, 1988] Preisendorfer, R. W., Principal Component Analysis in Meteorology and Oceanography, 425pp, 1988.

[*Wilson*, 1985] Wilson, C. R., Discrete Polar Motion Equations, *Geophys. J. R. astr. Soc.,* **80**, 551-554, 1985.